Investigations on Li$M_{0.5}$Mn$_{1.5}$O$_4$ (M = Fe, Co, Ni) Spinels as High-Volt Cathode Materials for Rechargeable Lithium-Ion Batteries

PhD Dissertation

Aiswarya Bhaskar
Institute for Materials Science

TECHNISCHE UNIVERSITÄT DARMSTADT

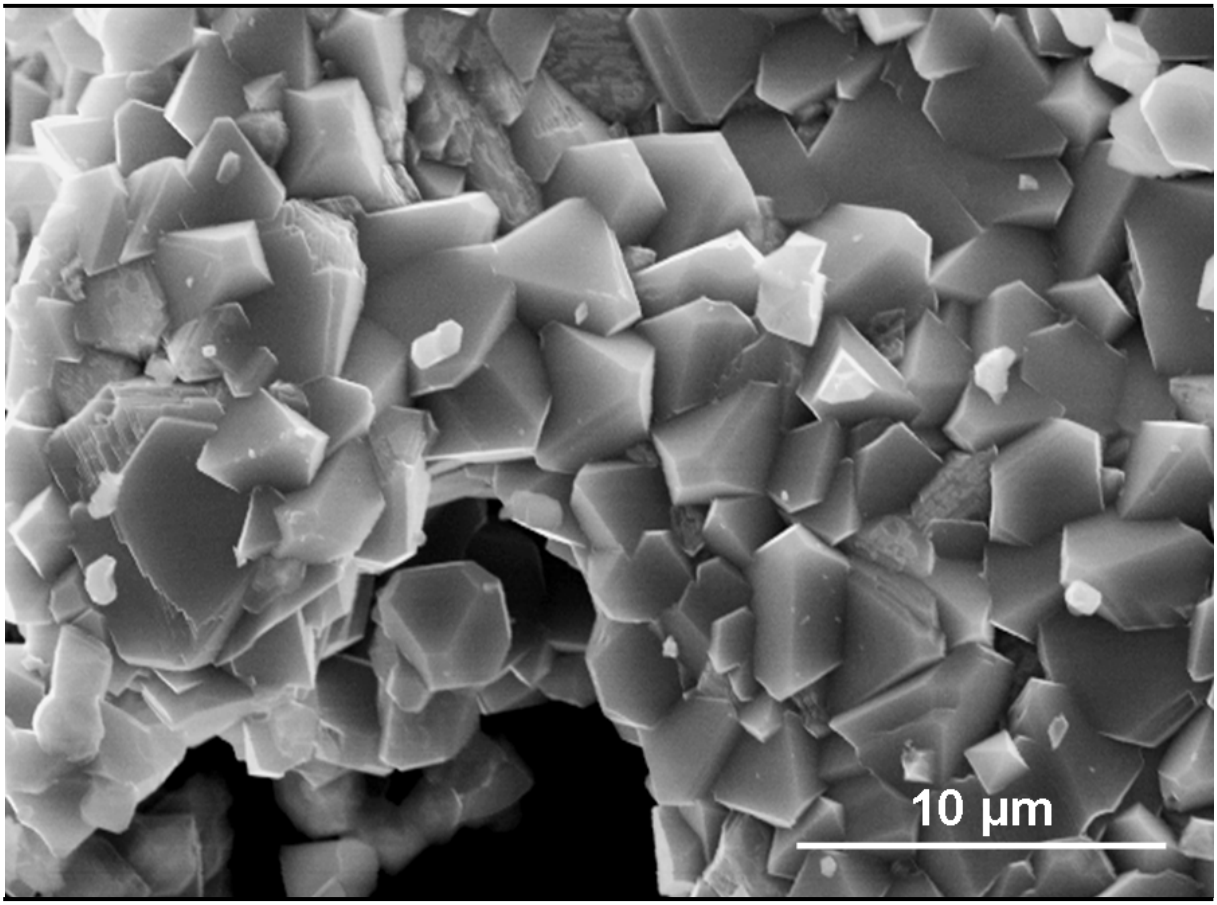

Investigations on $LiM_{0.5}Mn_{1.5}O_4$ (*M* = Fe, Co, Ni) Spinels as High-Volt Cathode Materials for Rechargeable Lithium-Ion Batteries

A dissertation submitted to the
Institute for Materials Science, Technische Universität Darmstadt

For the degree of
Doctor of Sciences
(Dr. rer. nat.)

Presented by

Aiswarya Bhaskar

MSc. Chemistry, Mahatma Gandhi University, India
Born on May 23, 1984 at Cherthala, India
Citizen of India

Referee:	Prof. Dr. rer. nat. W. Jaegermann
Co-referee:	Prof. Dr. rer. nat. H. Ehrenberg
Date of submission:	01/19/2011
Date of oral exam:	04/06/2011

Darmstadt 2011

D 17

Table of contents

List of symbols, fundamental constants and abbreviations

a	Chemical activity for relevant species
A	Surface area
CE	Counter electrode
C-rate	Charge-discharge rate
dE	First derivative of voltage of working electrode (vs. Li/Li^+)
DEC	Diethyl carbonate
DMC	Dimethyl carbonate
DMF	Dimethyl formamide
dQ	First derivative of specific capacity
DTA	Differential thermal analysis
E^0	Standard electrode potential
$E^{0,(-)}$	Negative electrode potential
$E^{0,(+)}$	Positive electrode potential
E^0_{cell}	Standard cell potential (the equilibrium cell potential when all reactants and products are in their standard states)
E^0_{red}	Standard half-cell reduction potential
E	Voltage of working electrode vs. Li/Li^+
EC	Ethylene carbonate
E_{cell}	Cell potential at temperature of interest
EMC	Ethyl methyl carbonate
EMI TFSI	1-ethyl-3-methylimidazonium-bis(trifluoromethylsulfonyl) imide
E_{red}	Half-cell reduction potential at temperature of interest
EV	Electric vehicles
Ewe	Voltage of working electrode vs. Li/Li^+
F	Faraday constant
GBL	γ-Butyrolactone
GCPL	Galvanostatic cycling
h	Hours

HEV	Hybrid electric vehicles
I	Current
ICP-OES	Inductively coupled plasma-optical emission spectroscopy
j	Current density
LiBOB	Lithium bis-(oxalato)borate
$LiPF_6$	Lithium hexafluorophosphate
LiTFSI	Lithium 1-ethyl-3-methylimidazonium-bis(trifluoromethylsulfonyl) imide
LIPON	Lithium phosphorus oxynitride
M	Mass of the active compound
m_i	Mass of reactants
mm	millimeter
M_r	Host molecular weight
n	Number of electrons
NEC	Nippon electric company
NMP	N-Methylpyrrolidone
OBI	On-site readable image-plate detector
OCV	Open circuit voltage
p	Specific power
PC	Propylene carbonate
PCGA	Potentiodynamic cycling with galvanostatic acceleration
PEO	Polyethylene oxide
PITT	Potentiostatic intermittent titration technique
ppm	Parts per million
PSD	Position sensitive detector
P_V	Power density
PVDF	Poly(vinylidene fluoride)
Q	Charge capacity
q_{th}	Theoretical specific charge
$Q_{V,\,th}$	Theoretical charge density
R	Universal gas constant
RE	Reference electrode
RT	Room temperature
SEI	Solid electrolyte interface
SEM	Scanning electron microscopy
SHE	Standard hydrogen electrode

T	Absolute temperature
TG	Thermogravimetry
V_i	Volume of the reactants
WE	Working electrode
w_{th}	Theoretical specific energy
$W_{V,\,th}$	Theoretical energy density
w/w	Weight/weight
XPS	X-ray photoelectron spectroscopy
XRD	X-ray diffraction
$-\Delta G^0$	Standard Gibbs free energy
Δt	Time interval

Chapter 1
Introduction

Lithium ion batteries are known of their high operation voltage. The most of commercial lithium-ion cells today use the chemistry combining so called "4 V cathode materials" (layered $Li(Ni/Co/Mn)O_2$, spinel $LiMn_2O_4$ as well as their doped derivatives) and graphite anode. The development of new cathodes operating at higher voltages can significantly increase the energy density of electrochemical cell. Moreover, high-voltage cathodes would allow the adoption of the anode materials other than graphite without a penalty in energy density.

The cathode materials operating at the voltages close to 5 V vs. metallic lithium, "5 V cathode materials", are known since 1990 [**Tarascon 1993]**. Though they have been remaining in the focus of research interest since many years, the lithium-ion technology is not yet ready to adopt their use in commercial cells. The principal obstacle here is the high likelyhood of side reactions in the electrochemical cell at such as high voltages (liquid-electrolyte oxidation, cell-components' corrosion, etc), which would strongly impinge on cycle life and safety of the battery. The development of stable electrolyte system enabling the application of 5 V cathodes is one of the challenging requirements of modern rechargeable batteries.

Among 5 V cathodes $LiNi_{0.5}Mn_{1.5}O_4$ with a spinel structure attracted most attention, but the impact of the crystal structure (cation ordering, oxygen non-stoichiometry) on the operation mechanism and electrochemical performance still remains the subject of the debates **[Alcántara 2004, Aurbach 2006]**. The goal of this work is to provide a comparative study of high-volt (5 V) spinel materials with general formula $LiM_{0.5}Mn_{1.5}O_4$ (M = Fe, Co, Ni). The structural aspects of these compounds in respect to the cation composition are studied by *ex situ*/*in situ* synchrotron and neutron diffraction. The interplay between morphology and electrochemical performance will

also be considered. Metal dissolution and thermal behavior of the materials will be also discussed.

Chapter 2
Basic electrochemical concepts

Electrochemistry covers all the reactions where electrical energy is produced through chemical processes and in the reverse case electric current induces many chemical reactions **[Pletcher 1991]**.

2.1 Galvanic cells and batteries

A galvanic cell is an electrochemical cell that consists of two dissimilar electrodes (the cathode and the anode) which are electronic conductors, immersed in an electrolyte solution which is an ionic conductor. The spontaneous reaction occurring inside the cell generates electricity. At the interface of the electrodes and electrolyte, the passage of electrical energy is coupled with a chemical reaction which is known as a redox reaction where the electrons transfer from one species to another. In galvanic cell this reaction is divided into two half-cell reactions: release of electrons by the anode (oxidation) and the absorption of electrons by the cathode (reduction).

$$\text{Anode:} \quad bB \Rightarrow dD + n \cdot e^{-} \tag{2.1}$$

$$\text{Cathode:} \quad aA + n \cdot e^{-} \Rightarrow cC \tag{2.2}$$

Both together form the overall cell reaction [**Linden 2002**];

$$aA + bB \Rightarrow cC + dD \tag{2.3}$$

B = negative electrode *A = positive electrode*

n = number of electrons

Both of these electrodes have a specified standard electrode potential, E^0 which could be derived from the thermodynamic data of the reaction. At equilibrium conditions:

$$E^0 = \frac{-\Delta G^0}{n \cdot F} \qquad 2.4$$

$-\Delta G^0$ = standard Gibbs free energy *n = number of electrons*
F = Faraday constant

As the individual electrode potentials cannot be determined in absolute sense, they are always measured with reference to another electrode, which is set as a standard. The normal standard electrode is the standard hydrogen electrode (SHE) (temperature = 25°C, pressure = 1 bar, activity of all active species is unity). For non-standard conditions, the potential of half-cell reactions (*E*) at equilibrium are calculated using the Nernst equation:

$$E_{red} = E^0{}_{red} - \frac{R \cdot T}{n \cdot F} \cdot \ln \frac{a_{red}}{a_{ox}} \qquad 2.5$$

E_{red} = half-cell reduction potential at temperature of interest
E^0_{red} = standard half-cell reduction potential *R = universal gas constant*
T = absolute temperature *a = chemical activity for relevant species*

For a full-cell reaction, the Nernst equation is written as:

$$E_{cell} = E^0{}_{cell} - \frac{R \cdot T}{n \cdot F} \cdot \ln Q \qquad 2.6$$

E_{cell} = cell potential at temperature of interest
E^0_{cell} = standard cell potential (the equilibrium cell potential when all reactants and products are in their standard states)
and *Q,* the reaction constant for a reaction

$$\alpha A + \beta B \leftrightarrow \sigma S + \tau T \qquad 2.7$$

is given by

$$Q = \frac{\{S_t\}^{\sigma}\{T_t\}^{\tau}}{\{A_t\}^{\alpha}\{B_t\}^{\beta}} \qquad 2.8$$

where $\{X_t\}$ denotes the instantaneous activity for a species *X* at a time *t*.

When two or more of the galvanic cells are connected in series or parallel depending on the desired output voltage and capacity, a battery is formed. In general, the batteries could be classified into two categories: primary and secondary. The primary batteries are disposable batteries that could be used only once as the electrochemical reactions taking place inside cannot be reversed under practical conditions. Examples are alkaline batteries and zinc-air batteries. The secondary batteries, also called as rechargeable batteries are reusable on charging (conversion of electrical energy to chemical energy) due to the reversibility of the electrochemical reactions taking place inside. During the discharging the chemical energy acquired will be again transformed into electrical energy. Lead-acid, nickel-cadmium and nickel-metal-hydride batteries are the main examples of secondary batteries. The rechargeable lithium-ion batteries are commercially available since 1991 and represent at the time the most advanced battery technology. In rechargeable batteries, the terms anode and cathode cannot be properly defined as per the convention. The two terms will be mixed depending on whether the cell is being charged or discharged. This confusion is eliminated by categorizing the electrodes as either positive or negative where the terms refer to their corresponding electrode potential. Since this work mainly considers a positive electrode (highest potential), only the reduction process takes place spontaneously (i.e. during cell discharge). Hence the name “cathode materials” is referred to the transition metal-doped, manganese-based spinels investigated in this work. The oxidation reaction takes place only if it is forced externally.

2.2 Characterization of electrochemical cells

The evaluation of performance of electrochemical power sources is done based on many parameters. The theoretical values are different from the practical values. While the theoretical values are calculated from the thermodynamics of electrochemical cell reaction, the calculation of practical values takes into account the mass of the electrolyte, separators, current collectors, terminals and cell housing [**Gritzner 1993**]. In the present work only the weight of active material is considered.

2.2.1 Cell potential

The maximum accessible energy from a cell is the free energy of the reaction ΔG. Hence the selection of electrode materials plays a significant role in determining the obtainable energy. High energy could be achieved by selecting electrodes with

greatest difference of electrochemical potential [**Pletcher 1991**]. The cell voltage is derived from the Gibbs free energy of the corresponding chemical reaction as:

$$U^0 = E^{0,(+)} - E^{0,(-)} = \Delta E^0 = \frac{-\Delta G^0}{n \cdot F} \qquad [\mathrm{V}] \qquad 2.9$$

$E^{0,(+)}$ = positive electrode potential $E^{0,(-)}$ = negative electrode potential

2.2.2 Current density

The current density j is the ratio of the total current flowing through an electrode, I to its surface area A (normally geometric surface area is used).

$$j(t) = \frac{I(t)}{A} \qquad 2.10$$

2.2.3 Charge capacity

The total amount of charge available from a cell is called charge capacity Q.

$$Q = \int_{t_t}^{t_2} I(t) \cdot dt \qquad [\mathrm{Ah}] \qquad 2.11$$

2.2.4 Theoretical specific charge and charge density

The amount of charge per kg of reactants m_i is called theoretical specific charge, q_{th} and is given by:

$$q_{th} = \frac{n \cdot F}{\sum_i m_i} \qquad [\mathrm{Ah/kg}] \qquad 2.12$$

The theoretical charge density, $Q_{V,\ th}$ is calculated by dividing the total charge by volume of the reactants V_i.

$$Q_{V,th} = \frac{n \cdot F}{\sum_i V_i} \qquad \text{[Ah/l]} \qquad 2.13$$

2.2.5 Theoretical specific energy and energy density

Generally these terms are used in order to compare the energy content and energy density content of the cells. The amount of electrical energy delivered per unit mass of a battery is called theoretical specific energy, w_{th} and is given by:

$$w_{th} = \frac{n \cdot F \cdot \Delta E^0}{\sum_i m_i} \qquad \text{[Wh/kg]} \qquad 2.14$$

The theoretical energy density, $W_{V,\,th}$ is obtained by dividing the Gibbs energy change of an electrochemical reaction with the volume of reactants V_i.

$$W_{V,th} = \frac{n \cdot F \cdot \Delta E^0}{\sum_i V_i} \qquad \text{[Wh/l]} \qquad 2.15$$

2.2.6 Specific power and power density

The comparisons of the rate capability of the cells are normally done using the terms specific power p and power density P_V which respectively represents the amount of power delivered per unit mass or unit volume of a cell.

$$p = \frac{I \cdot \Delta E^0}{\sum_i m_i} \qquad \text{[W/kg]} \qquad 2.16$$

$$P_V = \frac{I \cdot \Delta E^0}{\sum_i V_i} \qquad \text{[W/l]} \qquad 2.17$$

2.2.7 The charge-discharge rate

The term charge-discharge rate or C-rate is used to describe the time frame for either a full charge or discharge where *C* denotes the theoretical or nominal charge capacity (Ah) of a cell or battery. Hence C/5 and 2C for example stands for a current theoretically allowing a full discharge in 5 h and ½ h, respectively. The discharge curve is another important feature of battery systems. The delivered capacity and the discharge rate are related to each other as **[Besenhard 1999]**:

$$C = \frac{discharge\ current}{nominal\ capacity} \qquad 2.18$$

Hence by discharging with higher currents, the final capacity obtainable becomes lower.

2.2.8 Rate capability

The term rate capability in this work always refers to the cycling performance of the electrochemical cell at different C-rates.

Chapter 3
Lithium-ion reversible batteries

3.1 Basic principles

The basic working principle of a lithium-ion battery lies on the movement of lithium ions back and forth between the positive and negative electrodes. The name "lithium-ion battery" relates to the fact that no metallic lithium is present inside. The first lithium batteries were assembled with lithium metal as the anode as it is the most effective lithium source and it has the lowest E^0 = -3.04 V vs. SHE [**Mengeritsky 1996**]. These batteries were found to have many disadvantages. The main problem was high thermodynamic instability of lithium in aprotic electrolytes. The decomposed electrolyte passivates the lithium surface and forms a lithium permeable film, solid-electrolyte interface (SEI). The deposition of lithium proceeds irregularly resulting to the so called dendrite formation [**Besenhard 1987**]. These dendrite growth can induce perforations in the separator which brings out cell short-circuit and the energy stored in the cell gets transformed to heat. Explosions and fires could occur due to the low thermal stability of the whole system and high reactivity of lithium [**Reddy 1995, Winter 1998**]. Although metallic lithium cannot be used for commercial batteries due to safety requirements, it is often used as an anode within half-cells in the electrochemical testing of cathode materials. The full cells contain both lithium-insertion compounds as positive and negative electrodes.

In the discharged lithium-ion cell, the positive electrode is a lithium-rich compound and the negative electrode is a lithium-sink one. They are electrically separated by a polymeric membrane which is permeable to the electrolyte. The uptake and release of lithium ions during charging and discharging processes is the source of the net current flowing reaction in a lithium-ion cell. When the cell is charged, the lithium ions

migrate to the lithium-sink compound and get intercalated there. During discharge it gets intercalated back into the positive electrode. Meanwhile the electrons circulate through an external circuit with a release of energy. The electrolyte acts as a medium for transmission of the electro-active lithium ions and is not consumed during operation of the battery.

Until now, the most popular composition of rechargeable lithium-ion battery includes $LiCoO_2$ cathode and graphite anode. A scheme of electrochemical processes in this case is shown in Figure 3.1 and the corresponding electrochemical reactions are given below.

$$\text{Anode:} \quad 6 \cdot C + x \cdot Li^+ + x \cdot e^- \Rightarrow Li_x C_6 \tag{3.1}$$

$$\text{Cathode:} \quad Li_{1-x}CoO_2 + x \cdot Li^+ + x \cdot e^- \Rightarrow LiCoO_2 \tag{3.2}$$

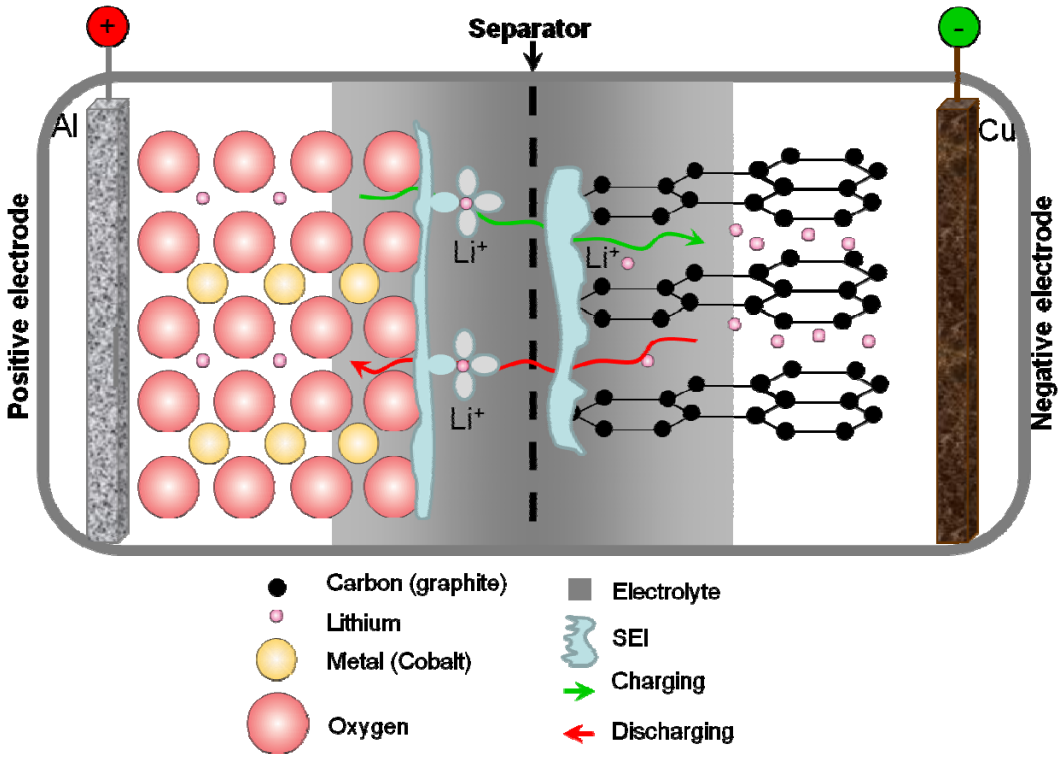

Figure 3.1: *Schematic representation of a lithium-ion cell. The cathode (positive electrode) is the original source of lithium ions and anode intercalates lithium ions only on charging. When discharging, the lithium ions get re-intercalated back in the cathode and leads to the original situation.*

3.2 Applications and advantages

Rechargeable lithium-ion batteries are very versatile and can satisfy the energy needs of many different applications. They show better efficiency and performance compared to other rechargeable batteries. The main advantages of lithium-ion battery over other rechargeable batteries are given below [**Winter 2004, Linden 2002]**:

- High energy density and output voltage
- Much lighter when compared to other energy equivalent, rechargeable batteries
- Selection of operation voltage and chemical system is possible
- Low self-discharge rate
- Cost-saving on waste battery disposal
- Environmentally friendly in comparison with other rechargeable batteries as it is absent from heavy metals like cadmium, mercury etc.
- Can deliver high-current pulses and exhibit long cycle life
- The selection of type is possible based on the area of application such as mobile, stationary or portable.
- Absence of memory effect

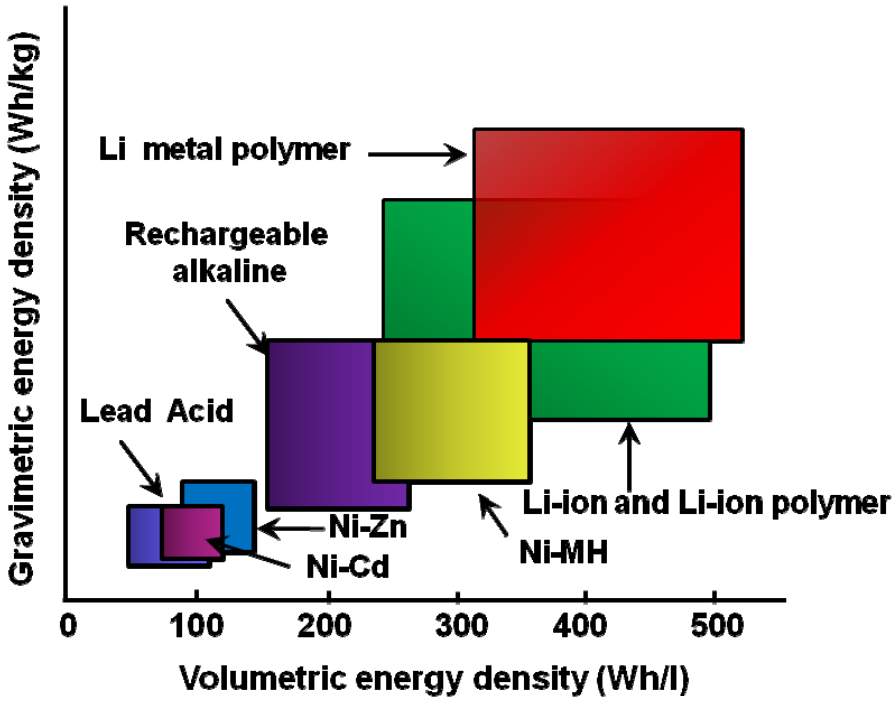

Figure 3.2: *Comparison of different rechargeable battery systems (redrawn from* ***[Winter 2004]****).*

As the lithium-ion batteries are light and compact, they are very attractive energy sources in the portable applications market. Due to the high energy density they can power electronic devices for several hours or days. A comparison of the lithium-ion batteries with other rechargeable batteries are shown in Figure 3.2.

Lithium-based batteries are in the top-right corner of the plot with higher gravimetric and volumetric power density exhibiting their superiority. This represents a huge advantage when portability is taken into account. Stationary applications of lithium-ion batteries include telecommunication. This market is still young and the research is under progress.

Another area of application of the lithium-ion batteries is electric mobility. Hybrid and fully-electric vehicles are proposed as an alternative to combustion engines for decades but are not commonly implemented even now mainly due to the perplexity on their safety and high cost of application. However, this technology is highly relevant and outstanding in this era of diminishing energy resources. One bright example is from Daimler AG which introduced its first hybrid car, the Mercedes-Benz S400 Hybrid, in June 2009 which is claimed to be the first commercial lithium-ion traction battery in a passenger car world wide [**Lamm 2010**]. These developments show that a fully-electric car that could satisfy most of the daily transportation needs is in fact possible with this innovative technology.

3.3 Some issues of current systems and possible improvements

Lithium-ion battery technology is still young and not fully established yet. There are still several issues to be solved to develop it to a fully matured technology.

As far as the electrode materials are concerned, performance problems such as risk of overcharging, discrepancy in the practical charge capacity between anode and cathode materials etc. should be taken into account. The main challenge is to augment both power and energy density simultaneously. The power density could be enhanced by developing materials which can promise a higher charge-discharge rate and the energy density can be improved by widening the potential window with cathode materials that have an intercalation potential of 5 V or more. At this point the issues regarding

electrolytes become more relevant. Present electrolyte solvents are flammable and start oxidizing around 4.5 V and are not very stable at higher voltages. Ionic liquids are proposed as a possible substitute and while exhibiting a higher stability, they lack an SEI formation on the graphite electrode during charging, which is important to protect the electrode from degradation [**McEwen 1999**]. Lithium-polymer batteries are proposed as another solution where a polymeric matrix which is less flammable than conventional electrolyte solvents is used in the electrolyte, which also do not seem to overcome the challenges at their roots.

Two major points require attention concerning safety aspects. First as stated before, the electrolyte solvents catch fire in case of short-circuit due to the release of large amount of energy in the form of heat. One way of preventing this should be replacing the liquid electrolytes with solid-state ceramic electrolytes, but a ceramic material which is superior in terms of conductivity to the conventional liquid electrolyte especially at room temperature is still to be developed[1]. The second point is regarding anode materials. When graphite anodes are intercalated with lithium ions, its potential reaches values near 0.0 V vs. Li/Li^+. At such a low potential the deposition of highly reactive metallic lithium ("lithium plating") may occur. This could be overcome by replacing them with materials like titanium dioxide, which has the properties for high-rate cycling and has an intercalation potential at about 1.5 V vs. Li/Li^+ [**Rosciano 2008**].

Environmental and economic aspects are also crucial for choosing the materials for lithium-ion batteries. From this point of view the most pressing part is the prevention of use of heavy and toxic metals in the cathode materials. Most of the present batteries contain a major percentage of cobalt in the cathode which is toxic, expensive and requires careful recycling. One way to reduce this is by substituting a percentage of this metal by other transition metals such as manganese, nickel etc. or by developing new materials which are either completely free or containing less percentage of cobalt. Examples are $LiFePO_4$, $LiNi_{0.5}Mn_{1.5}O_4$, and $LiNi_{0.5}Co_{0.5}O_2$ etc.

[1] The industry standard electrolyte mixture 1M $LiPF_6$ in EC:DMC, 1:1 wt% (LP30) has a conductivity σ_0 = 9.8 mS/ cm [**Djian 2007**].

3.4 Negative electrodes

At the present time, the most commonly employed negative electrodes are carbon-based because of their low cost, environmental friendliness, good cyclability and reliability [**Winter 1998, Linden 2002, Larcher 2000**]. At the same time also other materials are investigated which include metal alloys (examples are LiAl, $Li_{21}Sn_5$, Li_3Sb etc.), layered oxides ($LiWO_2$, $LiMoO_2$, $LiTiS_2$ etc.), spinel oxides ($Li_4Ti_5O_{12}$) and anatase (TiO_2) and silicon **[Chan 2008]**.

3.4.1 Carbonaceous materials

The carbon-based negative electrodes could be mainly distinguished into two classes: graphitic carbons and non-graphitic carbons. The process of insertion of lithium into these materials is referred as intercalation. The word intercalation is used in a sense that the guest species gets inserted into the host species without resulting in any major structural changes. The graphitic carbon intercalates one lithium atom per six carbon atoms and forms LiC_6 at ambient temperature, see equation 3.1, [**Winter 1998**] and gives rise to a theoretical specific charge capacity of 372 Ah kg^{-1} (based on the weight of carbon). Like metallic lithium, graphite is highly reactive to the electrolyte. In practice, during the first charge, some amount of charge is consumed irreversibly for the formation of an SEI on the electrode surface [**Peled 1979**]. The SEI formation kinetically restrains further electrolyte decomposition, thereby protects the electrode interface from further reduction and allows it to cycle reversibly [**Besenhard 1995, Aurbach 1999, Balbuena 2004, Xu 2004**]. However the irreversible capacity loss in the beginning should be kept to low values as the only lithium source is the positive electrode. Hence the composition of electrolyte is very important as the SEI formation strongly depends on the electrolyte solvent and the salt dissolved in it. Propylene carbonate (PC) which is a common electrolyte solvent, reduces at around 0.8 V vs. Li/Li^+ [**Buqa 2005, Spahr 2006**]. The intercalation of PC solvated lithium ions into graphite takes place at a slightly higher positive potential, which results in a separation of graphene layers and finally leads to an exfoliation of graphite before a stable SEI formation. In the case of ethylene carbonate (EC), the reduction is much faster than PC which results in a fast SEI formation which in turn prevents the further intercalation of solvated lithium ions [**Fong 2009**].

The non-graphitic carbon anodes include mainly hard carbons, which are obtained by the pyrolysis of organic polymer or hydrocarbon precursors [**Ozawa 2009**]. Such carbons show specific charge capacities between *ca*. 200-2000 Ah kg^{-1} depending on the heat-treatment temperature, organic precursor material and electrolyte [**Ozawa 2009**]. The extra lithium capacity of these materials is explained with models that are controversial. The suggestions are mainly availability of larger volume for lithium accommodation, lithium multilayer formation on graphene sheets and storage of considerable amounts of lithium on graphite edges and surfaces in addition to those located between the graphene layers [**Ozawa 2009**]. The main issue with this material is the poor reversibility which leads to poor cyclability [**Winter 1998**].

3.4.2 Non-carbon based materials

Binary or ternary lithium-metal alloys such as tin, silicon, lead, antimony, aluminum and bismuth [**Courtney 1997, Wilson 1995, Bockris 1981, Jow 1982**] are well investigated due to their higher theoretical specific-charge capacities compared to graphite. Problems of these materials arise from the huge volume changes when lithium is intercalated or extracted [**Besenhard 1997**]. This leads to mechanical stress and cracks during cycling which has adverse effect on their cyclability.

Another class of anode materials are titanium containing compounds such as titanium spinel ($Li_4Ti_5O_{12}$) and anatase form of titanium dioxide (TiO_2) [**Sudant 2005, Strobel 1996**]. Due to high diffusion-rate of lithium ions, these materials demonstrate good rate capability. The lithium insertion potentials of these materials are around 1.78 V and 1.56 V vs. Li/Li^+ and this would bring out a low overall cell voltage and poor energy densities [**Sudant 2005, Strobel 1996**]. Nevertheless, these materials, especially $Li_4Ti_5O_{12}$, are of great interest for high-power cells since the above lithium-insertion potential excludes the lithium metal deposition danger at high C-rates, which is in turn an issue with graphitic carbon [**Whittingham 2004**].

Some layered transition metal oxides are also found to be potential candidates for lithium-battery anodes. However, the lithium-intercalation potential of these layered oxides are often much higher than the Li/Li^+ couple. Hence they bring out a highly reduced voltage when combined together in a cell, leading to low power and energy densities [**Winter 1998**].

3.5 Positive electrodes

The currently used positive electrode materials can be divided into three major groups such as

- Layered type oxides
- Metallophosphates with olivine structure and silicates
- Spinel type oxides

The properties of these materials that favor and disfavor their use as positive electrode materials are discussed hereafter.

3.5.1 Layered type oxides

The class of layered oxides can be denoted by a general formula $LiMO_2$, where M can be one or more transition metals. These materials have a structure with oxygen cubic-close packed arrangement which is similar to α-$NaFeO_2$ which belongs to the $R\bar{3}m$ space group (see Figure 3.3). $LiCoO_2$, the most widely used positive material in lithium-ion commercial batteries is a member of this class of materials which exhibits a very good cyclability [**Tarascon 2001, Winter 1998, Whittingham 2004, Linden 2002, Larcher 2000**]. This material was recognized by John. B. Goodenough in 1980 and later patented [**Goodenough**]. However, this material has several drawbacks.

It has high toxicity and low natural abundance and also it is possible only to extract about half of the lithium from this material, above which the structure undergoes phase transitions, and thereby deteriorating the stability and hindering the reversibility of the lithium intercalation, ultimately limiting its charge capacity to 130 $mAhg^{-1}$ [**Ohzuku 1994**]. Later cobalt in this material was substituted with nickel to tackle the cost and safety issue, but the difficulty in synthesis and the very low thermal stability of the resulting $LiNiO_2$ in its charged state has made this material less attractive. Another alternative cathode material was later developed which has a composition of $LiNi_{0.80}Co_{0.15}Al_{0.05}O_2$ (NCA) which provides a slightly higher practical capacity than $LiCoO_2$ (160-180 $mAhg^{-1}$). However, the thermal stability of this material compromises the safety of lithium-ion cells [**Thackeray 2007**].

In order to increase the capacity of the above system, by fully extracting the lithium from the material, without compromising the structural stability, a new class of cathode materials with a general formula $xLi_2MnO_3 \cdot (1\text{-}x)LiMO_2$ (M = Mn, Ni, Co)

was developed [**Thackeray 2007**]. These layered-layered compositions were found to have a capacity >200 $mAhg^{-1}$ and a higher thermal stability than the other available layered systems.

However, oxygen release in the charged state (high potentials) is a drawback of these materials, which leads to issues regarding the thermal safety of the battery **[Wang 2009, Mantia 2008]**.

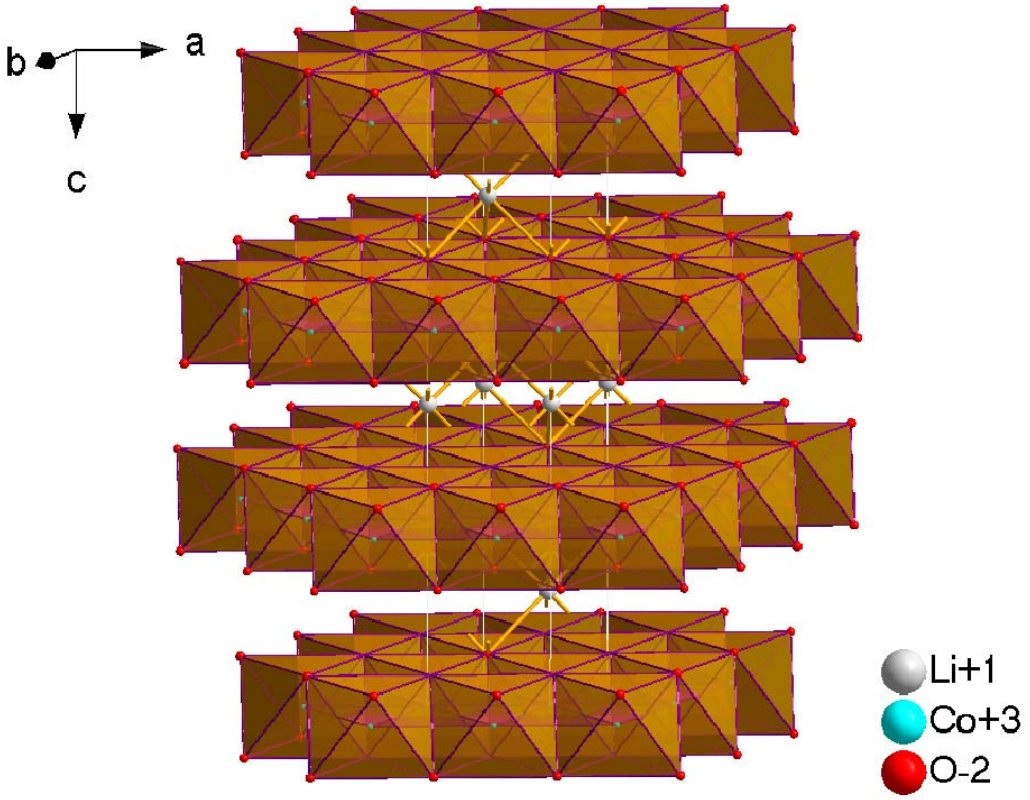

Figure 3.3: *$LiCoO_2$ structure.*

3.5.2 Metallophosphates with olivine structure and silicates

Phosphate-based materials Li*M*PO_4 (*M* = Fe, Mn, Co, Ni) isostructural with olivines have received attention as a new class cathode materials for rechargeable lithium-ion batteries over the past few years [**Wakihara 1998**]. Recently commercialized $LiFePO_4$ has been now considered as a most safe and durable material among lithium-ion battery cathodes. The strong P-O covalent bonds in $(PO_4)^{3-}$ polyanion provide these materials with a highly stable 3D framework (see Figure 3.4), which prevents

the release of oxygen from cathode material structure in the charged state. $LiFePO_4$ is environmentally friendly and can be potentially inexpensive. Nevertheless, the synthesis of high-performance $LiFePO_4$ still remains difficult and requires special approaches to overcome low electronic and ionic conductivity of this compound. Other members of olivine-like metallophosphates family are also attractive due to higher operation voltage. Comparing to $LiFePO_4$, the stability of the delithiated forms $CoPO_4$ and $MnPO_4$ seem to be lower [**Bramnik 2008]**.

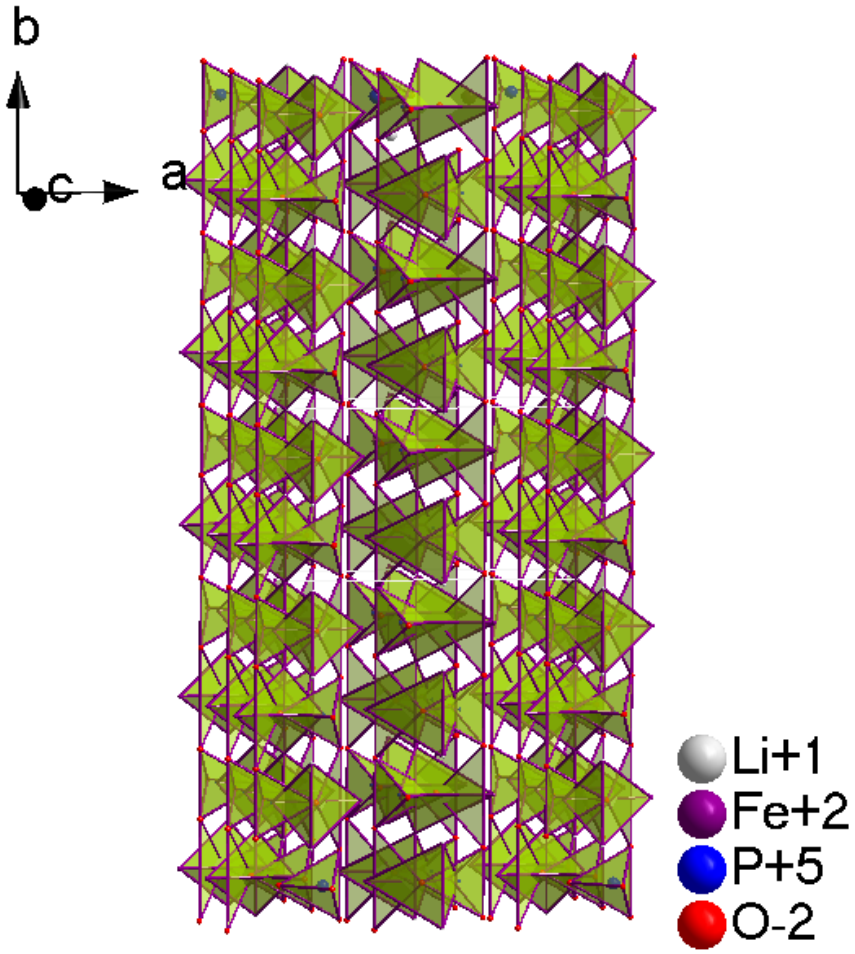

Figure 3.4: *$LiFePO_4$ structure.*

Other polyanion-containing frameworks, which benefit from highly stable covalently bonded XO_4 groups which could reversibly insert and extract lithium are also under investigation. One of the best example is silicates with general formula Li_2MSiO_4 (*M* = Mn, and Co) which could theoretically insert or extract two lithium per formula unit with a theoretical capacity of 330 $mAhg^{-1}$. They are interesting candidates due to their

low cost and high natural abundance. However, the practical capacity is much more reduced due to their characteristically lower electronic conductivity (up to 3 orders of magnitude lower than that of $LiFePO_4$) [**Muraliganth 2010]**.

3.5.3 Spinel type oxides

Researches on the secondary lithium-ion batteries over several years have shown that the materials with three-dimensional frameworks have distinct advantage over compounds with two-dimensional frameworks mainly because lithium diffusion is much easier in a 3D framework than a 2D structure. Among various materials with three-dimensional frameworks, compounds with spinel structure are of extreme interest as cathode materials in rechargeable lithium-ion batteries with high energy density, as revealed by the extensive research works going on in their area. They have a general formula AB_2O_4, where the oxygen atoms occupy 32e site ($Fd\bar{3}m$ space group) and form a face-centered cubic close packing. The A cations occupy tetrahedral 8a site, whereas the B cations are located in octahedral 16d site. The octahedral 16c site remains unoccupied. The spinel structure is shown in Figure 3.5. The original material after which the whole class is named is $MgAl_2O_4$. In general, the spinel oxides suitable as positive electrodes are limited to be those with normal spinel structure, where the lithium ions are located on the 8a site and the transition metal ions on an octahedral 16d site. The 8a and 16d sites form a three-dimensional pathway for lithium diffusion. In the case of inverse spinels, such easy lithium diffusion is hindered due to the displacement of a part or half of the lithium ions on the 8a site by the metal ions from the 16d site. The materials previously studied for lithium intercalation under this class were LiM_2O_4 (M = Ti, V, Mn) [**Wakihara 1998**], out of which manganese based spinels have attracted wide range of attention in the field of lithium secondary batteries because of low costs, acceptable environmental impact, high operation voltage and good transport properties [**Thackeray 1997**].

$LiMn_2O_4$ was first proposed by Thackeray and Goodenough in 1983 [**Thackeray 1983**] and was first commercialized by NEC in 1996 [**Numata 2000, Tsunoda 2000**]. This material is well investigated and as the main focus of this thesis is synthesis and optimization of substituted manganese based spinels as high-volt cathode materials for rechargeable lithium-ion batteries, a detailed review on the advantages and disadvantages of this class of materials together with the investigations done so far and possible improvements available from the literature are given in chapter 4.

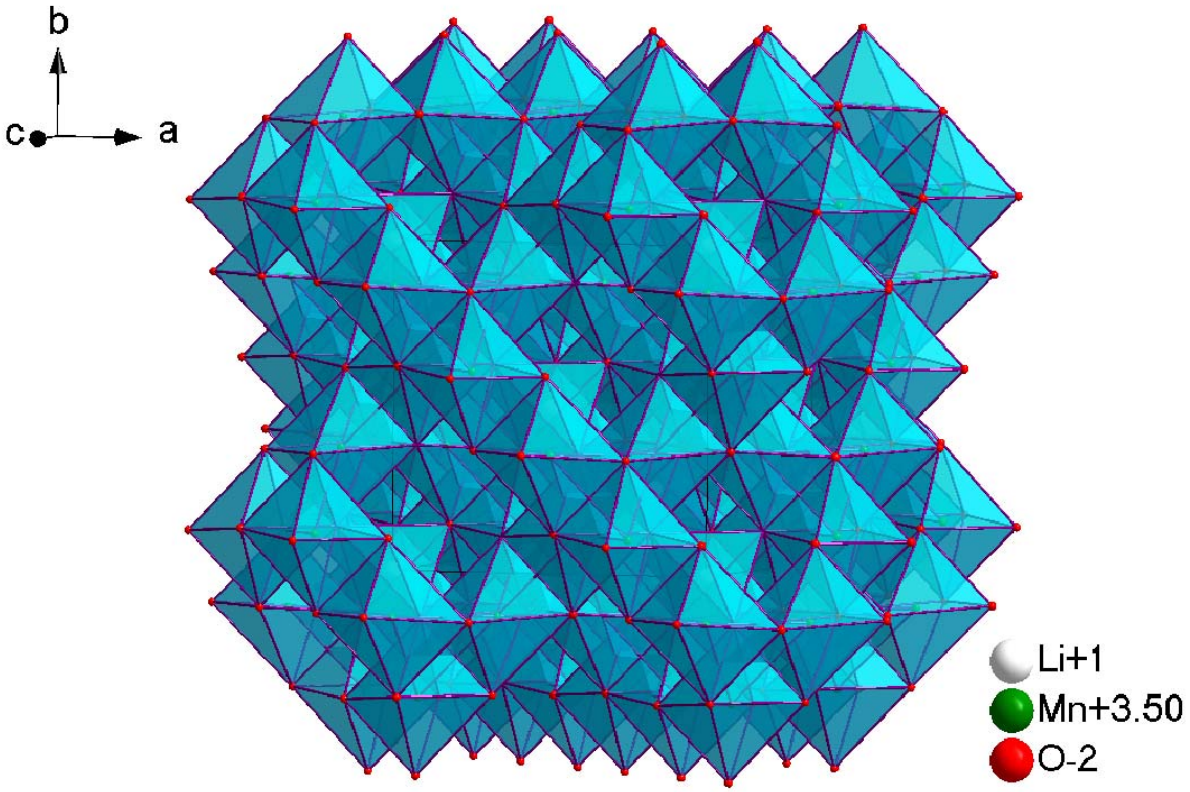

Figure 3.5: *$LiMn_2O_4$ structure.*

3.6 Electrolytes

The term electrolyte in this work stands for a solution of both solvent and a lithium salt.

3.6.1 Properties of lithium-ion battery electrolytes

To use with high-volt cathodes, with potential greater than 4 V vs. Li/Li^+, the electrolyte should be stable and operable in a broad potential range, ideally from 0.0 – 5.0 V vs. Li/Li^+. The main characteristics that a lithium-ion battery electrolyte must satisfy are [**Linden 2002, Xu 2004**]:

- Good ionic conductivity (low internal resistance)
- Good thermal stability (up to 90° C)
- Good compatibility with other cell components
- Low cost, non-toxicity and low flammability

The lithium salts used for electrolytes should also fulfill certain criteria. They should be [**Linden 2002, Xu 2004, Gabano 1983**]

- Able to dissolve and decompose in non-aqueous media
- Inert with the cell components
- Cost effective and non-toxic
- Stable against thermal, oxidative and reductive decomposition

Considering all the above properties, Lithium hexafluorophosphate ($LiPF_6$) is the best candidate so far [**Xu 2004**]. The other available salts are presented here with their drawbacks in brackets: Lithium tetrafluoroborate; $LiBF_4$ (moderate ion-conductivity), lithium perchlorate; $LiClO_4$ (possibly explosive), Lithium hexafluoroarsenate; $LiAsF_6$ (toxic), lithium bis (trifluoromethylsulfonyl) imide (highly corrosive especially with the aluminum current collector). The main classes of electrolytes used or under development in lithium-ion batteries are liquid organic electrolytes, ionic liquids and polymer electrolytes.

3.6.2 Ionic electrolytes

Ionic liquids are salts in the liquid state which have a melting point of <100° C [**Welton 1999, Rogers 2003, Hagiwara 2000, Wasserscheid 2003, Endres 2004**]. Due to their good electrochemical stability at high oxidizing potentials [**Suarez 1997, Golding 2002, Webber 2002, Nishida 2003, MacFarlane 1999, Sun 1998, Forsyth 2003, Fuller 1997, Sato 2004**] and high ionic conductivity [**Hagiwara 2000, Bonhote 1996, Ohno 2002**], they have found applications in lithium-ion and lithium-metal batteries. The other superior properties of ionic electrolytes over organic electrolytes include highly reduced flammability, high thermal [**MacFarlane 1999, Sun 1998**] and chemical [**Wasserscheid 2003**] stability and environmental friendliness. The above properties grant these electrolytes with an enhanced safety of the battery. One of the most promising candidates is an electrolyte containing the ionic liquid salt 1-ethyl-3-methylimidazonium-bis(trifluoromethylsulfonyl) imide (EMI TFSI) with a lithium salt (LiTFSI) [**Holzapfel 2004**].

3.6.3 Polymer electrolytes

In this class of electrolytes, lithium ions are incorporated into a polymer matrix. A typical example of the polymer is polyethylene oxide (PEO). An advantage of these

electrolytes is simplified battery assembly due to the flexibility and solid nature of the polymer. The disadvantage lies in their low ionic conductivity compared to liquid electrolytes.

3.6.4 Liquid organic electrolytes

This class of electrolytes consists of pure or mixtures of organic solvents with a lithium salt dissolved in it. The common solvents used are organic carbonates such as ethylene carbonate (EC), dimethyl carbonate (DMC), diethyl carbonate (DEC), ethyl methyl carbonate (EMC) and propylene carbonate (PC) [**Dominey 1994**]. In addition solvents like γ-Butyrolactone (GBL) are also used. The chemical formulas of the above solvents and their IUPAC names are displayed in Table 3.1.

Table 3.1: *The solvents used for organic electrolyte preparation.*

Electrolyte solvents	IUPAC/ trivial names
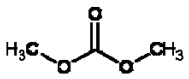	**Dimethyl carbonate (DMC)**
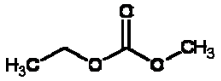	**Ethyl methyl carbonate (EMC)**
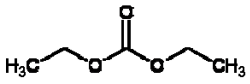	**Diethyl carbonate (DEC)**
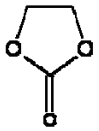	**1,3-dioxolan-2-one/ Ethylene carbonate (EC)**
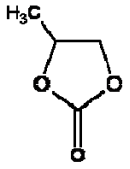	**4-methyl-1,3-dioxolan-2-one/ Propylene carbonate (PC)**
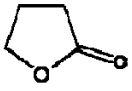	**oxolan-2-one/ γ-Butyrolactone (GBL)**

Chapter 4
Manganese-based spinels as high-volt electrode materials.

4.1 $LiMn_2O_4$ 4 V cathode materials

A second generation of lithium-ion batteries with $LiMn_2O_4$ cathodes was introduced by NEC after the commercialization of this material by them in 1996. This new generation batteries were introduced for electric vehicles (EV) with an improved capacity and elevated-temperature cyclability [**Tsunoda 2000**]. These improvements were mainly attained by addition of small amounts of $LiCoO_2$ or its doped derivatives [**Narukawa 2002**]. Review by Thackeray on different manganese oxides for lithium-ion batteries had a detailed discussion on the advantages and issues with $LiMn_2O_4$ spinels [**Thackeray 1997**]. Lithium can be extracted from this material upon the electrochemical reaction at 4.1 V vs. Li/Li^+ or can be additionally inserted into $LiMn_2O_4$ upon the electrochemical reaction at 3 V vs. Li/Li^+. The reaction is given below:

$$\lambda \cdot MnO_2 \xleftrightarrow{4V} LiMn_2O_4 \xleftrightarrow{3V} Li_2Mn_2O_4 \qquad 4.1$$

The electrochemical reaction at 4 V region (3.5 V – 4.2 V) takes place through a two-step process. First step from x = 1 to x = 0.5 and the second step from x = 0.5 to x = 0 in $Li_xMn_2O_4$. This two-step process is due to the ordering of lithium ions on one half of tetrahedral sites. The reason for the high voltage associated with this process is the high activation energy required for lithium ions to move from one 8a site to another 8a site via the energetically unfavorable neighboring 16c octahedron. The process of lithium extraction and insertion is highly reversible at the 4 V region and the cubic

symmetry of $Li_xMn_2O_4$ ($0 \leq x \leq 1$) electrodes remain unaffected. The lattice parameter varies from 8.245(1) Å in $LiMn_2O_4$ to 8.029 Å Mn_2O_4 over a compositional range ($0 \leq x \leq 1$). The unit-cell contraction and expansion by 7.6% in the 4 V region is gradual and isotropic which provides a structural stability to this material during cycling. This material shows high capacity retention at RT but a very high fatigue at elevated temperatures [**Thackeray 1997**]. The following reasons are argued for this high fatigue [**Gummow 1994**]:

- Manganese dissolution from the spinel cathodes, especially when the electrolytes contain very small amount of acidic species (HF is found very common with $LiPF_6$ based electrolytes, in the presence of a few ppms of water). This dissolution occurs on extensively lithiated particles, with a high concentration of Mn^{3+} and via a disproportionation reaction as follows,

$$2Mn^{3+}{}_{(solid)} \rightarrow Mn^{4+}{}_{(solid)} + Mn^{2+}{}_{(solution)} \qquad 4.2$$

- The extensively delithiated spinel electrodes are highly oxidizing, especially with the organic electrolytes and this reaction gets enhanced in the presence of a carbon conductive additive in the positive electrode and will also result in manganese dissolution [**Gummow 1994**].

- At the end of a discharge, the material is prone to Jahn-Teller distortion, especially in an over discharged composition, where the average oxidation state of manganese ions reach below 3.50.

At 3 V, additional lithium insertion to $LiMn_2O_4$ takes place via a two-phase, constant-voltage electrochemical reaction. During this process, lithium ions are inserted into the octahedral 16c sites of the spinel structure. As the 16c octahedra shares faces with the 8a tetrahedra, the electrostatic interactions between the lithium ions in these two sets of sites cause a displacement of the lithium from the tetrahedral site to the neighboring unoccupied 16c octahedral site, resulting in the formation of rock-salt $Li_2Mn_2O_4$ on the surface of electrode particles. The cycling in 3 V region results to fast capacity fading. The reason for that is a Jahn-Teller distortion. It is caused as a result of increased concentration of Mn^{3+} (d^4) ions in the Mn_2O_4 spinel framework which reduces the crystal symmetry from cubic (c/a = 1) to tetragonal (c/a = 1.16).

This 16% increase of the c/a ratio is too high for the spinel electrode to withstand the electrochemical cycling of lithium in and out of the structure. The strain in the structure prevents the spinel particles from maintaining the structural integrity and they tend to break up and lose electrical contact, which in turn leads to a quick capacity loss of the cells [**Thackeray 1997**].

In order to circumvent the above mentioned factors to an extent, slight modification in the composition of the above materials was performed. Initially a small fraction of the manganese was replaced by lithium in the framework which has a general formula $Li_{1+\delta}Mn_{2-\delta}O_4$ ($0 < \delta < 0.33$) [**Gummow 1994, Thackeray**]. For example, when the value of $\delta = 0.03$, the average manganese oxidation state is increased to +3.54. Even though there is a disadvantage of lowering of theoretical capacity (drop from 148 $mAhg^{-1}$ to 136 $mAhg^{-1}$) as only 0.91 Li^+ ions can be extracted from the structure successfully; this lithium substitution will combat the Mn dissolution and the onset of Jahn-Teller distortion. Later this process of substituting a portion of manganese ions with monovalent ions was extended to divalent and trivalent ions such as Mg^{2+} [**Gummow 1994**], Ni^{2+} [**Guohua 1996, Amine 1996, Gao 1996, Zhong 1997**], Zn^{2+} [**Gummow 1994**], or Co^{3+} [**Kawai 1998a**], Cr^{3+} [**Guohua 1996, Sigala 1995, Robertson 1996**], Fe^{3+} [**Gummow 1994, Thackeray**] which gave rise to materials with a general formula $LiM_xMn_{2-x}O_4$ (*M* = Ni, Co, Cr, Fe, Zn etc. and $0 \leq x \leq 1$). Detailed discussion on these substituted materials will be given in the next section.

4.2 Motivation and goal of the work: 3d transition metal (*M*) substituted $LiMn_{2-x}M_xO_4$ 5 V spinels

The substitution of Mn in $LiMn_2O_4$, especially with Ni^{2+}, Co^{3+} and Fe^{3+} was shown to result to the electrochemical reaction of doping metal in 5 V regions [**Amine 1997, Kawai 1998a, Kawai 1998b**]. Several compositions of these doped spinels were studied and out of this the Ni substituted spinel with a Ni: Mn ratio 1:3 was of greatest interest as the substitution will raise the whole electrochemical activity into 5 V region. In contrast, the substitution with Co or Fe will lead to the oxidation of only a part of the manganese to Mn^{4+}. The distribution of oxidation states of the metal ions in a composition $LiM_{0.5}Mn_{1.5}O_4$ (*M* = Fe, Co, Ni) is given as:

- for M = Ni: $Li^{+}Ni^{2+}_{0.5}Mn^{4+}_{1.5}O_4$ (the lithium extraction occurs via $Ni^{2+/}Ni^{4+}$ reaction in 5 V region, **[Kim 2004b]**)
- for M = Co: $Li^{+}Co^{3+}_{0.5}Mn^{4+/3+}_{1.5}O_4$ (lithium extraction occurs via Mn^{3+}/Mn^{4+} reaction in 4 V region and Co^{3+}/Co^{4+} reaction in 5 V region **[Aitchison 1999]**)
- for M = Fe: $Li^{+}Fe^{3+}_{0.5}Mn^{4+/3+}_{1.5}O_4$ (lithium extraction occurs via Mn^{3+}/Mn^{4+} reaction in 4 V region and Fe^{3+}/Fe^{4+} reaction in 5 V region, [**Ohzuku 2001**])

A different composition with Co substituted spinel ($LiCoMnO_4$) exists where all the Mn remains in its tetravalent form, but attempts to obtain such a composition for Ni and Fe substituted spinel were never successful [**Amine 1997**]. Though this material with Co: Mn ratio 1:1 has advantages like absence of trivalent Mn ions, the high amount of Co, which means increased cost and toxicity make this material less interesting. This was the main reason for the selection of substituted manganese based spinels of the composition $LiM_{0.5}Mn_{1.5}O_4$ (M = Fe, Co, Ni) in this work.

The major synthesis methods available for these materials are solid-state [**Kawai 1998a, Kawai 1998b, Yoon 2007**] and sol-gel routes. Out of these, the sol-gel synthesis is more attractive as it is a low-temperature synthesis method which results in high homogeneity of the products and provides a good control over the stoichiometry [**Amine 1997**]. A citric acid assisted sol-gel method (Pechini method) introduced by Liu et al. [**Liu 1996**] for the synthesis of $LiMn_2O_4$ was later adapted by many groups to synthesize the spinel structures [**Kunduraci 2008**].

4.2.1 $LiM_{0.5}Mn_{1.5}O_4$ (M = Fe, Co, Ni): crystal structures

Depending on the cation distribution $LiNi_{0.5}Mn_{1.5}O_4$ has two crystallographic forms: cation-ordered spinel ($P4_332$ space group) and cation-disordered spinel ($Fd\bar{3}m$ space group), see Figure 4.1. No cation ordering was reported so far for all other compounds of the stoichiometry $LiM_{0.5}Mn_{1.5}O_4$ (M = Fe, Co, Cr).

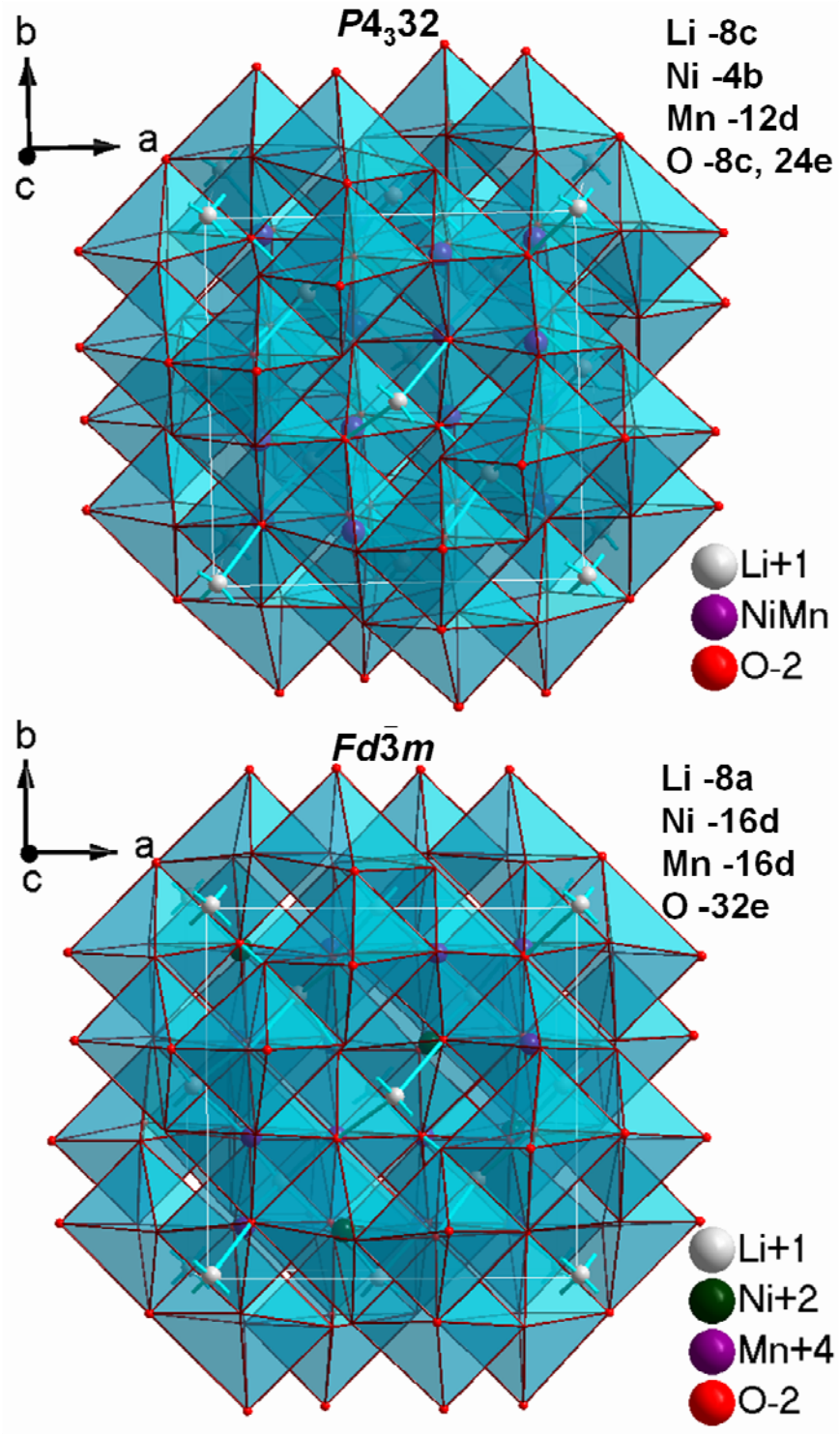

Figure 4.1: *$LiNi_{0.5}Mn_{1.5}O_4$ structures based on $P4_332$ and $Fd\bar{3}m$ space groups. The cation distribution is shown in the inset of each figure.*

According to the recent study of Pasero et al., the disordered structure is oxygen-deficient $LiNi_{0.5}Mn_{1.5}O_{4-\delta}$ ($0.05 \leq \delta \leq 0.18$), which transforms reversibly into oxygen-

stoichiometric spinel upon oxygen uptake. The ordered and disordered modifications of $LiNi_{0.5}Mn_{1.5}O_4$ differ with respect to their electrochemical behavior and observed phase transitions during lithium insertion and extraction **[Kim 2004a, Takahashi 2004, Ariyoshi 2004]**. The cation-ordered spinel can be obtained at relatively low annealing temperatures ≤600°C [**Pasero 2008**]. An annealing above 700°C leads to an oxygen loss from the spinel structure and cation disordering that results in an oxygen-deficient structure and is always a cation-disordered structure. In 2008, Pasero et al. have developed a method to analyze the amount of oxygen deficiency in $LiNi_{0.5}Mn_{1.5}O_4$ and found that this amount, δ, in $LiNi_{0.5}Mn_{1.5}O_{4-\delta}$ has a strong influence on the cation ordering and structural stability of this material. According to their work when $\delta > 0.005$, the cation-ordered spinel changes to a disordered structure and with $\delta > 0.07$, an additional rock-salt phase ($Fm\bar{3}m$ space group) is formed [**Pasero 2008**]. More insight into the cation ordering was obtained by neutron diffraction. The differences in the coherent neutron scattering lengths of manganese (-3.73 fm) with the substituted transition metal elements (Co: +2.50, Ni: +10.3, Fe: +9.45 fm) [**Sears 1984**] makes the investigation of their cation ordering easy with neutron diffraction. No such information could be obtained from XRD due to similar scattering powers of the ordered cations. Except for a work done by Pierre et al. in 2003, not much attempts were made to investigate the 3d cation ordering in $LiCo_{0.5}Mn_{1.5}O_4$ spinel. According to their report, no cation ordering was observed for the trivalent ion (Co or Ga or Ti) substituted spinels **[Pierre 2003, Strobel 2003**] and so far to the knowledge of the author no information is available about $LiFe_{0.5}Mn_{1.5}O_4$. This lack of information lead to the detailed structural investigation of the synthesized $LiM_{0.5}Mn_{1.5}O_4$ (M = Ni, Co, Fe) in this work with combined XRD and neutron diffraction techniques. The oxygen non-stoichiometry and their effect on the structure stability and electrochemical behavior of $LiM_{0.5}Mn_{1.5}O_4$ (M = Co, Fe) is still an open question and initial attempts are made to answer these questions in this work.

4.2.2 $LiM_{0.5}Mn_{1.5}O_4$ (M = Fe, Co, Ni): phase transition upon cycling

$LiNi_{0.5}Mn_{1.5}O_4$ was investigated for its cycling mechanism in the 5 V region by several research groups through *in situ* or *ex situ* diffraction or X-ray absorption techniques. According to Mukerjee et al., the Ni-doped spinel exhibits three phase co-existence in the 5 V region with minimal lattice parameter changes within each phase [**Mukerjee 2004**]. Another work came out of Kim et al. in 2004 with *ex situ* XRD illustrates that the mechanism of $LiNi_{0.5}Mn_{1.5}O_4$ spinel is completely dependent on the

initial crystal structure of the material. If the material has a cation-ordered structure in the beginning, belonging to the $P4_332$ space group, then during lithium extraction from the host lattice, a phase with cation-disordered structure is formed (space group $Fd\bar{3}m$). When lithium extraction continues, an additional phase change was observed from the $Fd\bar{3}m$ space group to another cubic structure. For the material with initial cation-disordered structure, with $Fd\bar{3}m$ space group, only the transformation to the cubic structure takes place as similar to the last step phase transition for the ordered spinel. The reason for this phase transitions was explained as a migration of the cations accelerated by the vacancies created by lithium ions. The phase transitions were found reversible during lithium re-intercalation which indicates the reversibility of the cation migration [**Kim 2004b**]. Some additional works have shown their structural changes in wider voltage ranges [**Park 2007, Ariyoshi 2004**]. Hence the charge-discharge mechanism is through a topotactic two-phase transition for the disordered, $Fd\bar{3}m$, $LiNi_{0.5}Mn_{1.5}O_4$ spinel and via a topotactic three-phase transition for the ordered, $P4_332$, $LiNi_{0.5}Mn_{1.5}O_4$ spinel when cycled in the voltage range 3.5 – 5.0 V [**Kim 2004a**].

However, the structural changes during cycling in the 5 V region for $LiM_{0.5}Mn_{1.5}O_4$ (M = Co, Fe) are not comprehensively investigated, though proposals were made for a solid-solution mechanism of $LiCo_{0.5}Mn_{1.5}O_4$ in the 4 V region [**Wohlfahrt-Mehrens 1997**]. In 2001 Ozhuku et al. have reported on a Mössbauer spectroscopic study on the electrochemical reaction mechanism in $LiFe_{0.5}Mn_{1.5}O_4$ where they confirmed the reaction Fe^{3+}/Fe^{4+} in the 5 V region during charging, but no structural evolution was investigated [**Ohzuku 2001**]. These missing points were the motivation to elucidate the structural changes during cycling for $LiFe_{0.5}Mn_{1.5}O_4$ and $LiCo_{0.5}Mn_{1.5}O_4$ using *in situ* synchrotron diffraction methods.

4.2.3 $LiM_{0.5}Mn_{1.5}O_4$ (M = Fe, Co, Ni): cycling behavior

In the initial investigations, Ni substitution was found to improve the cyclability of the $LiMn_2O_4$ spinels particularly by suppressing the Jahn-Teller effect and manganese dissolution. In addition, $LiNi_{0.5}Mn_{1.5}O_4$ also exhibited enhanced cyclability at elevated temperatures compared to its parent compound [**Okada 2000**]. However, in the literature, different data are available regarding the cyclability of $LiNi_{0.5}Mn_{1.5}O_4$. In 2006, Aurbach et al. [**Aurbach 2006**] reported that this material develops a

passivating layer at the surface, an SEI, which protects the material from any reaction with the electrolyte and results in good capacity retention, even for nanoparticles and at elevated temperatures. Nevertheless, in numerous publications the cyclability of $LiNi_{0.5}Mn_{1.5}O_4$ in conventional electrolytes was reported to be poor, which initiated different approaches to improve the cyclability, like coating or doping [**Alcántara 2004, Sun 2002b, Fan 2007, Aklalouch 2008**]. In 2002, Sun et al. have reported a work on ZnO coated $LiNi_{0.5}Mn_{1.5}O_4$ cathodes. According to this report, the $LiNi_{0.5}Mn_{1.5}O_4$ material they synthesized via a sol-gel method exhibited only ~7% of its initial capacity after 50 cycles, when cycled at a rate of C/3 and with an electrolyte 1M $LiPF_6$ in EC: DMC (1:2) whereas 1.5% ZnO coated material exhibited more or less no capacity fade after 50 cycles when cycled at the same conditions [**Sun 2002b**]. The reason for this enhanced capacity retention was proposed as suppression of Mn dissolution by reduction of HF formation. Locati et al. have reported in 2007, that Mg-doping improves the rate capability of this material [**Locati 2007**]. Later in 2008, Aklalouch et al. have found that certain amount of Cr-doping also improves its electrochemical performance [**Aklalouch 2008**]. Several groups tried to synthesize nano $LiNi_{0.5}Mn_{1.5}O_4$ and found that in nanoscale these materials exhibit enhanced rate capability and high-rate cyclability [**Shaju 2008, Arrebola 2006a**]. Nevertheless, nanoparticles are of less interest in commercial applications due to their low volumetric capacity and increased available surface for parasitic reactions.

About the cyclability of the $LiM_{0.5}Mn_{1.5}O_4$ (M = Co, Fe) compounds, it is known that the performance at 4 V was improved by the substitution of these 3d transition elements [**Wohlfahrt-Mehrens 1997, Wang 2003, Zhao 2009, Kim 2003**]. Though they are known as 5 V materials since 1998 [**Kawai 1998a, Kawai 1998b, Ohzuku 1999, Song 1998, Eftekhari 2003**], there is only limited information available concerning their cycling behavior. In 2003, Eftekhari, in the work done on thin film $LiFe_{0.5}Mn_{1.5}O_4$ cathodes, reported that at 55°C, this material lose >50% of its initial discharge capacity after 50 cycles when cycled at a rate of C/10 in a potential range 3.0 - 5.3 V with 1M $LiPF_6$ in EC:DMC (3:7) as the electrolyte. An improvement of the capacity retention to ~79% after 50 cycles was reported in the same work by using an electrolyte 1M $LiBF_4$ in EC: DMC (3:7) at the same cycling rate, temperature and voltage range [**Eftekhari 2003**]. One of the possible suggestions for the former degradation was given as manganese dissolution or a surface contamination, as a result of electrolyte decomposition at the electrode surface during the high-volt

performance which leads to the formation of carbonaceous species on the surface. The generation of high valent transition metal species, here Fe^{4+}, will also lead to side reactions that indeed result in the formation of carbonaceous films on the surface. Later in 2004, Eftekhari has reported ~82% retention of the initial discharge capacity after 100 cycles for thin film $LiFe_{0.5}Mn_{1.5}O_4$ as a 5 V cathode with a solid electrolyte, LIPON, with a special cell design and at a rate of C/10. He also reported an improvement of the capacity retention to 95% after 100 cycles when a metal oxide layer is placed between the cathode and solid electrolyte [**Eftekhari 2004**]. Apart from his works, not much works are available which show a good performance for $LiFe_{0.5}Mn_{1.5}O_4$ as a 5 V cathode, especially with conventional electrolytes. Similarly, not much information is available about the cyclability of $LiCo_{0.5}Mn_{1.5}O_4$.

A work came out of Caballero et al. in 2005 states that the annealing temperature has a strong influence on the cyclability of spinel materials independent of the doped cations. The study was dealing with Cr, Ni, Cu substituted $LiMn_2O_4$ spinels. According to this work the low-temperature synthesized materials (500°C) exhibited an inferior cyclability in comparison with the high-temperature synthesized materials (800°C). They have investigated the reasons for this behavior and concluded that the low-temperature treated materials contain excess oxygen in the lattice, (nominal composition of $Li M_x Mn_{2-x}O_{4+\delta}$ (M = Cr, Ni, Cu), which is released when cycled above 4.5 V. This oxygen loss may lead to structural damage on the crystal surface and have an adverse effect on the cyclability and may lead to overcharge in the electrochemical cells **[caballero 2005]**. As the synthesis temperature has a clear influence on the cyclability, materials treated at two different temperatures were investigated in this work.

Storage behavior and ageing processes are important in determining the life of a battery. In a normal lithium-ion battery the active material remains always in contact with the electrolyte. Hence it is important to consider the influence of electrolyte contact on the active material (cathode and anode materials). In 2006, Aurbach et al. have published a study on ageing, interfacial reactions and cycling behavior of $LiNi_{0.5}Mn_{1.5}O_4$ through combined electrochemical and spectroscopic analyses. According to them, the loss of capacity with prolonged cycling of this material was not due to a structural degradation, but as a result of formation of surface films. A precipitation of LiF, C-F and PF_X species was observed on the surface with the help of

XPS. They have observed that this surface chemistry is completely dependent on the temperature of treatment. The $LiNi_{0.5}Mn_{1.5}O_4$ active material, in contact with the electrolyte is stable at 30°C, whereas at high temperatures, above 60°C, there are local changes in the structure due to manganese and nickel dissolution [**Aurbach 2006**]. Another work came out in 2006 and was also adding proof to the metal-ion dissolution from this material in the electrolyte [**Choi 2006**]. Due to the strong influence of ageing or storage stability, which also includes metal-ion dissolution, on the electrochemical behavior of the battery materials, these parameters are thoroughly investigated for the $LiM_{0.5}Mn_{1.5}O_4$ (M = Ni, Co, Fe) materials in this work, in their charged as well as discharged states at different temperatures.

Chapter 5
Experimental part

5.1 Synthesis of Li$M_{0.5}Mn_{1.5}O_4$ (M = Fe, Co, Ni)

The synthesis of Li$M_{0.5}Mn_{1.5}O_4$ (M = Fe, Co, Ni) was carried out using a citric acid assisted Pechini synthesis similar to the work reported by Liu et al. [**Liu 1996**]. The process is based on the ability of some weak acids to form polybasic chelates with various cations. These chelates, when heated in a polyhydroxylalcohol undergoes polyesterification and hence results in the formation of a solid polymeric resin in which the cations are uniformly distributed. This resin can be then calcined to get phase-pure oxides. The reaction scheme for this process is shown in Figure 5.1 (modified from [**Liu 1996**]). For the synthesis of the transition metal-doped, Mn-based spinel samples, first citric acid (Applichem, 98%) was dissolved in ethylene glycol (BDH Prolabo, 100%) in a 1:4 molar ratio. Stoichiometric amounts of Manganese (II) acetate tetrahydrate, $C_4H_6MnO_4.4H_2O$ (Fluka, 99%), Lithium acetate dihydrate, $C_2H_7LiO_4$ (Alfa Aesar, reagent grade) and corresponding metal acetate, that is for Fe: $C_4H_6FeO_4$ (Alfa Aesar), for Co: $C_4H_6CoO_4.4H_2O$ (Fluka, 99%) and for Ni: $C_4H_6NiO_4.4H_2O$ (Fluka, 99%), respectively, were added to the above solution and dissolved, by stirring. When the temperature of the resulting solution was increased to 140°C, the viscosity started gradually increasing. The excess ethylene glycol in the solution was then evaporated by increasing the hot plate temperature to 180°C. The viscous transparent gel then obtained was precalcined at 400°C for 3 h with a heating rate of 10°C/minute and ground in a mortar to get the initial precursors, which were black powders in appearance.

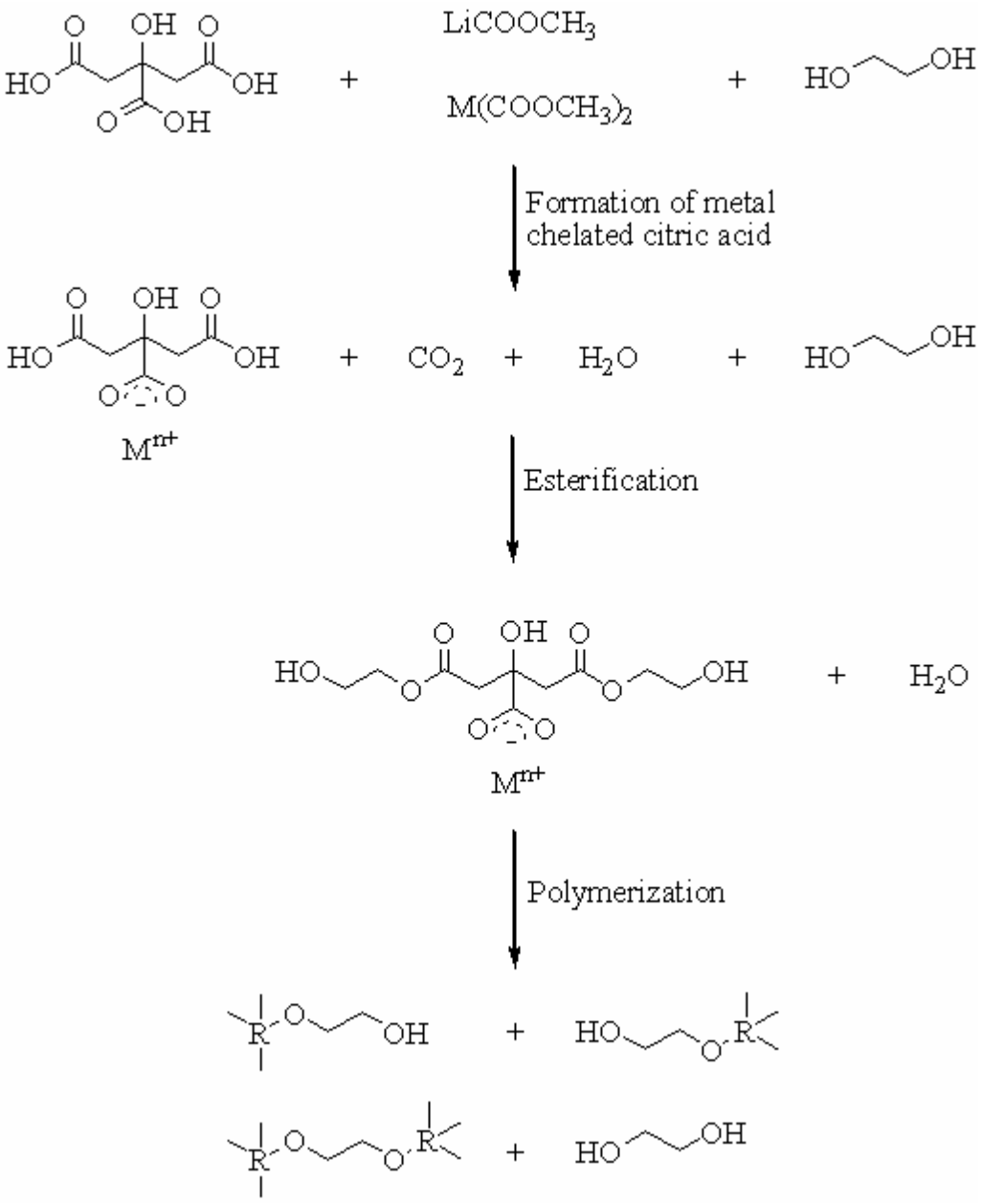

Figure 5.1: *The reaction scheme for the preparation of organic precursors during Pechini synthesis of $LiM_{0.5}Mn_{1.5}O_4$ (M = Mn and Fe or Co or Ni).*

All the calcinations were performed in a furnace using alumina crucibles. Two different thermal treatments were used to produce two sets of samples. One set was produced by annealing the initial precursor at 600°C for 24 h with intermittent grinding and with a heating rate of 5°C/min, hereafter referred as $LiM_{0.5}Mn_{1.5}O_4$-600 (*M* = Fe, Co, Ni) . The second set was prepared by reannealing a part of the $LiM_{0.5}Mn_{1.5}O_4$-600 (*M* = Fe, Co, Ni) with the maximal power of the furnace up to 1000°C with a heating rate of ~10°C/min and with a holding time of <1 min, hereafter

referred as Li$M_{0.5}Mn_{1.5}O_4$-1000 (M = Fe, Co, Ni). The very low holding time prevents any extensive oxygen deficiency. In both the cases, the samples were cooled down to room temperature without explicit temperature control. As the latter method is not a well defined route, the structural characterization including lattice parameter calculation was performed with XRD for every batch of synthesized materials used for different experiments and will be displayed in the context.

All other syntheses methods used other than for the root material will be discussed in the corresponding sections.

5.2 Characterization techniques

5.2.1 X-ray and neutron powder diffraction

The crystal structures of the materials were initially identified using X-ray powder diffraction with a STOE STADI/P powder diffractometer (Mo-Kα_1 radiation, curved Ge (111) monochromator, step width 0.02° (2θ), linear PSD, Position Sensitive Detector, counter. The reasons for the use of Mo-Kα_1 radiation over Cu radiation are high intensity and less absorption especially in the case of iron containing samples. Normally, the as prepared materials and end products from thermogravimetric treatments were measured in flat-sample transmission mode. The samples were ground in a mortar and glued in between the centre of two circular acetate foils. The foils were then fixed to a flat-sample holder using two tiny screws and with a metal cover slip having a hole in the middle for the free passage of the X-ray beam. In the case of most of the electrochemically treated samples, a method which involves a Debye-Scherrer mode using capillaries was adopted so as to prevent any contacts with atmospheric air and moisture. The capillaries used were made of glass and with diameter varying from 0.3 - 0.5 mm. They were filled with the sample to be analyzed, inside an argon-box and sealed temporarily before taking out. These capillaries were then fused under flame outside the box, hence to introduce a permanent, tight sealing. These prepared samples were then mounted on a sample holder and rotated during the measurement to obtain better powder statistics.

XRD cannot provide complete information about the cation distribution in the structure of Li$M_{0.5}Mn_{1.5}O_4$ (M = Fe, Co, Ni) because of the low scattering ability of

lithium atoms and the close resemblance of the Mn and "*M*" X-ray atomic form factors. Therefore, the $LiM_{0.5}Mn_{1.5}O_4$ (*M* = Fe, Co, Ni) samples were also characterized by neutron diffraction, which benefits from a stronger scattering from the lithium ions and very significant differences in the scattering lengths of Mn and the other 3d-metals. The neutron data were obtained at the SPODI powder diffractometer (research reactor FRM II, Garching). The datasets were collected with monochromatic neutrons of wavelength 1.546(3). A vanadium can was used as a sample holder as it is nearly invisible in a neutron diffraction experiment due to its negligible absorption and coherent scattering cross section for neutrons. X-ray and neutron powder diffraction data were collected at room temperature and used simultaneously for the structure refinement for the 600°C annealed samples by the Rietveld method with the FullProf software package. The standard deviations of all refined parameters were calculated in agreement with Berar and Lelann [**Berar 1991**].

5.2.2 Scanning electron microscopic studies

A scanning electron microscope Philips XL-30 FEG was used to investigate the particle morphology. The sample preparation includes spreading a small portion of the already ground powder onto a conductive carbon tape which can be sticked on a SEM pin stub, which later can be mounted on a specimen holder. After the specimen was mounted, the chamber was evacuated and images were taken. The acceleration voltage and spot size were varied for different experiments to obtain better images.

5.2.3 Inductively coupled plasma-optical emission spectroscopy

The chemical composition of the materials was analyzed by ICP-OES using an IRIS Intrepid II XUV, Thermo Fisher spectrometer. The samples were dissolved in concentrated hydrochloric acid or nitric acid in order to perform the analysis. Each of the samples was divided into three portions and all these portions were analyzed independently in order to check the reproducibility of the measurements. Therefore, the values are always reported as an average of the three values and in most cases, with their standard deviation in the brackets.

5.2.4 Thermogravimetric analysis

Thermal behavior and oxygen deficiency studies were carried out using simultaneous TG-DTA analyses. DSC measurements were also performed in the thermal stability experiments. The experiments were performed with a Model STA 449 apparatus (Netzsch, Selb, Germany) or Netzsch TG 209 F1 Iris analyzer. Measured weights of samples were taken in an alumina crucible (for TG-DTA) or Pt-Rh crucible (for DSC) and heated to a specified temperature with a dedicated heating rate. Cooling experiments were also performed in oxygen deficiency analyses in order to check the reversibility of the process. All the measurements were carried out with reference to a standard material which was the same crucible.

5.2.5 X-ray photoelectron spectroscopic analysis

A quasi-*in situ* X-ray photoelectron spectroscopy as similar to the work done by Oswald et al. [**Oswald 2009**] was performed to investigate the chemistry of surfaces and the valence state of surface species in $LiM_{0.5}Mn_{1.5}O_4$-600 (M = Fe, Co, Ni) cathodes in the fresh state and after electrochemical treatments. For the fresh cathodes about 10 - 15 mg of the cathode mixtures of the ratio 80: 15: 5 for material: carbon black: PVDF were pressed on an aluminum grid at 5 tons and dried at 110°C for 1 h. The cathodes prepared above were then cycled at RT at 1C for 50 cycles , dismounted in the glove box and washed with DMC several times (to remove residual $LiPF_6$) to prepare the second set of samples for XPS.

The X-ray photoelectron spectra were obtained on a PHI 5600 CI (physical electronics) spectrometer, with a monochromatic Al Kα excitation (350W); in most cases combined with a low energy electron charge neutralizer. The spectrometer is equipped with a hemispherical analyzer operating at typical pass energy of 29 eV and an analysis area of 800 μm. A dedicated transfer chamber (Physical Electronics) was used to transport the samples from the argon-box (with O_2 and H_2O levels less than 1 ppm) to the X-ray photoelectron spectrometer so that any contact with air and moisture is avoided. Occasionally a surface scraping with a diamond coated file was carried out inside the argon-box before transfer to prepare more “bulk-like states”.

5.2.6 Transmission electron microscopic studies

In order to confirm the presence of coatings, transmission electron microscopic investigations were performed at high resolution either with a Philips CM20 TEM with an acceleration voltage of 200 kV or with a JEOL JEM-3010 TEM operating at acceleration voltage of 300 kV, both with a LaB_6 cathode. Sample preparation for this application was performed by suspending the material powder in acetone and depositing a drop of the suspension on a standard copper grid covered with carbon.

Chapter 6
Electrochemical experiments

This part of the work is mainly focused on the preparation methods of electrodes, their optimization and the techniques used to study the electrochemical performance. Cell construction and electrochemical instrumentation is also a part of the discussion.

6.1 Electrochemical cell

The electrochemical investigations were performed using two electrode electrochemical cells. Swagelok-type cells were used during this work (see Figure 6.1 a). The cell used for most of the measurements consisted of two cylindrical current collectors, made of stainless steel on the anode and cathode sides, a cell body made of Teflon (includes two screws and a middle part) and four o-rings made of Teflon. Two o-rings each were used on both sides of the cell in order to seal it hermetically. The cells were assembled in an argon-filled glove box. The working and counter electrodes were placed in the cell, separated by electrolyte-soaked separators (~300 µL electrolyte was used), on the two current collectors. The cell is then sealed and the voltage was checked with a multimeter to detect any unsuccessful assembling.

For the *in situ* synchrotron diffraction measurements, slightly modified Swagelok-cells were used as analogous to the ones designed by Nikolowski et al. [**Nikolowski 2005**]. The modification was in the design of the current collectors. A hollow stainless steel current collector was used on the anode side, which was sealed with epoxy-resin glue (UHU Endfest 300) with a thickness of about 1 – 2 mm. On the cathode side an aluminum current collector was used which was manufactured by gluing a thick aluminum foil on a Teflon tube. This set up as shown in Figure 6.1 b is hermetic and reduces the absorbance of the X-ray beam.

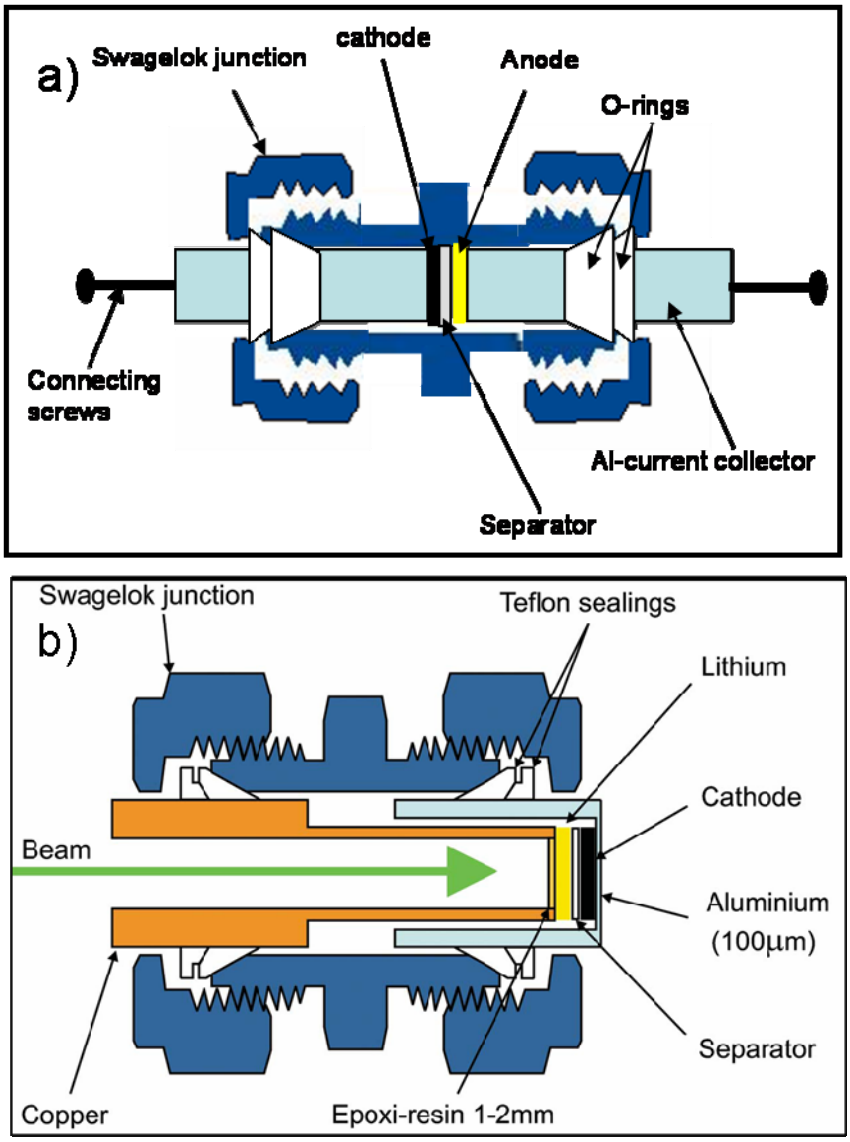

Figure 6.1: *Schematic diagram of the electrochemical cells used for (a) normal measurements and (b) in situ measurements (reproduced with permission from* ***[Nikolowski 2005]****).*

6.2 Galvanostatic measurements

In the galvanostatic measurements, a constant-current pulse is applied between the working and counter electrodes and the variation of potential with time are measured between given potential limits. This method is also known as chronopotentiometry. An applied positive current oxidizes the working electrode and a negative current reduces it. The voltage responses to the applied constant current indicate the changes

in the electrode processes. An example of a galvanostatic measurement is shown in Figure 6.2. An advantage of this method is that, due to the constant current density, the electrode processes are investigated under real working conditions, like in a battery. In the case of new electrode materials whose electrochemical activity potential regions are unknown, a cyclic voltammetry or PITT experiment is performed first using a wide voltage range and the obtained ranges are then used for the galvanostatic cycling. For an intercalation/deintercalation process where A is the guest species, the amount of A according to (equation 6.1) can be calculated as shown by (equation 6.2) [**Hardwick 2007**].

$$A_x \cdot Host + \Delta x \cdot A^+ + \Delta x \cdot e^- \leftrightarrow A_{x+\Delta x} \cdot Host \qquad 6.1$$

$$\Delta x = \frac{I \cdot \Delta t \cdot M_r}{n \cdot F \cdot M} \qquad 6.2$$

I: current Δt: time interval

M_r: Host molecular weight M: mass of the active compound

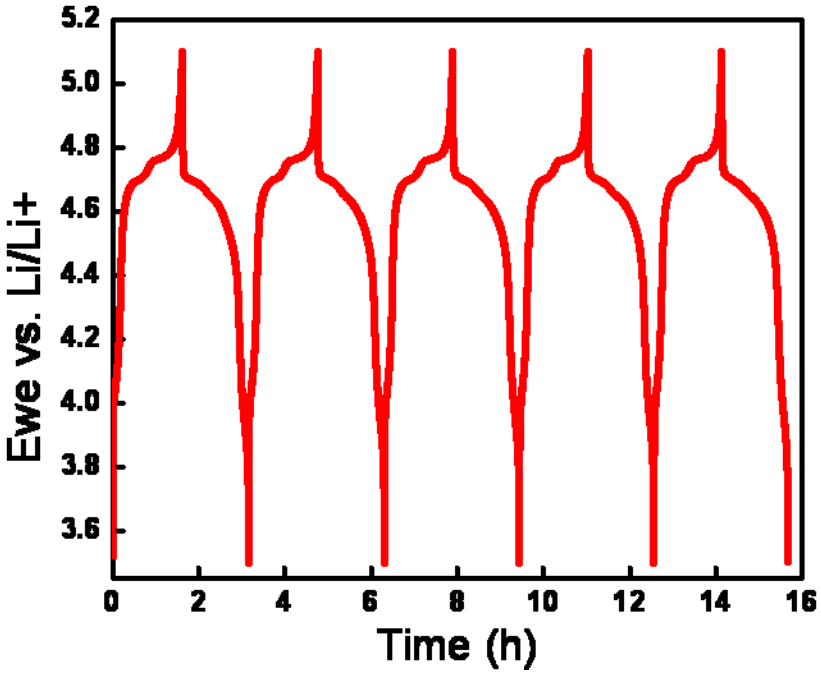

Figure 6.2: *Example of a galvanostatic measurement, performed with a C-rate of C/2. The electrode materials were $LiNi_{0.5}Mn_{1.5}O_4$-1000 (cathode), Li metal (anode) and the electrolyte was 1M $LiPF_6$ in EC:DMC, 1:2.*

6.3 PITT measurements and differential capacity plots

In a PITT experiment (potentiostatic intermittent titration technique), the potential is varied with a fixed potential step width, beginning from the starting potential, without any limited time interval. The current and the flown charge are measured meanwhile and the next potential step starts once the current has fallen under a certain, given value. This is the difference compared with cyclic voltammetry, where the potential is changed after a given time interval. As a result, the dQ/dE vs. E (Ewe) plots obtained from PITT experiments looks similar to a cyclic voltammetry curve but appear more structured and could be easily interpreted.

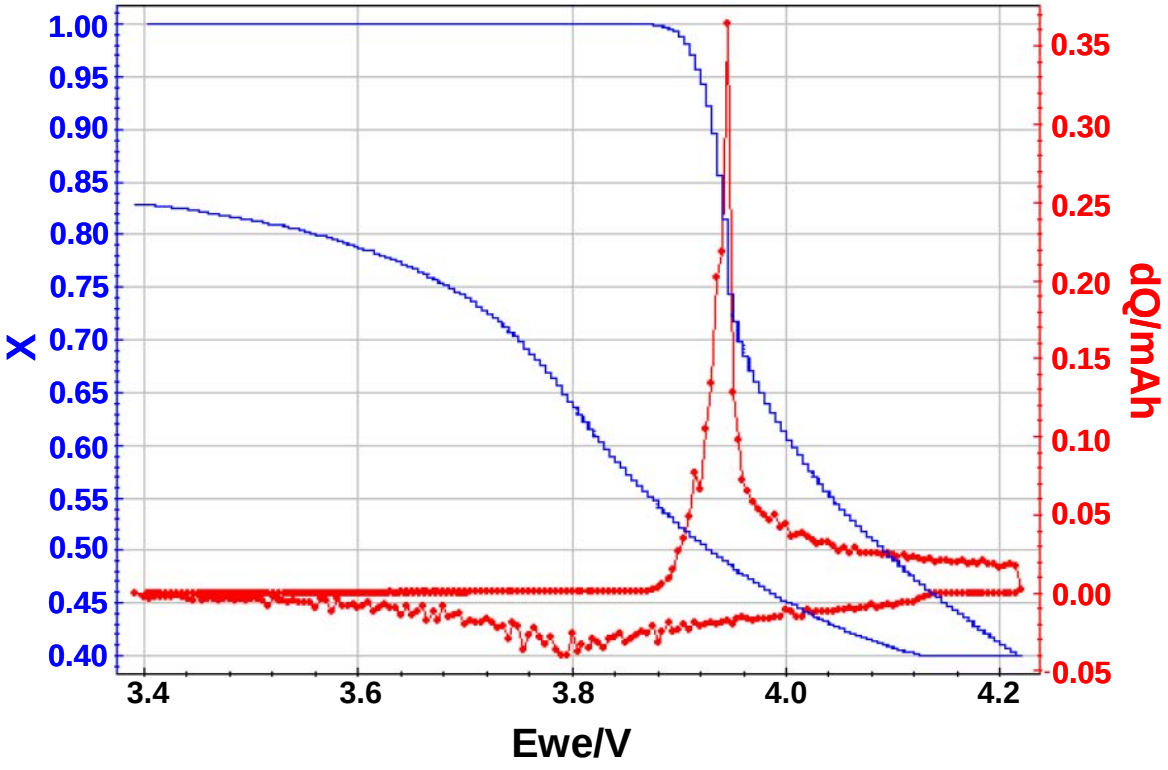

Figure 6.3: *Incremental capacity (dQ vs. Ewe) graph (red circles) and X vs. Ewe plot (blue lines) of a lithium button cell* ***[EC-Lab]****.*

With a VMP potentiostat which uses the EC-Lab software, this technique is called potentiodynamic cycling with galvanostatic acceleration (PCGA). This application corresponds to electrode cycling under stepwise potentiodynamic mode. The potential sweep can be defined by the user by setting the potential step amplitude and duration. It is also possible to go to the next potential step before the end of the duration which

has been set if the charge or discharge currents are lower than a given value (cut-off current limit), that is to cycle at least with a minimum galvanostatic rate. This is a direct protocol to determine the incremental capacities, -dx/dV, of insertion electrode materials while using the compacting function (dQ = f(Ewe)). The quality of the determination is usually better than that obtained by derivation of a titration curve made with chronopotentiometry under galvanostatic mode (because of the significant noise on the potential derivative with respect to the charge, i.e. time) **[EC-Lab]**.

The peak-shape of the incremental capacity plots (the half-width of the peaks) provides information about the mechanism of lithium insertion and extraction in a material. Narrow-sized peaks when appearing at constant potentials, independent of the C-rates is an indication of a mechanism including phase transitions. When the peak shape and appearing potential changes with different C-rates, it may be due to a kinetic effect. The broad peaks can be usually attributed to a solid-solution mechanism of lithium extraction and insertion **[Levi 1999, Wohlfahrt-Mehrens 1997]**.

6.4 Electrode preparation

6.4.1 The working electrode

The working electrode used was a blend of the synthesized $LiM_{0.5}Mn_{1.5}O_4$ (M = Fe, Co, Ni) active material with a conductive additive and a binder. Carbon black was used as the only conductive additive in most cases, which is found to enhance the electronic conductivity, as the conductivity of the spinel itself is not high enough. The binder is added for the purpose of keeping the active material and the conductive additive together. The materials used are listed in Table 6.1. The preparation of the electrode was done in several ways based on the context of application, as described below and in common after the mechanical preparation; the cathodes were dried under vacuum with the help of a glass oven (Büchi B-585) which could be later on transferred into an argon-box so that any contact with atmospheric moisture is avoided.

Table 6.1: *The materials used for electrode preparation.*

Material/solvent	Supplied by	Application
Super P Li carbon	TIMCAL	Conductive additive
Solef PVDF, Poly (vinyledene fluoride), 6020	Solvay Solexis	Binder
SFG 6L graphite	TIMCAL	Conductive additive
N-Methylpyrrolidone (NMP)	Fluka	Slurry preparation
Acetone		Homogenization

- **Using aluminum grid as current collector**

For most of the experiments, including XPS analysis after cycling, the cathode preparation was done using an aluminum mesh as a current collector. For this, first a sheet of aluminum with grids was cut into circular slices of diameter ~12 mm. The cut pieces were then washed with acetone and dried for 10 minutes at 110°C. The mesh was then weighed and placed inside a press matrix. The cathode mixture was prepared by grinding active material, super P Li carbon and PVDF 6020 in a ratio of 80:15:5 respectively with acetone in a mortar for 5 - 7 minutes until a visual mechanical homogenization was achieved. A part of the obtained mixture was then deposited uniformly on the aluminum mesh which is already inside the press matrix and pressed at 5 tons. The surface of the mesh was then scratched with a spatula so that the material is deposited only inside the grids. The obtained cathode was then dried at 120°C for 1 h in the vacuum oven. The dried cathode was then weighed inside the argon-box and used for the electrochemical studies.

- **Pellet cathode**

To conduct *in situ* and most of the *ex situ* XRD measurements, and for metal dissolution and thermal stability experiments, cathode pellets were prepared as follows: the active material, super P Li carbon and PVDF 6020 were mixed in a ratio of 80: 10: 10 respectively with NMP in a mortar. The obtained slurry was then dried for approximately 12 h at 110°C and pressed into a pellet with a pressure of 8 tons. The pressed pellet was then dried at 120°C for 24 h in a vacuum oven and weighed in the argon-box before use.

- **Using aluminum foil as current collector**

For commercial applications of the synthesized materials, it is necessary to coat them uniformly on aluminum foils. Hence it was also important to optimize the preparation of these aluminum foil cathodes. In order to achieve this, different ratios of active material and additives were tried and sometimes the type of additives was also varied. The active material was always selected as $LiNi_{0.5}Mn_{1.5}O_4$ (1000°C annealed), due to its known superior electrochemical behavior. A list of additives used and their amounts in different experiments are shown in Table 6.2. The aluminum foils for the given experiments were supplied by Evonik and were of thickness 0.02 mm and the coating was performed using a Model 509 MC I (ERICHSEN) coating machine.

In experiment I, the active material and super P Li carbon were first dissolved in NMP by stirring for 2 h and PVDF was added followed by a stirring of 3 h. The homogeneous slurry obtained was then coated on the aluminum foil and dried at 60°C overnight.

In experiment II, the active material and super P Li carbon were mixed well by grinding and the powder mixture was then heated at 60°C for 1 h. PVDF, previously dissolved in NMP, was added to the above mixture and stirred for 2 h. The homogeneous slurry obtained was then coated on the aluminum foil and dried at 60°C for 2 h, followed by overnight drying at 80°C.

Experiment III was done different from I and II. In addition to the active material and above additives, graphite was also used for the cathode preparation. The active material, super P Li carbon and graphite were mixed well by grinding with acetone and dried at 110°C for 1 h. A previously made solution of PVDF in DMF was added to the above mixture and mixed well with an IKA T25 digital ULTRA-TURRAX for 1 h. The obtained slurry was then subjected to a very slow evacuation, in order to remove the air bubbles and this was achieved by placing the small beaker containing the slurry inside a desiccator and applying vacuum to the desiccator. After coating the obtained slurry, the aluminum foil was dried overnight at 60°C.

Table 6.2: *The weight ratios of additives used and wet thickness of coating in aluminum foil cathode optimization.*

Electrode components	Active material (w/w %)	Super P Li Carbon (w/w %)	PVDF binder (w/w %)	Graphite(w/w %)	Wet coating thickness on Al foil (μm)
Experiment-I	80	10	10		90
Experiment-II	84	8	8		250
Experiment-III	85	5	5	5	80

All the coated foils from the mentioned three experiments were cut into circular cathodes of diameter 12 mm and each cathode was then pressed at 8 tons. The pressed cathodes were then dried at 120°C under vacuum for 24 h. The weight of cathode mixture on the foil was calculated by weighing at least 30 pieces of the cut cathodes and non-coated aluminum foils, cut with the same diameter, and taking the difference of the average weights. The differences in the electrochemical performances of these cathodes prepared by different experiments will be discussed in chapter 8 together with other electrochemical results.

6.4.2 The counter electrode

The counter electrode is the one which finally complete the cell circuit. In the work presented here, metallic lithium (high purity lithium foil, 0.50 mm thick, supplied by Chemetall Corporation) was used as the counter electrode. A circular piece of lithium with about 7 mm diameter was cut out from the ribbon and placed in front of the working electrode at a distance given by the separator.

6.4.3 The reference electrode

A reference electrode is used to measure the potential of the working electrode. The reference electrode should have a constant potential in the absence of a current flow. In order to reduce the ohmic potential drop due to the presence of electrolyte solution between it, the reference electrode should be similar to the working electrode. In the work reported here, the counter electrode, which was metallic lithium, was always used as the reference mainly due to the advantage of very high exchange current in

contact with the electrolyte solution (containing 1M concentration of the lithium salt, hence Li^+).

6.4.4 The electrolyte

The electrolyte used for this work was 1 M $LiPF_6$; in EC: DMC (1:2) (POWERLYTE, UBE). The electrolyte was used for the measurements as received. The water content of the electrolyte was analyzed as <20 ppm by Karl-Fischer titration.

6.4.5 The separator

Separators act as a medium of ionic transport and also serve the purpose of dividing the working and counter electrodes. A glass fiber paper, supplied by MACHEREY NAGEL was used for this partition. The paper was cut into circular pieces of diameter 13 mm and dried under vacuum at 110°C for 24 h before application. Always two pieces were used as a precaution for short-circuit in the cells.

6.5 Instrumentation

The electrochemical tests were performed with a computer controlled multichannel potentiostatic–galvanostatic system, VMP (Perkin Elmer Instruments, USA), using the prepared two electrode cells. A schematic drawing of this configuration is shown in Figure 6.4, where WE, CE and RE refer respectively to the working electrode, counter electrode and reference electrode. The electrochemical experiments can be done either by controlling the cell potential (potentiostatic) or the current flow (galvanostatic). These controls as well as the post data analysis were performed with the help of a software EC-Lab **[EC-Lab]**.

For doing high temperature cycling experiments, a thermostat coupled with the potentiostat was used. The cells were connected to the channels inside the thermostat and subjected to an initial relaxation period of 1 h. This relaxation period was applied by using the EC-Lab software and it helped the cell to heat up to the temperature provided (usually 55°C for high temperature cycling experiments).

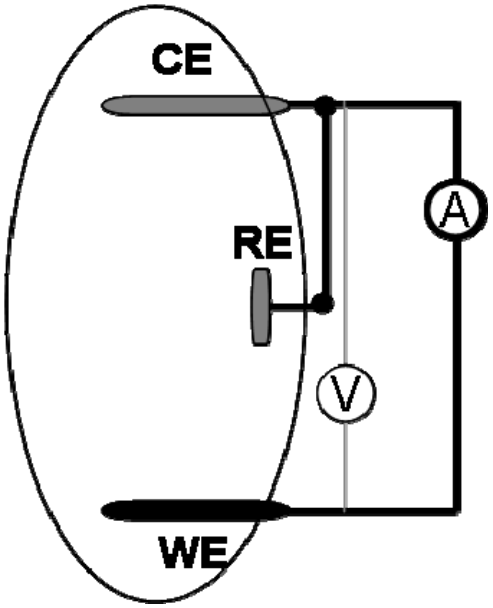

Figure 6.4: *Schematic drawing of a two-electrode setup for the electrochemical cells, redrawn from* ***[Piotto 2004]****.*

6.6 *in situ* synchrotron diffraction

Simultaneous diffraction and electrochemical measurements were taken to understand the phase changes or lattice expansion during electrochemical processes. By applying this *in situ* method, many factors like any unwanted chemical reactions by change in the environment or scattering between data from several samples etc. could be eliminated. The electrochemical tests were performed using a multichannel potentiostatic–galvanostatic system VMP (Perkin Elmer Instruments, USA).

The RT *in situ* synchrotron diffraction during electrochemical cycling was carried out using specially designed cells (shown in Figure 6.1 b) and pellet cathodes at the powder diffraction beamline B2 of the Deutsches Elektronensynchrotron (DESY) at Hamburg, Germany. The prepared cell was then mounted on a flat sample holder, as shown in Figure 6.5, which could be oscillated to reduce preferred orientation effects and enhance powder statistics.

The cells were subjected to galvanostatic cycling at RT with a charge-discharge rate of C/8. The voltage range 3.0 - 5.5 V was chosen to ensure the maximum degrees of charge/discharge and, consequently, the maximum degrees of lithium

extraction/insertion, respectively. The data recording for the XRD measurements was started simultaneously with cell charging and was continuously performed with a time interval of 10 minutes until the completion of the first cycle.

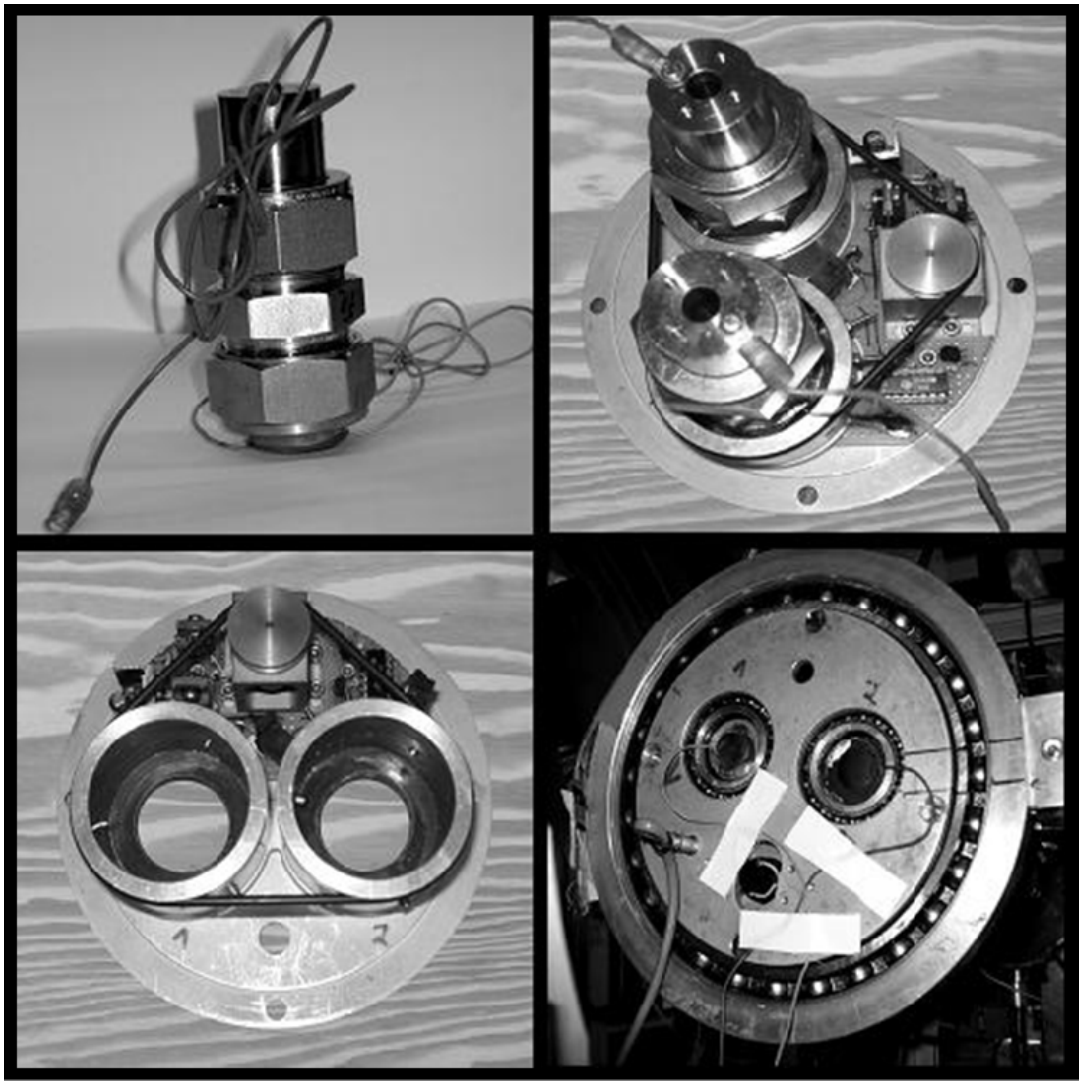

Figure 6.5: *Images of the the electrochemical cell (top left) and the flat sample holder from different directions (top right and bottom), used for in situ studies.*

The diffraction data was recorded using an on-site readable image-plate detector OBI [**Knapp 2004b**]. The XRD measurements were conducted with a wavelength of λ = 0.65168(1) Å, selected by a double-crystal Si (111) monochromator. Rietveld refinement was applied for data analysis using the WinplotR package [**Roisnel 2001**].

The standard deviations of all refined parameters were calculated in agreement with Berar and Lelann [**Berar 1991**].

Chapter 7
Characterization of Li$M_{0.5}Mn_{1.5}O_4$ (M = Fe, Co, Ni)

This chapter is mainly focused on the characterization of the transition metal-doped, Mn-based 5 V spinels. A detailed structural investigation was performed using X-ray diffraction (XRD) and neutron diffraction techniques. The morphology of the synthesized materials was analyzed using scanning electron microscopy (SEM). Analysis of the composition was done using inductively coupled plasma–optical emission spectroscopy (ICP-OES). The thermal properties were studied using simultaneous thermogravimetry (TG)-differential thermal analysis (DTA) studies.

7.1 Structural Characterization

7.1.1 X-ray powder diffraction

To obtain the spinel $LiNi_{0.5}Mn_{1.5}O_4$ the calcination of the precursor was performed initially at 600°C for 12 hours. The X-ray diffraction pattern of this sample reveals the existence of two sets of peaks which could be indexed based on the $Fd\bar{3}m$ space group, corresponding to the cubic spinel structures with two different lattice constants, 8.1773(2) Å (92% w/w) and 8.2356(7) Å (8% w/w), see Figure 7.1. The second set of reflections were disappeared when the sample was ground and reannealed at 600°C again for 12 h, Figure 7.2 f. As the holding time 12 h seems to be not sufficient to obtain phase-pure spinel at this temperature, 24 h holding time was applied for the synthesis of final products Li$M_{0.5}Mn_{1.5}O_4$-600 (M = Fe, Co, Ni) with intermittent grinding after 12 h.

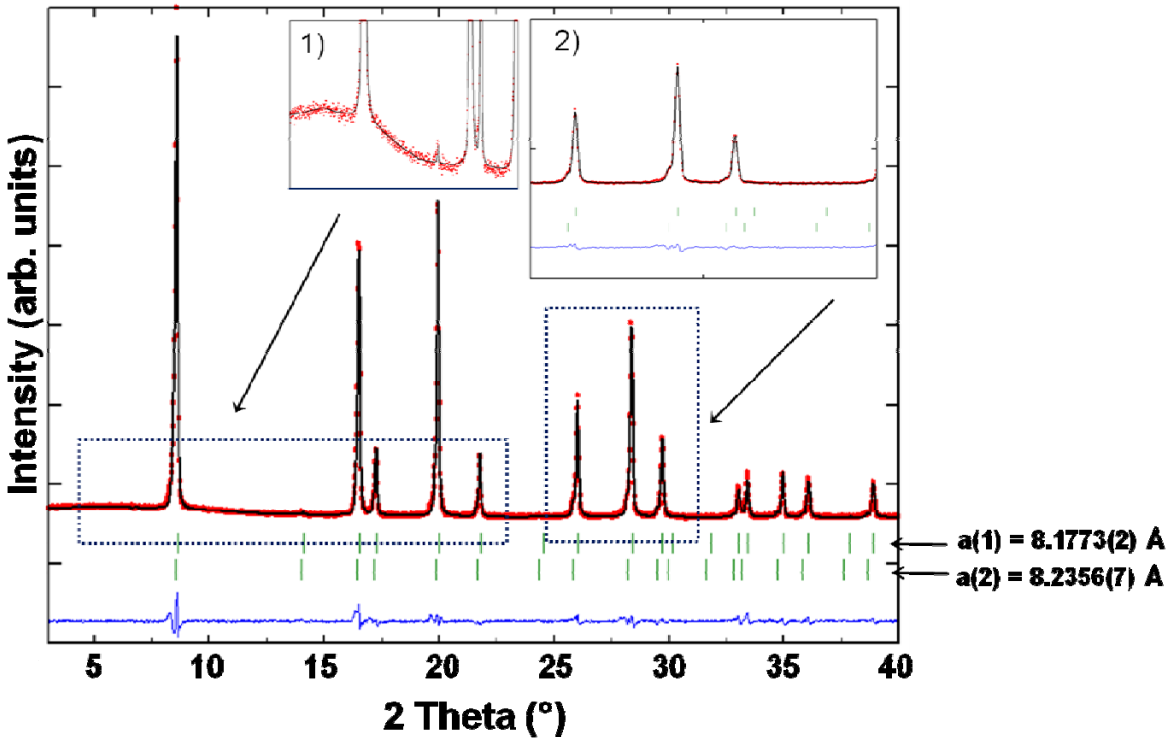

Figure 7.1: *Rietveld refinement for $LiNi_{0.5}Mn_{1.5}O_4$ obtained by Pechini synthesis (a) based on $Fd\bar{3}m$ space group, after annealing at 600°C for 12 h. Inset: (1) large amorphous part; (2) shows the existence of the second set of reflections as a shoulder on the left side of the higher angle reflections.*

Figure 7.2 shows the results of simultaneous refinements based on the XRD and neutron diffraction data obtained for $LiM_{0.5}Mn_{1.5}O_4$-600 (M = Fe, Co, Ni). In all the diffraction patterns shown in this work, the observed data are shown as points (in red), calculated profile as drawn line (in black) and the corresponding difference curve (in blue) at the bottom of each figure. The lines of vertical marks (in green) indicate the calculated positions of reflections. Rietveld analysis based on both X-ray and neutron data for $LiNi_{0.5}Mn_{1.5}O_4$-600 shows that this sample crystallizes with a partial ordering of Ni and Mn on distinct sites, corresponding to the primitive cubic space group $P4_332$. In addition, a small amount of impurity phase identified as $Li_xNi_{1-x}O$ (~1% w/w) with a rock-salt structure was observed. The structural parameters are summarized in Table 7.1.

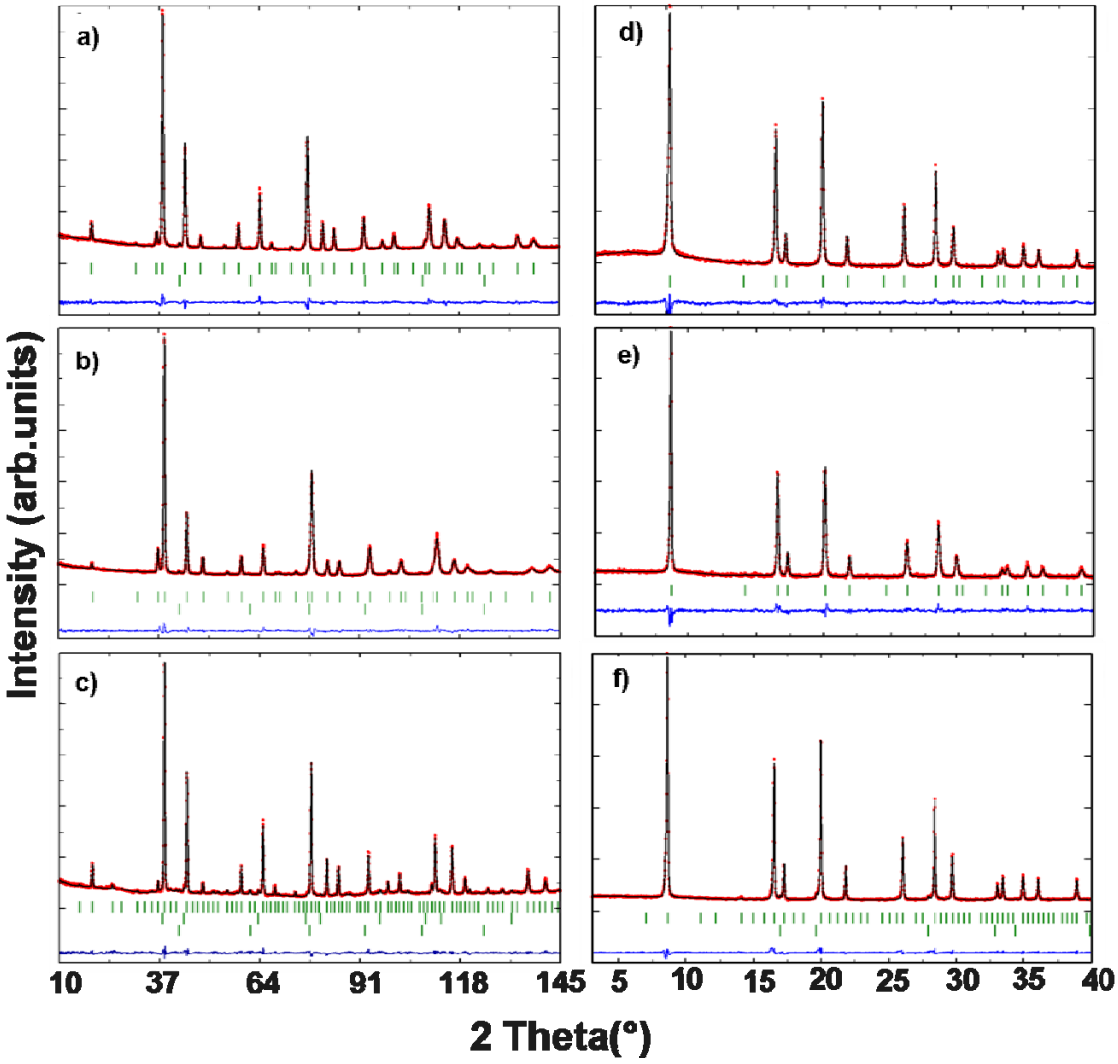

Figure 7.2: *Left: Neutron diffraction patterns at RT for 600°C annealed (a) $LiFe_{0.5}Mn_{1.5}O_4$ in $Fd\bar{3}m$ space group (b) $LiCo_{0.5}Mn_{1.5}O_4$ in $Fd\bar{3}m$ space group (c) $LiNi_{0.5}Mn_{1.5}O_4$ in $P4_332$ space group (top line of reflection marks), with about 1% w/w contribution from $Li_xNi_{1-x}O$ (middle line of reflection marks). The bottom line of reflections marks the positions of extreme weak but visible reflections from the V-container. Right: XRD patterns at RT for 600°C annealed (d) $LiFe_{0.5}Mn_{1.5}O_4$ in $Fd\bar{3}m$ space group (e) $LiCo_{0.5}Mn_{1.5}O_4$ in $Fd\bar{3}m$ space group (f) $LiNi_{0.5}Mn_{1.5}O_4$ in $P4_332$ space group[2] (top line of reflection marks) with about 1% w/w contribution from $Li_xNi_{1-x}O$ (bottom line of reflection marks).*

[2] Note that Figure 7.2 shows the results of a simultaneous refinement of XRD and neutron diffraction data. This is the reason why the patterns in 7.2 f are assigned to $P4_332$ space group even though this difference cannot be seen with XRD.

The Ni-Mn order is not complete, and the stoichiometry $LiNi_{0.46(2)}Mn_{1.54(2)}O_4$ is calculated from the refined site occupation factors (s.o.f). The slight Ni-deficiency is in very good agreement with the small observed fraction of $Li_xNi_{1-x}O$ (~1% w/w) in XRD and the calculated stoichiometry agrees with the overall composition obtained from ICP-OES (see Table 7.3, section 7.3).

The so-called "ordered" spinel $LiNi_{0.5}Mn_{1.5}O_4$ ($P4_332$ space group) has been always considered as a completely ordered structure with Ni exclusively on the 4a site and Mn exclusively on the 12d site [**Kim 2004a]**. The appearance of the cation disorder has been attributed to the transformation of completely ordered primitive spinel ($P4_332$) to the fully disordered F-centered spinel ($Fd\bar{3}m$). Here it is shown for the first time that the small degree of 3d-cation disorder in $P4_332$ structure is possible. This one-phase structure model with partial order clearly gave a better agreement with the observed diffraction data than a two-phase model, based on the co-existence of completely ordered and completely disordered spinels. Therefore, the specific Ni/Mn distribution on the 4a and 12d sites is an important structural degree of freedom for this material, and neutron diffraction is essential for a complete characterization.

In the case of $LiCo_{0.5}Mn_{1.5}O_4$-600 and $LiFe_{0.5}Mn_{1.5}O_4$-600, neutron diffraction reveals only the existence of $Fd\bar{3}m$ spinels with statistical distributions of the 3d-cations. Rietveld refinement converges with site occupation factors, corresponding to stoichiometries of $LiFe_{0.44}Mn_{1.56}O_4$ and $LiCo_{0.48}Mn_{1.52}O_4$. The structural parameters for all three samples are given in Table 7.1 and 7.2.

For the $LiM_{0.5}Mn_{1.5}O_4$-1000 (M = Fe, Co, Ni) samples, the X-ray analysis revealed an increase in the cell parameters in comparison with those of $LiM_{0.5}Mn_{1.5}O_4$-600 (M = Fe, Co, Ni) samples, which may indicate an oxygen loss from the spinel structure (see Table 7.2). High temperature calcinations lead to an oxygen deficiency in manganese-based spinels, which is accompanied by the increasing amount of Mn^{3+} and, consequently, by the increase of the cell volume [**Zhong 1997, Pasero 2008, Caballero 2005, Wang 2003**].

***Table 7.1**: Structural parameters obtained from simultaneous Rietveld refinements based on XRD and neutron diffraction data, for $LiM_{0.5}Mn_{1.5}O_4$-600 (M = Fe, Co, Ni) samples.*

(a) Structural parameters obtained from Rietveld refinement for $LiFe_{0.5}Mn_{1.5}O_4$ based on space group $Fd\bar{3}m$				
Atom	Wyckoff site	x = y = z	$u_{iso}/Å^2$	s.o.f.
Li	8a	1/8	1.83(10)	1
Fe/ Mn	16d	½	0.56(5)	0.22(1)/ 0.78(1)
O	32e	0.2629(1)	1.02(2)	1

(b) Structural parameters obtained from Rietveld refinement for $LiCo_{0.5}Mn_{1.5}O_4$ based on space group $Fd\bar{3}m$				
Atom	Wyckoff site	x = y = z	$u_{iso}/Å^2$	s.o.f.
Li	8a	1/8	1.16(9)	1
Co/ Mn	16d	½	0.48(4)	0.24(1)/ 0.76(1)
O	32e	0.2631(1)	0.80(2)	1

(c) Structural parameters obtained from Rietveld refinement for $LiNi_{0.5}Mn_{1.5}O_4$ (space group $P4_332$). Note that the thermal displacement parameters for the two 3d-tranisition metal sites and for the two oxygen sites, respectively, were constrained						
Atom	Wyckoff site	x	y	z	$u_{iso}/Å^2$	s.o.f.
Li	8c	0.004(7)	0.004(7)	0.004(7)	0.8(4)	1
Ni1/ Mn1	4a	5/8	5/8	5/8	0.1(1)	0.43(2)/0.57(2)
Ni2/ Mn2	12d	1/8	0.378(1)	-0.128(1)	0.1(1)	0.16(1)/0.84(1)
O1	8c	0.387(1)	0.387(1)	0.387(1)	0.49(3)	1
O2	24e	0.141(1)	-0.139(1)	0.135(1)	0.49(3)	1

(d) Refinement results for $LiM_{0.5}Mn_{1.5}O_4$-600 (M = Fe, Co) (space group $Fd\bar{3}m$) and $LiNi_{0.5}Mn_{1.5}O_4$-600 (space group $P4_332$)			
Sample	Space Group	a (Å)	Vol (Å^3)
$LiFe_{0.5}Mn_{1.5}O_4$	$Fd\bar{3}m$	8.2190(6)	555.22(7)
$LiCo_{0.5}Mn_{1.5}O_4$	$Fd\bar{3}m$	8.1321(6)	537.7(1)
$LiNi_{0.5}Mn_{1.5}O_4$	$P4_332$	8.17392(7)	546.12(1)

For Co- and Fe-doped samples, no additional phase was observed after the high temperature treatment. For Ni-doped sample, the amount of $Li_xNi_{1-x}O$ (<4% w/w) impurity phase increased slightly comparing to $LiNi_{0.5}Mn_{1.5}O_4$-600 (see Figure 7.3). The formation of these admixtures has been often reported for the high-temperature synthesis of $LiNi_{0.5}Mn_{1.5}O_4$ and may be considered as additional evidence for the oxygen non-stoichiometry in the spinel structure [**Zhong 1997**]. The appearance of this admixture with Ni^{2+} reduces the effect of increasing lattice parameter of the spinel phase, see column 4 in Table 7.2.

Table 7.2: *The cubic lattice parameters "a" for $LiM_{0.5}Mn_{1.5}O_4$-600 and $LiM_{0.5}Mn_{1.5}O_4$-1000 (M = Fe, Co, Ni).*

M in $LiM_{0.5}Mn_{1.5}O_4$	a/ Å (for 600°C)	a/ Å (for 1000°C)	Δa/ a
Fe	8.2190(6)	8.2575(2)	0.47%
Co	8.1321(6)	8.1660(2)	0.42%
Ni	8.17392(7)	8.1946(2)	0.25%

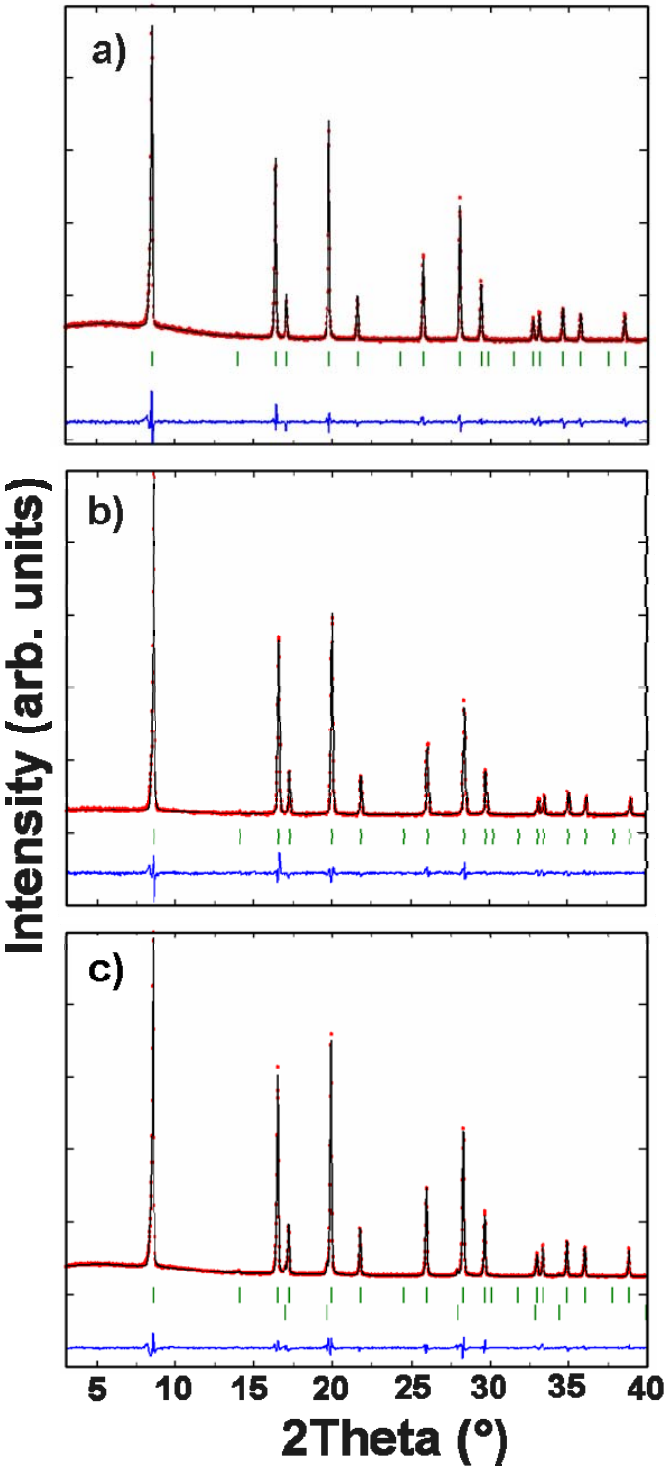

Figure 7.3: *XRD patterns at RT, after additional fast excursion to 1000°C. In* $Fd\bar{3}m$ *space group (a)* $LiFe_{0.5}Mn_{1.5}O_4$*, (b)* $LiCo_{0.5}Mn_{1.5}O_4$*, (c)* $LiNi_{0.5}Mn_{1.5}O_4$ *where the top line of reflection marks shows* $LiNi_{0.5}Mn_{1.5}O_4$ *with 96(1)% w/w and the bottom line of marks shows the contribution from* $Li_xNi_{1-x}O$ *with 4(1)% w/w.*

7.2 Morphology studies

The images were taken in secondary electron mode with an acceleration voltage of 20 kV and with varied spot sizes.

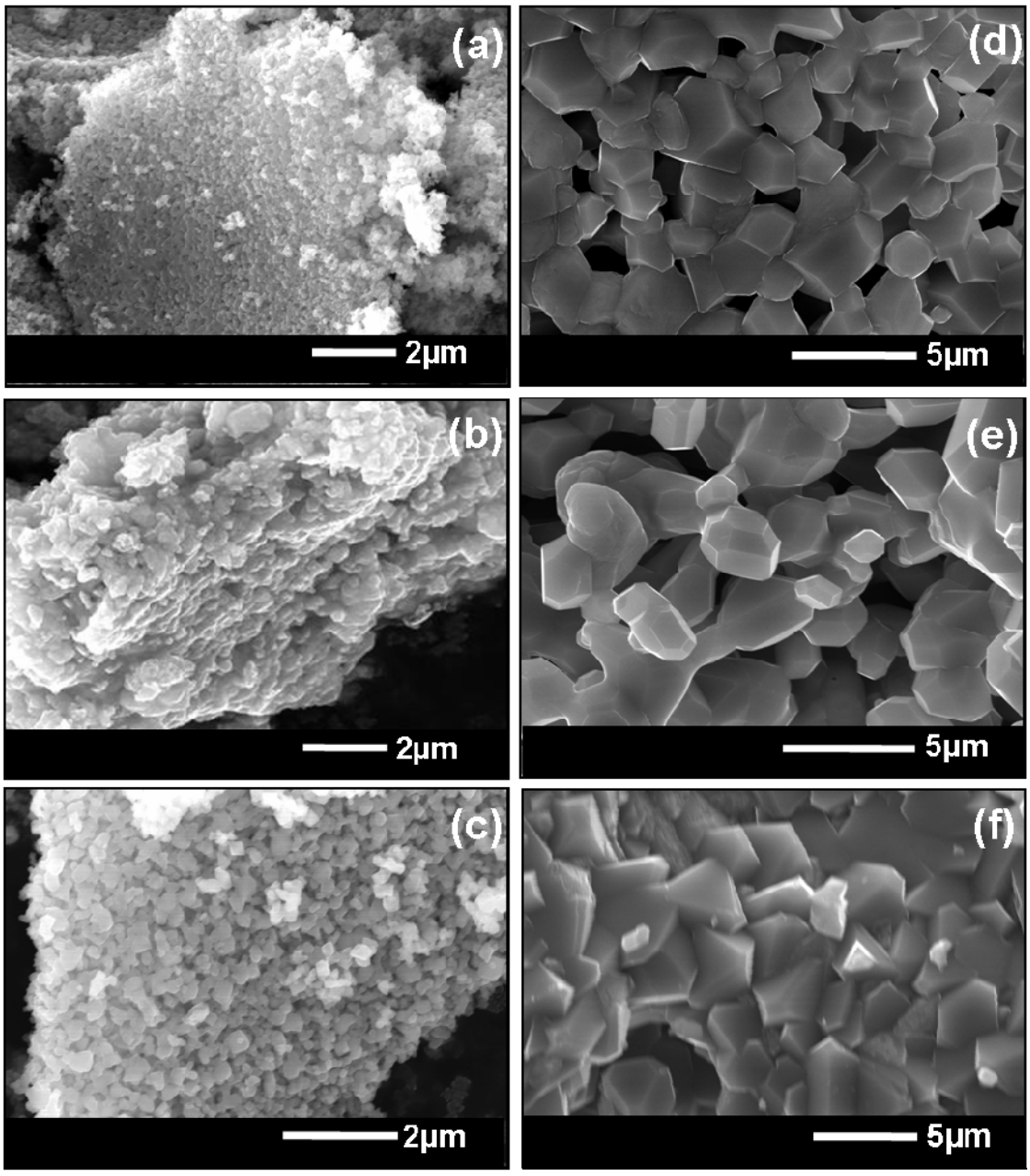

***Figure 7.4**: SEM images of (a) $LiFe_{0.5}Mn_{1.5}O_4$-600, (b) $LiCo_{0.5}Mn_{1.5}O_4$-600, (c) $LiNi_{0.5}Mn_{1.5}O_4$-600, (d) $LiFe_{0.5}Mn_{1.5}O_4$-1000, (e) $LiCo_{0.5}Mn_{1.5}O_4$-1000 and (f) $LiNi_{0.5}Mn_{1.5}O_4$-1000. Different scales are shown for the 600°C and 1000°C annealed particles as the former exhibited comparatively smaller particle size.*

The SEM images obtained show that the samples annealed at 600°C for 24 h are not well crystallized whereas a fast excursion to 1000°C results in good crystallinity as revealed by their pseudo-octahedral forms and smoother particle surface (see Figure 7.4). This relatively short heat treatment resulted also in a significant growth of the particles from 200 - 400 nm to 2 - 4 µm.

7.3 Chemical analysis

The chemical composition of the material was analyzed by ICP-OES and the obtained results are shown in Table 7.3.

Table 7.3: *The results of ICP-OES analysis of $LiM_xMn_yO_4$-600 (M = Fe, Co, Ni) and $LiM_xMn_yO_4$-1000 (M = Fe, Co, Ni).*

$LiM_xMn_yO_4$-600 (*M* = Fe, Co, Ni)					
Samples	Li	Mn (y)	Fe (x)	Co (x)	Ni (x)
$LiFe_xMn_yO_4$-600	1.00 (2)	1.51 (9)	0.47 (3)		
$LiCo_xMn_yO_4$-600	1.00 (1)	1.50 (1)		0.51 (4)	
$LiNi_xMn_yO_4$-600	1.00 (2)	1.50 (3)			0.50 (1)

$LiM_xMn_yO_4$-1000 (*M* = Fe, Co, Ni)					
Samples	Li	Mn (y)	Fe (x)	Co (x)	Ni (x)
$LiFe_xMn_yO_4$-1000	0.998 (7)	1.529 (9)	0.471 (3)		
$LiCo_xMn_yO_4$-1000	0.996 (9)	1.49 (1)		0.504 (4)	
$LiNi_xMn_yO_4$-1000	0.989 (9)	1.504 (9)			0.496 (3)

The stoichiometries from the ICP-OES analysis are calculated assuming a complete oxygen stoichiometry in the compound. The obtained results show that the stoichiometries of the samples calculated from the ICP-OES analysis are in good

agreement with the refined stoichiometries, especially with the slight Mn excess in the Fe compound. The slightly lower amount of lithium in the Li$M_xMn_yO_4$-1000 (M = Fe, Co, Ni) samples can be attributed to the assumed complete stoichiometry of the oxygen, which is actually less in the real case after fast excursion to 1000°C, as revealed by an increase in the lattice parameter.

7.4 Thermogravimetric analysis

Oxygen non-stoichiometry is a factor which needs to be taken into account before applying a synthesized material in lithium-ion batteries, as it is found to be directly related to cation-ordering and electrochemical activity regions, especially in the case of spinels and layered rock-salt structures [**Pasero 2008**]. Pasero et al. have also investigated on the reversibility of oxygen exchange and estimated the oxygen deficiency (δ) in $LiNi_{0.5}Mn_{1.5}O_{4-\delta}$ using TG measurements. A similar approach has been made to investigate the oxygen stoichiometry studies in Li$M_{0.5}Mn_{1.5}O_4$-600 and Li$M_{0.5}Mn_{1.5}O_4$-1000 (M = Fe, Co, Ni) samples. In order to perform this, simultaneous TG-DTA analyses were conducted, on known weights of samples in synthetic air atmosphere. The samples were heated to 1200°C (up to 1000°C in case of Li$M_{0.5}Mn_{1.5}O_4$-1000 samples) and cooled back to ~350°C, with a heating and cooling rate of 10°C/minute.

The results of the above analyses are shown in Figure 7.5. All the samples were assigned an initial weight of 100%. Above ~650°C, all the 600°C annealed samples were found to have an onset of weight loss. At 1200°C, the weight loss is found to be ~6.7% in the case of Fe and Ni containing samples and ~5.2% in the case of Co containing sample respectively. The cooling curves in the case of all the three 600°C synthesized samples were of similar behavior which showed a reversible weight gain between 1200 and 650°C. This reversibility indicates that oxygen gain or loss is completely responsible for the weight changes under the given conditions. This is further supported by the appearance of endothermic and exothermic signals on heating and cooling between 800 and 1200°C for all the samples, irrespective of the dopant ion.

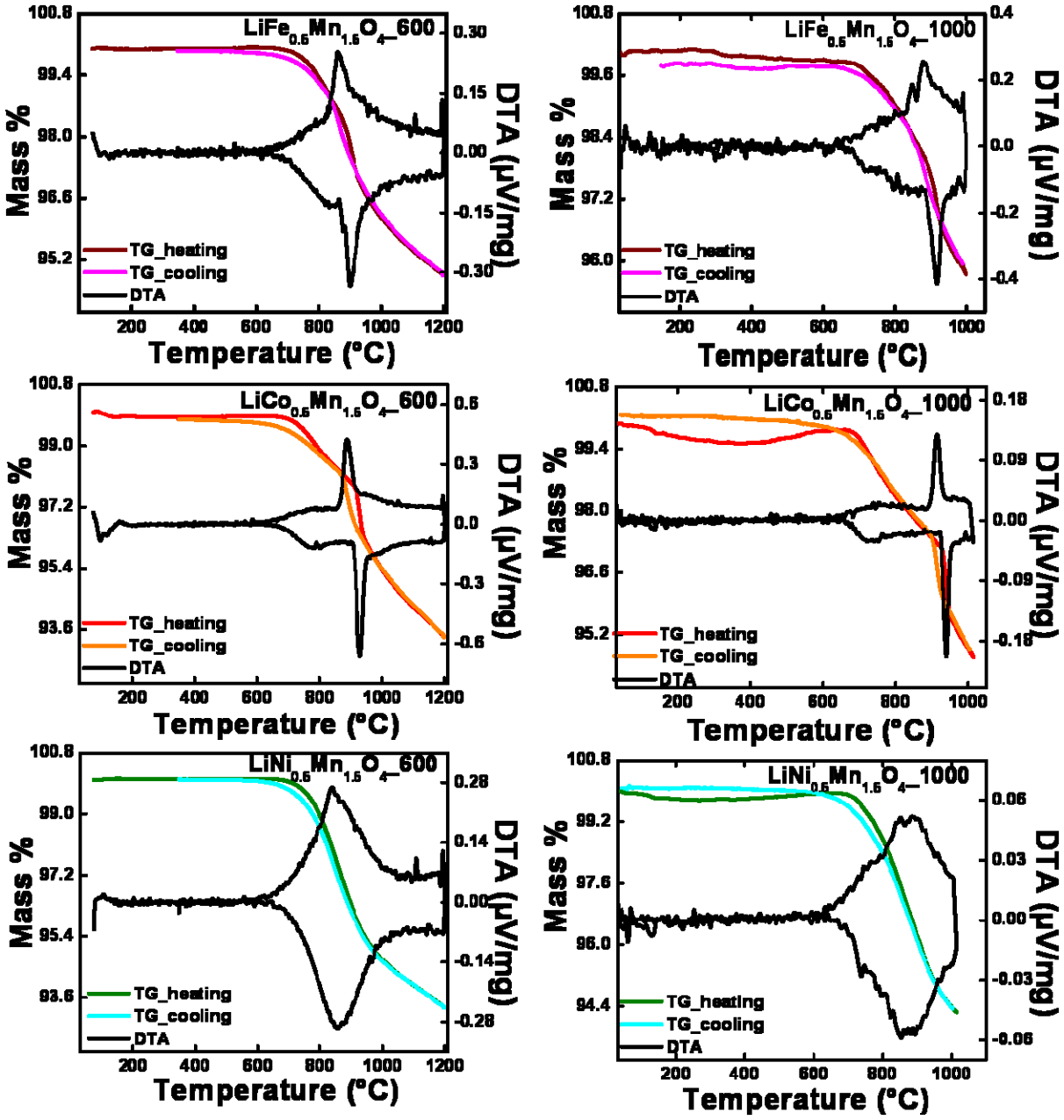

Figure 7.5: *TG profile (colored lines) and DTA curves (black lines) in synthetic air at a rate of 10°C/ minute, for $LiM_{0.5}Mn_{1.5}O4$-600 (M = Fe, Co, Ni) and $LiM_{0.5}Mn_{1.5}O4$-1000 (M = Fe, Co, Ni) samples.*

The heating curves of $LiM_{0.5}Mn_{1.5}O_4$-1000 (M = Fe, Co, Ni) samples show slightly different behavior in comparison with the 600°C samples. There is a small weight gain during heating close to 650°C, considerably less pronounced in the case of $LiFe_{0.5}Mn_{1.5}O_4$-1000 which is an indication of the oxygen deficiency in these high temperature treated materials [**Pasero 2008**]. However, this oxygen deficiency is

considerably less in the case of all Li$M_{0.5}Mn_{1.5}O_4$-1000 (M = Fe, Co, Ni) samples, as revealed by the less pronounced weight gain close to 650°C. The remaining features in the heating and cooling profiles of the Li$M_{0.5}Mn_{1.5}O_4$-1000 (M = Fe, Co, Ni) samples are similar to that described in the case of 600°C annealed samples.

Chapter 8
Electrochemical studies

The electrochemical measurements on Li$M_{0.5}$Mn$_{1.5}$O$_4$ (M = Fe, Co, Ni) were carried out to compare electrochemical performance of these materials in terms of electrochemical activity regions, cycling stability and rate capability. Two most common electrochemical techniques for the characterization of battery materials were applied: potentiostatic intermittent titration technique (PITT) and galvanostatic cycling. The materials were also characterized by crystal structure analysis (X-ray, synchrotron and neutron diffraction) and morphological analysis (SEM). The surface properties of the materials before and after cycling were studied by XPS.

8.1 Differential capacity plots

Differential capacity plots were obtained by potentiostatic intermittent titration technique. In most of the measurements, a cut-off current limit C/5 was applied (if not otherwise stated). The PITT experiments were done in the first charge-discharge cycle followed by after 50th and 100th cycles in the case of each sample, with intermittent galvanostatic cycling.

The incremental capacity plots obtained for the Li$M_{0.5}$Mn$_{1.5}$O$_4$-600 and Li$M_{0.5}$Mn$_{1.5}$O$_4$-1000 (M = Fe, Co, Ni) samples are displayed in Figure 8.1. It can be seen that the 600°C annealed Ni-doped sample exhibits two reversible peaks in the voltage range 4.7-4.9 V vs. Li/Li$^+$ during the Li extraction/insertion. According to the previous reports, this couple of peaks reflects Ni^{2+}/Ni^{4+} electrochemical reaction, which takes place via topotactic one-step phase transition between two cubic phases. [**Kim 2004a, Ariyoshi 2004, Arrebola 2006b**]. After the fast excursion to 1000°C, the material was found to exhibit a small electrochemical activity in the 4 V-region, usually attributed to a Mn^{3+}/Mn^{4+} electrochemical reaction. The formation of

electrochemically active Mn^{3+} in the 1000°C annealed Ni-doped sample could be explained as an effect of increased oxygen deficiency in the spinel structure ($LiNi^{(2+)}_{0.5}Mn^{(4+)}_{1.5-\delta}Mn^{(3+)}_{\delta}O_{4-\delta/2}$) at temperatures ≥ 650°C.

Comparing to $LiNi_{0.5}Mn_{1.5}O_4$, the distribution of oxidation states is known for $LiCo_{0.5}Mn_{1.5}O_4$ and $LiFe_{0.5}Mn_{1.5}O_4$ to be different. [**Amine 1996, Kawai 1999**]. The oxidation states of both Fe and Co in $LiM_{0.5}Mn_{1.5}O_4$-600 and $LiM_{0.5}Mn_{1.5}O_4$-1000 (*M* = Fe, Co) were found to be +3, which in turn illustrates the presence of significant amount of Mn^{3+} in these samples, as revealed by the stoichiometry. The Co and Fe-samples prepared at 600°C exhibit two pronounced oxidation-reduction peaks, one in the 4 V region (Mn^{3+}/Mn^{4+} reaction) as well as another peak in the voltage range 4.8-5.3 V (Co^{3+}/Co^{4+} and Fe^{3+}/Fe^{4+}), see Figure 8.1. In general, the fast excursion of $LiCo_{0.5}Mn_{1.5}O_4$ and $LiFe_{0.5}Mn_{1.5}O_4$ to 1000°C may have resulted in an oxygen deficiency and as an outcome, an increase in the amount of Mn^{3+} in the structure, in-order to maintain the electrical neutrality. The increase in the lattice parameters after the fast heating up to 1000°C for all the three samples (Table 7.2 in section 7.1), supports this idea. However, this quantitative increase of Mn^{3+} after excursion to 1000°C is very difficult to detect in the PITT plots.

The incremental capacity plots obtained for $LiCo_{0.5}Mn_{1.5}O_4$ and $LiFe_{0.5}Mn_{1.5}O_4$ were highlighted by a peculiar feature; well pronounced shoulders in the oxidation/reduction peaks in the 4 V and 5 V regions designated as A, A' and B, B' respectively as shown in Figure 8.1. Though this feature is observed before, no discussions were available from literature **[Dokko 2004]**. To our knowledge, this feature may indicate the stepwise character of the structural changes, corresponding to the electrochemical reactions Mn^{3+}/Mn^{4+} and Co^{3+}/Co^{4+} (Fe^{3+}/Fe^{4+}), respectively. Another characteristic feature which was observed in the case of $LiFe_{0.5}Mn_{1.5}O_4$-1000 samples is the existence of a sharp peak at about 4.8 V, in the 5 V region of the discharge capacity, in the first cycle. Three independent experiments were carried out to confirm the reproducibility of this feature and the results show that this distinct feature appears in all measurements, but with altered positions (see Figure 8.2a).

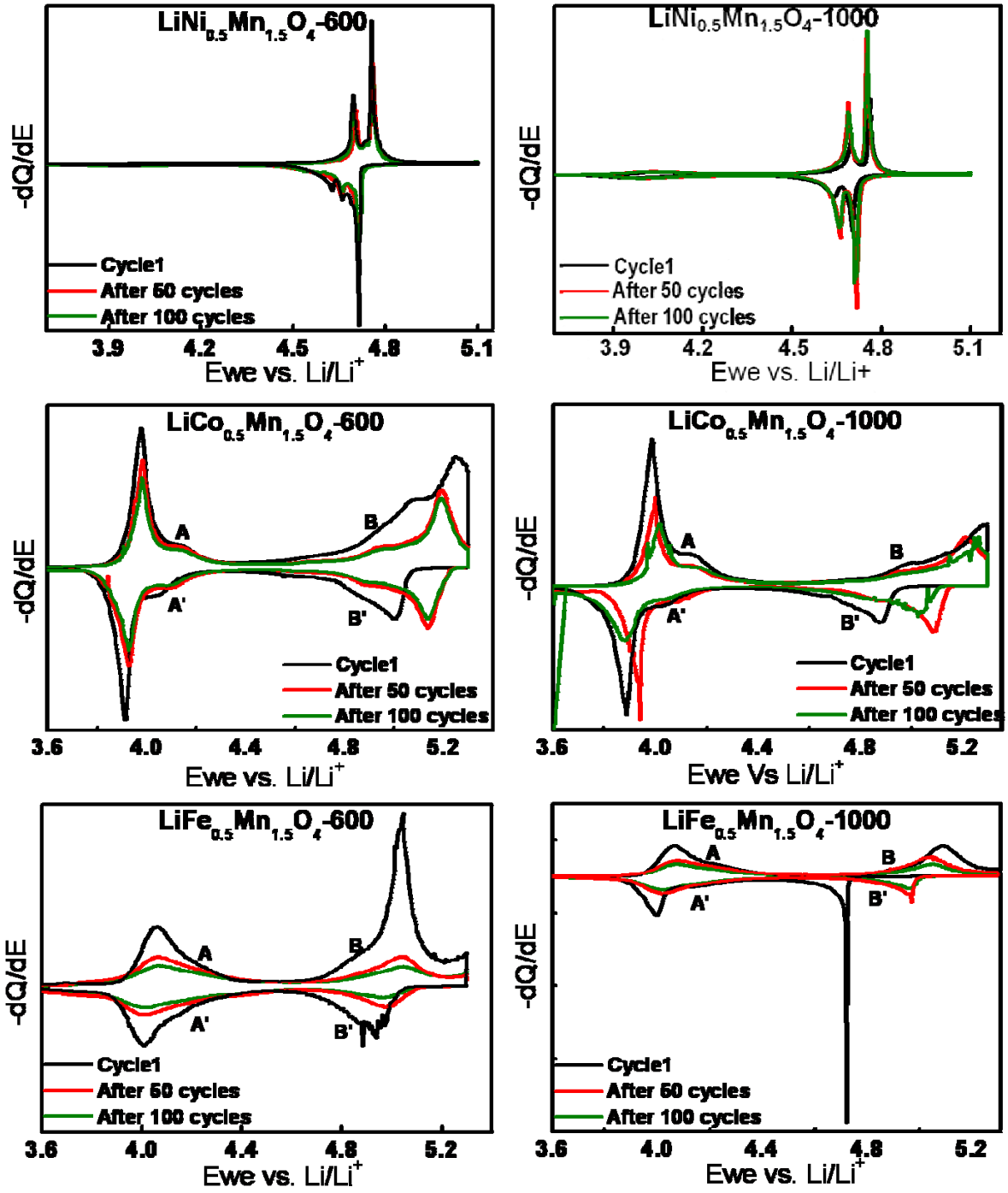

***Figure 8.1**: Differential capacity plots for (left) $LiM_{0.5}Mn_{1.5}O_4$-600, (M = Fe, Co, Ni) and (right) $LiM_{0.5}Mn_{1.5}O_4$-1000 (M = Fe, Co, Ni) samples with a cut-off current limit C/5.*

To understand the origin of this effect, a new set of PITT experiments was implemented by introducing an OCV (open circuit voltage) period after charging the cell with a cut-off current C/5. During this OCV periods no external electric current

between the electrodes is applied, but the voltage of the cell is continuously registered. The duration of the OCV period was varied in each experiment as 5 h, 10 h and 30 h. The observed voltage drops during the OCV period were 0.354 V, 0.342 V and 0.710 V for 5 h, 10 h and 30 h, respectively. The corresponding discharge capacities observed were 61 $mAhg^{-1}$, 78 $mAhg^{-1}$ and 88 $mAhg^{-1}$ respectively. Hence it can be concluded that the self-discharge during these voltage drops is insignificant and the voltage drop during OCV period is not due to self-discharge, but due to relaxation process only.

The results of these experiments are displayed in Figure 8.2. By introducing an OCV period of 5 h after charging, the sharp peak disappears and instead two broad peaks are visible, with the second peak more close to 5.0 V. When the OCV period was increased to 10 h the two broad peaks remain, but a variation in the peak ratio is visible (now the peak closer to 5.0 V is more pronounced). With the increase in the OCV period to 30 h, only one peak is visible and now the peak position is close to 5.0 V (see Figure 8.2b, c and d).

As the character of discharge peak in the first cycle of $LiFe_{0.5}Mn_{1.5}O_4$-1000 seems to be determined by the kinetic parameters, a slower PITT experiment was conducted with a cut-off current of C/20 without introducing any OCV period after charging. The sharp peak closer to 4.7 V disappears now completely, instead a broad peak closer to 5.0 V is only visible, see Figure 8.2 e. Therefore, the extremely sharp peak in the 5.0 V discharge capacity region of the $LiFe_{0.5}Mn_{1.5}O_4$-1000 sample was evolved as a result of the kinetic limitations in the first discharge. One of the possible explanations can be slower kinetic of lithium insertion into bigger particles (about 2.0 – 4.0 μm size) comparing to lithium extraction. After the first cycle, the material seems to undergo a structural relaxation and acquires a better kinetics in the following cycles, as revealed by the absence of this sharp peak when cycled at the same C-rate. This conditioning step will be further elucidated by detailed *in situ* structural investigations which are presented in chapter 9.

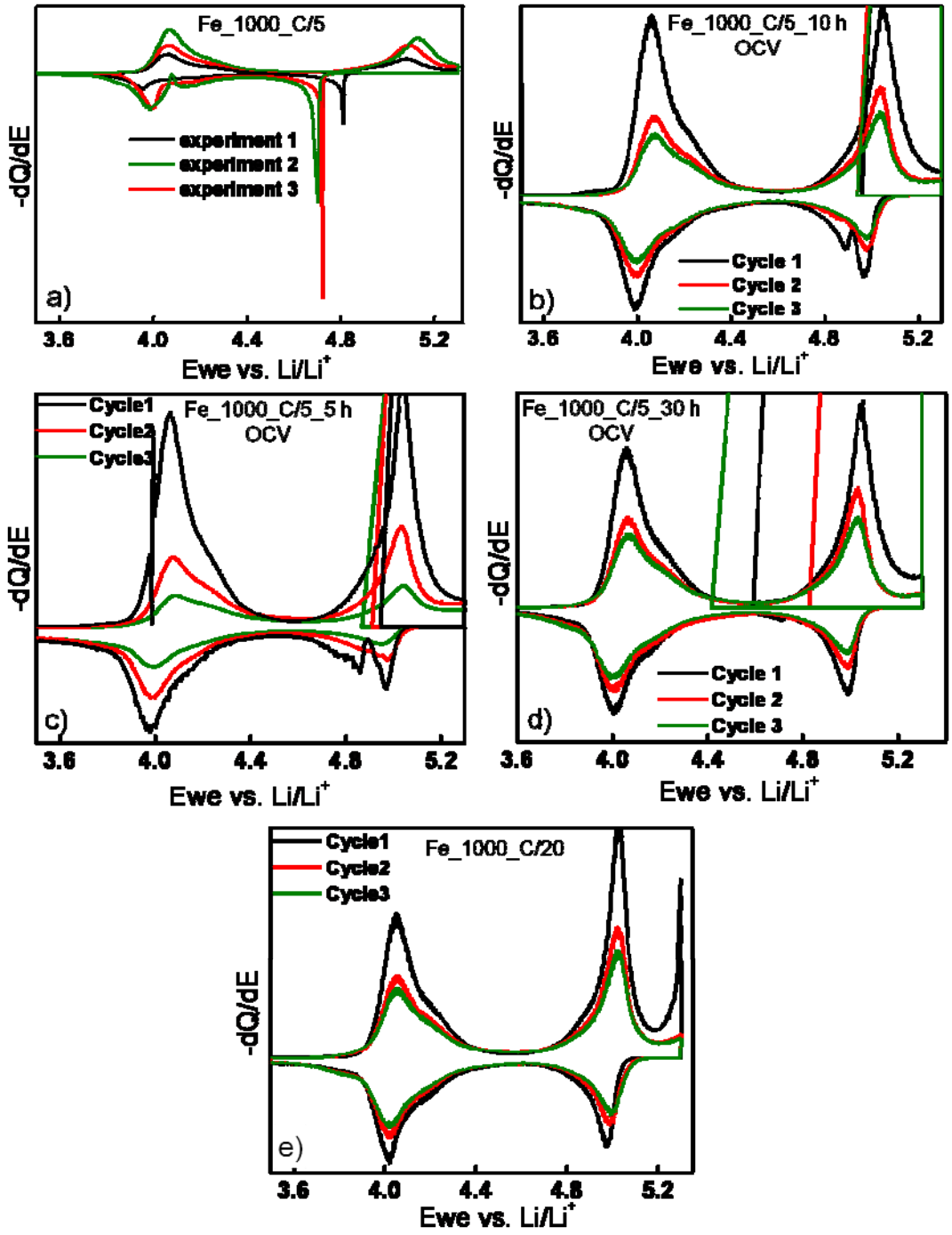

***Figure 8.2**: (a) Three independent measurements showing the reproducibility of the sharp peak in the discharge capacity region of the first cycle, for $LiFe_{0.5}Mn_{1.5}O_4$-1000, with a cut-off current C/5, (b, c, d) $LiFe_{0.5}Mn_{1.5}O_4$-1000 with a cut-off current C/5 and an OCV period of 5 h, 10 h and 30 h, respectively, after charging, (e) $LiFe_{0.5}Mn_{1.5}O_4$-1000 with a cut-off current C/20.*

8.2 Cycling stability studies

8.2.1 At room temperature

Cycle life is an important parameter to determine the suitability of a battery for a specific application. Hence a good cyclability has a higher industrial value. The cycling stability of the $LiM_{0.5}Mn_{1.5}O_4$ (M = Ni, Co, Fe) was studied by galvanostatic cycling experiments at a charge-discharge rate of C/2. For the Ni substituted spinel, a voltage range of 3.5 - 5.1 V was used and for the Co and Fe substituted spinels a voltage range of 3.5 - 5.3 V was applied. Several experiments were conducted for each material to check the reproducibility and hence in most cases the obtained initial capacity and capacity retention values are represented as calculated average obtained from repeated experiments with the standard deviation and number of experiments in brackets, separated by ";".

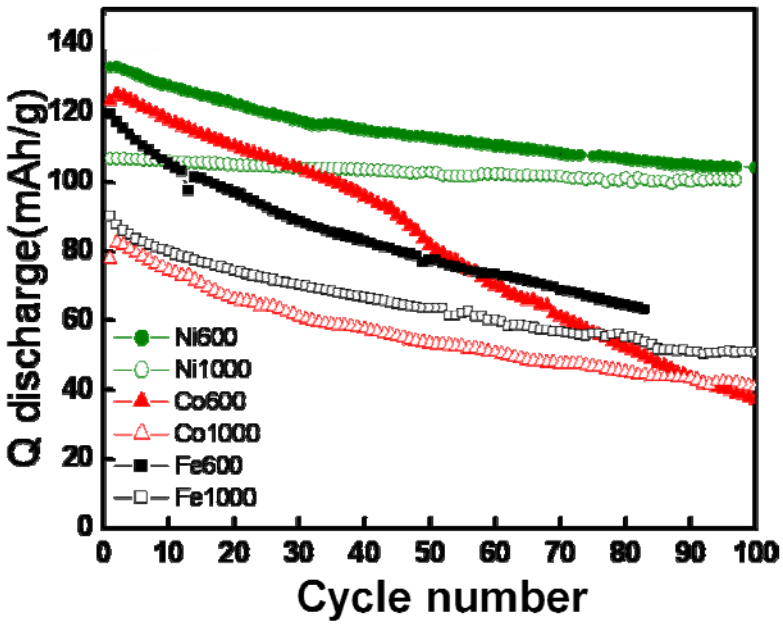

***Figure 8.3**: Discharge capacity vs. cycle number plots for $LiM_{0.5}Mn_{1.5}O_4$-600 (M = Fe, Co, Ni) and $LiM_{0.5}Mn_{1.5}O_4$-1000 (M = Fe, Co, Ni) with a charge-discharge rate C/2 at RT.*

The 600°C annealed $LiNi_{0.5}Mn_{1.5}O_4$, $LiCo_{0.5}Mn_{1.5}O_4$ and $LiFe_{0.5}Mn_{1.5}O_4$ delivered initial capacities such as 133, 115(8;2) and 104(11;3) $mAhg^{-1}$ respectively and the

capacity retention after 70 cycles were found to be 81%, 41(8;2)% and 58(3;3)% respectively. Instead in the case of the samples after fast excursion to 1000°C, the initial capacities were found to be slightly lower and the values are 107 $mAhg^{-1}$ for Ni, 77(6;2) $mAhg^{-1}$ for Co and 89.5(0.5;2) $mAhg^{-1}$ for Fe, respectively, whereas these samples exhibited an enhanced capacity retention such as 95% for Ni, 55(3;2)% for Co and 59(4;2)% for Fe respectively after 70 cycles. Selected experiments as representatives are displayed in Figure 8.3.

The Li$M_{0.5}Mn_{1.5}O_4$-600 samples demonstrate lower residual capacities than the Li$M_{0.5}Mn_{1.5}O_4$-1000 samples after 110 cycles for M = Ni and after more than 90 cycles for M = Co. The superior capacity retention of Li$M_{0.5}Mn_{1.5}O_4$-1000 (M = Fe, Co, Ni) samples could be attributed to the higher degree of crystallinity, smoother particle surface of the sample and a reduced available active surface due to the particle size increase after the fast heating up to 1000°C. All these factors may play a role in suppressing the degradation phenomena in the prepared cells when cycled in a higher voltage range. Another cause could be the suppressed release of oxygen from the spinel framework of the 1000°C treated samples, in the highly charged state which is more feasible for 600°C annealed samples; as the former is already slightly oxygen deficient from the high temperature treatment. A work done by Caballero et al. in 2005 have reported in support to the above proposition that the oxygen release from the framework might cause structural damage on the crystal surface which could in turn result in inferior cell performance [**Caballero 2005**].

The voltage profiles of the Li$M_{0.5}Mn_{1.5}O_4$-1000 samples during galvanostatic cycling are displayed in Figure 8.4. It can be seen that always the charge capacity is noticeably higher than the discharge capacity in the first cycle. There is an irreversible capacity loss in the first cycle, which could be an indication of the side reactions in the first cycle. The difference between the charge and discharge capacities reduces after the first few cycles and reaches negligible values, as illustrated by the plots for 50^{th} and 100^{th} cycles in Figure 8.4, which indicates that the efficiency of the system reaches equilibrium, possibly due to passivation phenomena.

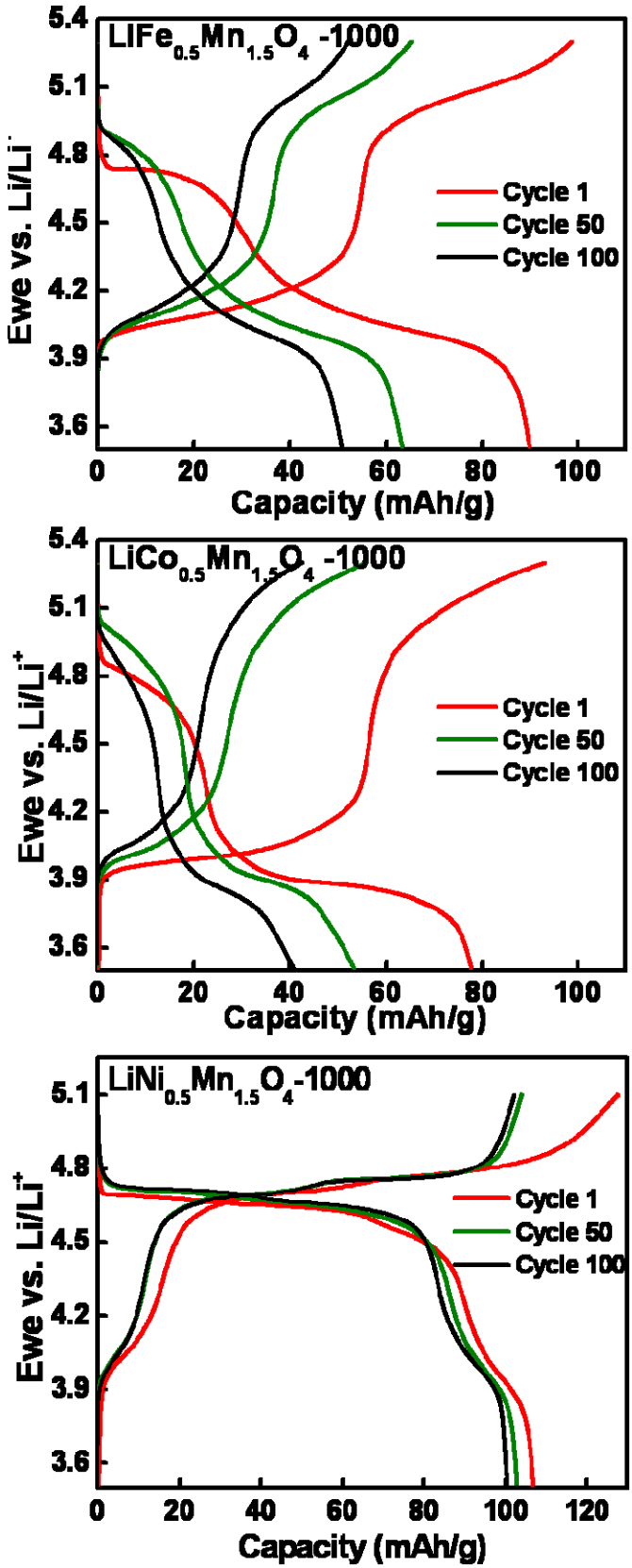

***Figure 8.4**: Voltage vs. capacity plots for $LiM_{0.5}Mn_{1.5}O_4$-1000 (M = Fe, Co, Ni) with a charge-discharge rate C/2 at RT.*

8.2.2 At elevated temperature (55°C)

The synthesized materials were also tested for their electrochemical performance at elevated temperature. The temperature was chosen as 55°C as many previous studies were reported at this temperature for other materials and hence a comparison would be more conclusive [**Eftekhari 2003**]. At higher temperatures (~70°C) the organic electrolyte starts to decompose **[Xu 2004]**.

Comparing to RT performance, the cycling behavior at 55°C is different for both sets of the samples. For 600°C annealed samples, the initial capacities obtained were 125 $mAhg^{-1}$ for Ni substituted, 116 $mAhg^{-1}$ for Co substituted and 145 $mAhg^{-1}$ for Fe substituted samples respectively and the capacity retention values were found to be correspondingly 60% for Ni, 21% for Co and 5% for Fe after 50 cycles. The initial capacities delivered by the 1000°C annealed samples at 55°C were 108 $mAhg^{-1}$ for Ni, 95(7;3) $mAhg^{-1}$ for Co and 83(15;4) $mAhg^{-1}$ for Fe, respectively. After 50 cycles, 96% capacity retention was found in the case of $LiNi_{0.5}Mn_{1.5}O_4$-1000 which was much higher in comparison with the 25(1;3)% and 14(4;4)% capacity retentions observed for $LiCo_{0.5}Mn_{1.5}O_4$-1000 and $LiFe_{0.5}Mn_{1.5}O_4$-1000 respectively. This significantly faster degradation is clearly seen in Figure 8.5 which shows selected data with representative behavior. In one of the experiments at 55°C conducted on the $LiFe_{0.5}Mn_{1.5}O_4$-1000 sample, an initial capacity of 98 $mAhg^{-1}$ and a capacity retention of 43% was measured which was outstandingly high in comparison with all other measurements on the same sample (see Figure 8.6 a). The reason for this could be that the cell was not heated enough to reach 55°C as the capacity retention value is much closer to that obtained for the experiment at RT.

The elevated cycling stability of $LiNi_{0.5}Mn_{1.5}O_4$ material was reported before [**Markovsky 2004, Fang 2007**] and is ascribed to the exceptional surface chemistry of this material, leading to the formation of stable solid-electrolyte interface in aprotic electrolytes [**Aurbach 2006**]. However, the $LiNi_{0.5}Mn_{1.5}O_4$-1000 samples from our group delivered excellent capacity retention at 55°C at a rate of C/2 after 50 cycles (97% retention at C/5 for commercial $LiNi_{0.5}Mn_{1.5}O_4$ from LG Chem. at 60°C after 50 cycles reported by Aurbach et al. [**Aurbach 2006**]). Moreover the existence of Mn in a higher oxidation state (Mn^{4+}) in $LiNi_{0.5}Mn_{1.5}O_4$ stabilizes this material against dissolution of Mn in the acidic species of the electrolyte. The Mn dissolution is found to occur if its oxidation state is lower than +3.5 and results in a rapid degradation in

$LiMn_2O_4$ spinel when cycled at elevated temperatures [**Thackeray 1997**]. The lower voltage of Ni^{2+}/Ni^{4+} reaction in comparison with the Co^{3+}/Co^{4+} and Fe^{3+}/Fe^{4+} could also be a reason for superior stability of $LiNi_{0.5}Mn_{1.5}O_4$ with respect to Co and Fe samples. Except for a work on thin film $LiFe_{0.5}Mn_{1.5}O_4$ electrodes by Eftekhari, not much reports are available in the literature about the elevated temperature cycling behavior of $LiM_{0.5}Mn_{1.5}O_4$ (M = Fe, Co) at 5 V in the literature **[Eftekhari 2004]**. Hence a comparison is not possible with previous works. The increased degradation in $LiM_{0.5}Mn_{1.5}O_4$-600 (M = Fe, Co, Ni) samples is of the same trend shown by them during RT cycling and could be a result of the extra available active surface for parasitic reactions and oxygen-release effects as described before. Hereafter the 1000°C annealed samples were used for the high temperature investigations due to their superior behavior.

In completely stoichiometric $LiCo_{0.5}Mn_{1.5}O_4$ and $LiFe_{0.5}Mn_{1.5}O_4$, the nominal oxidation state of Mn is +3.67, when M is considered to be M^{3+} (M = Fe, Co). The discrepancy in the stoichiometry revealed by neutron diffraction studies ($LiFe_{0.44}Mn_{1.56}O_4$) implies a slightly lowered oxidation state +3.64 for Mn. In principle, the fast excursion to 1000°C would have resulted in an oxygen deficiency and hence a change in the Mn oxidation state again to slightly lower values in $LiFe_{0.44}Mn_{1.56}O_4$ and $LiCo_{0.48}Mn_{1.52}O_4$ (the calculated stoichiometries from neutron diffraction) in comparison with $LiNi_{0.5}Mn_{1.}5O_4$ and this might be a reason for the quick degradation of these materials at elevated temperature cycling. In contrast the end-of-charge voltage applied for cycling for Co- and Fe-doped spinels is slightly higher, which may in turn lead to electrolyte decomposition reactions. To understand this point and hence the real source of fatigue in more detail, the high temperature (at 55°C) cycling experiments were conducted for $LiCo_{0.5}Mn_{1.}5O_4$-1000 and $LiFe_{0.5}Mn_{1.5}O_4$-1000 in two different voltage regions at a cycling rate of C/2. The two voltage regions were selected by dividing the usual voltage range 3.5 - 5.3 V. The first range was chosen from 4.4 - 5.3 V in order to exclude the Mn^{3+}/Mn^{4+} couple and the other was from 3.5 - 4.4 V, hereafter will be referred as 5 V and 4 V regions respectively.

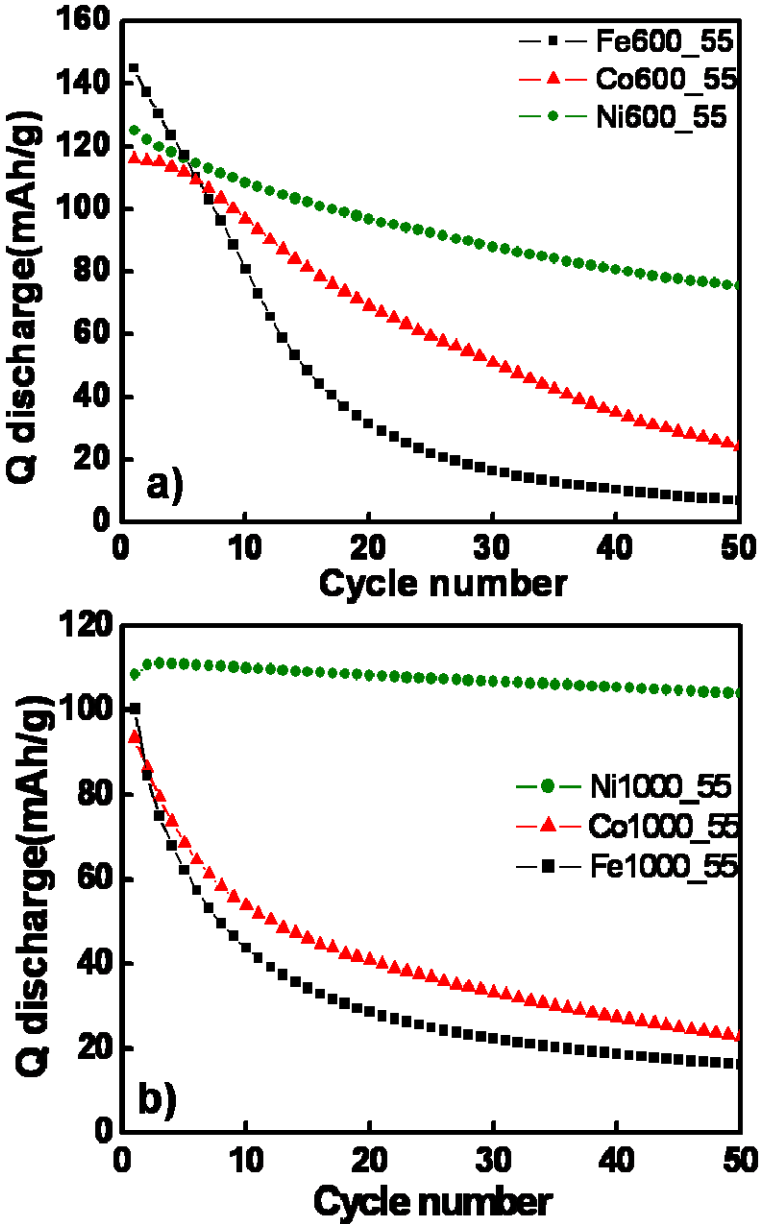

Figure 8.5: *Discharge capacity vs. cycle number plots for $LiM_{0.5}Mn_{1.5}O_4$-600 and $LiM_{0.5}Mn_{1.5}O_4$-1000 (M = Fe, Co, Ni) with a charge-discharge rate C/2 at 55°C.*

In the 5 V region measurements, Co and Fe substituted samples show an initial capacity of 35(4;4) $mAhg^{-1}$ and 22(2;3) $mAhg^{-1}$, respectively, with a capacity retention of 68(14;4)% for Co and 35(20;3)% for Fe after 50 cycles, shown in Figure 8.6 b. The 4 V region measurements show much stable behavior in comparison with the 5 V cycling, where the transition metal-doped samples delivered an initial capacity of 53 $mAhg^{-1}$ for Co and 56(4;2) $mAhg^{-1}$ for Fe with a capacity retention of 93% and

80(6;2)% after 50 cycles for Co and Fe, respectively. The fatique occurs mostly in high-voltage region and may be caused by either Fe/Co redox reaction or electrolyte degradation.

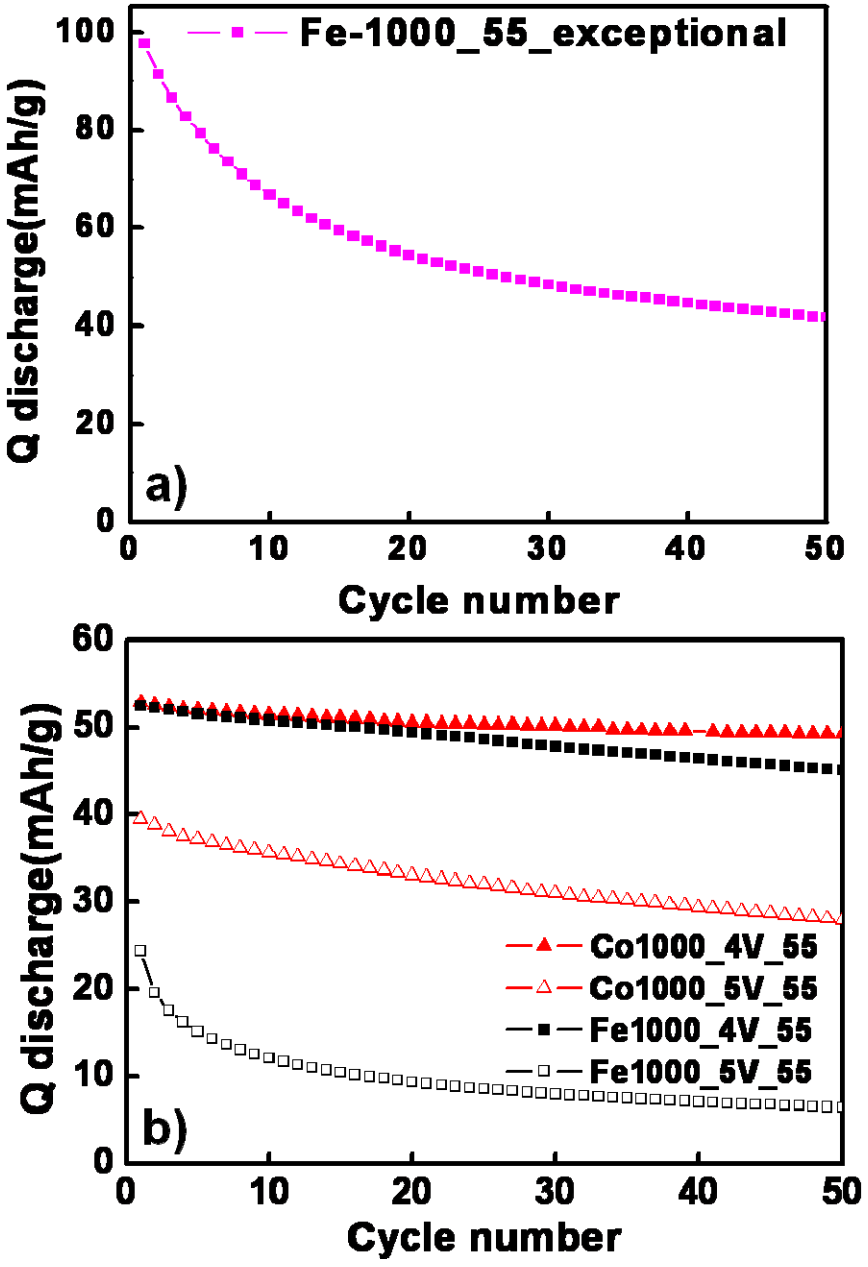

Figure 8.6: *Cyclability experiment from (a) $LiFe_{0.5}Mn_{1.5}O_4$-1000 where exceptionally high capacity retention is observed (b) $LiFe_{0.5}Mn_{1.5}O_4$-1000 and $LiCo_{0.5}Mn_{1.5}O_4$-1000 in 4 V and 5 V regions at C/2 at 55°C.*

In order to understand the nature of the capacity loss, dedicated galvanostatic cycling experiments were carried out by subjecting the prepared cells to cycle at 55°C for first

50 cycles and then to RT for another 50 cycles. A relaxation period of 1 h was applied in between the two successive experiments in order to cool down the cells to RT. The obtained results are displayed in Figure 8.7a and it shows that there is no capacity regain for the 55°C cycled cell when the experiment is again performed at RT. The reasons for this permanent loss could be:

- The destruction of the spinel structure at 55°C in contact with the electrolyte, especially when the material is in its completely charged state during the galvanostatic cycling.

- The electrolyte decomposes to produce some byproducts which serve as a hindering medium on the surface of the electrodes for lithium intercalation.

The cathodes were then used to assemble new cells with fresh separators, lithium anode and electrolyte and cycled again at RT. The results again showed no improvement in the capacity regain (see Figure 8.7 b). Hence electrolyte decomposition may be a reason and the resultant products, which cannot be removed by washing with DMC, could hinder the lithium transfer on the electrode surface.

To investigate the structural changes of the electrode materials upon cycling, X-ray diffraction analyses were performed on the cathodes after 50 cycles at 55°C. The results are shown in Figure 8.8. No new phases were observed after cycling; the Fe and Co-doped samples remain single phase ($Fd\bar{3}m$ space group) as similar to the samples before cycling. The lattice parameters in the discharged state were found to be 8.1453(3) and 8.2107(8) for $LiCo_{0.5}Mn_{1.5}O_4$-1000 and $LiFe_{0.5}Mn_{1.5}O_4$-1000 respectively. These values reveal a contraction of the unit cell, 0.57% and 0.25% respectively for Fe- and Co-doped samples, when compared with the values before cycling (8.1660(2) for $LiCo_{0.5}Mn_{1.5}O_4$-1000 and 8.2575(2) for $LiFe_{0.5}Mn_{1.5}O_4$-1000). The above comparison also points out that the extent of lithium re-intercalation is more than 80% for Co-doped sample and more than 70% for Fe-doped samples (obtained from a comparison of unit cell shrinkage calculated with respect to the unit cell parameter vs. number of moles of lithium remains plot shown in Figure 9.6a and b, chapter 9). Hence it could be concluded that this permanent capacity loss is not due to any structural degradation, rather during cycling the lithium diffusion is limited due to kinetic hindrance.

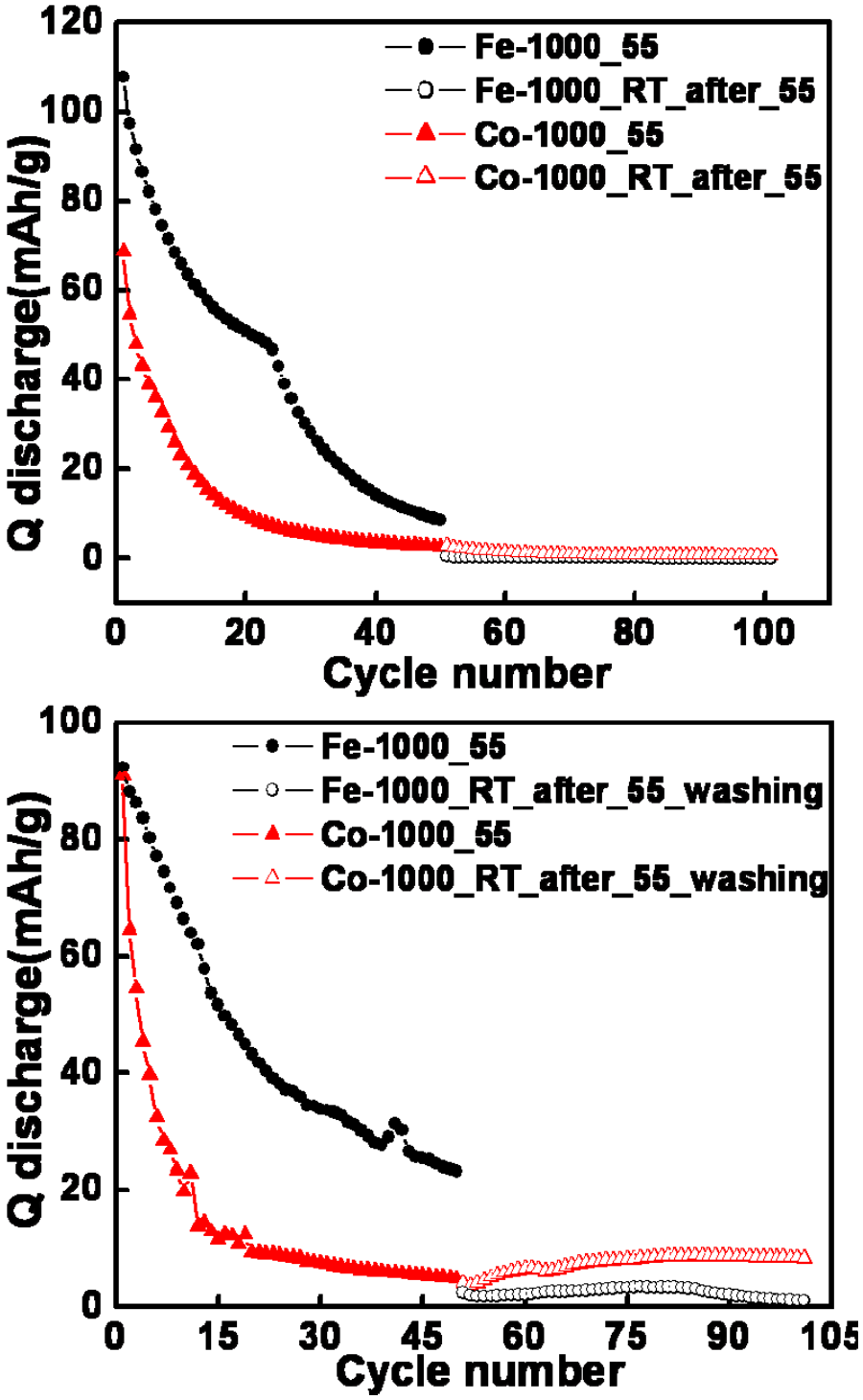

Figure 8.7: *Results from capacity regaining experiments showing a permanent capacity loss when cycled at RT after 50 cycles at 55°C. (a) without washing the cathodes after 55°C cycling (b) with washing the cathodes after 55°C cycling.*

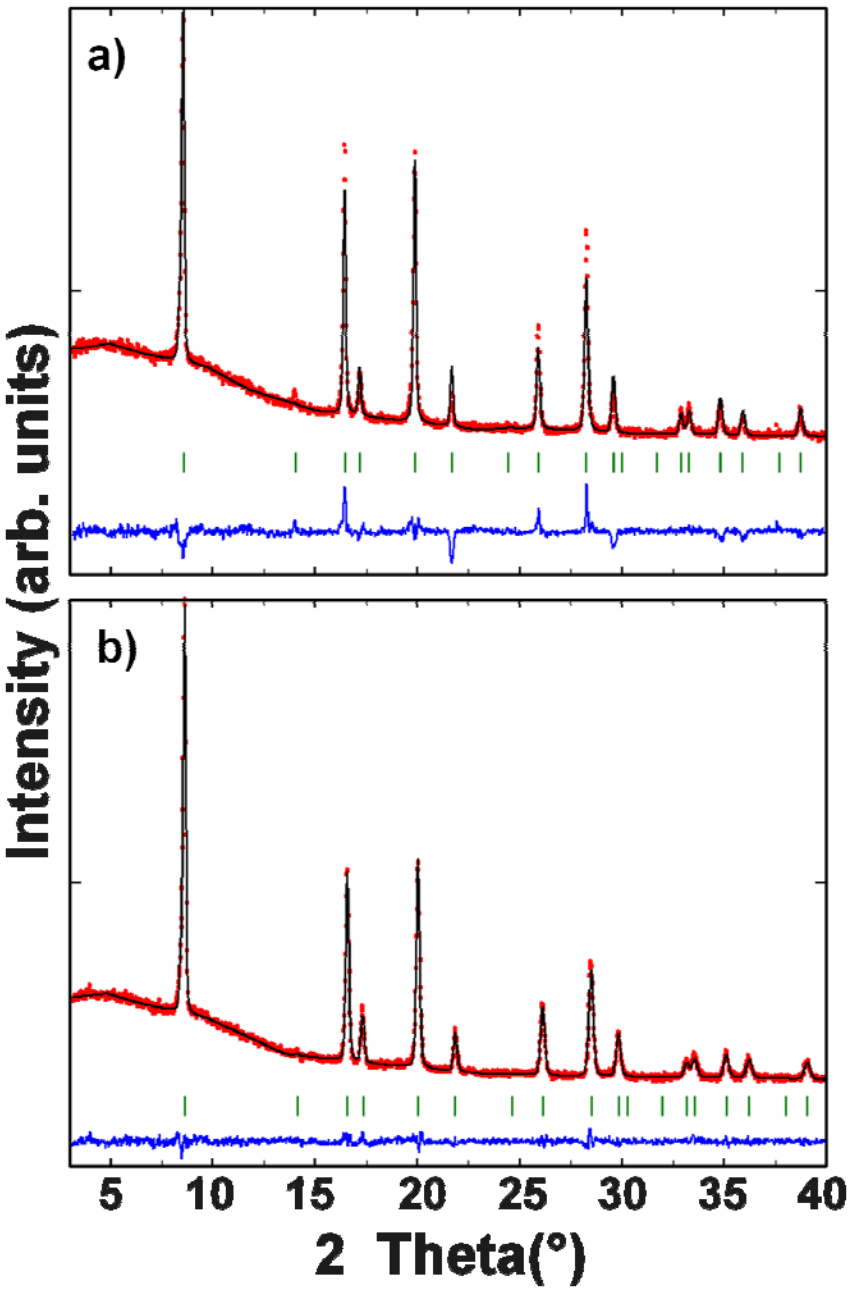

Figure 8.8: *XRD patterns at RT, after 50 cycles at 55°C. (a) $LiFe_{0.5}Mn_{1.5}O_4$-1000 based on $Fd\bar{3}m$ space group (b) $LiCo_{0.5}Mn_{1.5}O_4$-1000 based on $Fd\bar{3}m$ space group.*

8.2.3 XPS analysis

A quasi *in situ* X-ray photoelectron spectroscopy was performed to investigate the chemistry of surfaces and the valence state of surface species in $LiM_{0.5}Mn_{1.5}O_4$-600

(*M* = Fe, Co, Ni) cathodes [**Oswald 2009**]. The cathodes were studied in two different states: as prepared and cycled after 50 cycles at 1C (the cell was in completely discharged state at the end of the 50th cycle), respectively.

The results of the quasi *in situ* X-ray photoelectron spectroscopy performed on the Li$M_{0.5}$Mn$_{1.5}$O$_4$-600 (*M* = Fe, Co, Ni) cathodes are shown in Figures 8.9 and 8.10. In order to compare, all the spectra are calibrated in terms of binding energy of C 1*s* position at 284.8 eV. For comparison of the spectral shapes, the intensities of the spectra were normalized within each window separately. As a consequence, the intensities do not illustrate relative concentration of elements measured. The main features derived from the spectra are given below.

- Co 2*p* (Figure 8.9): The binding energy values for Co 2*p* remain constant (780.5 eV) except for the slight broadening of the peaks, after cycling which may be attributed to different extent of lithium insertion (existence of particles on the electrode surface with different amount of lithium) after the high-rate cycling. A well pronounced shake up satellite is visible at a binding energy difference of 9.5 eV from the Co 2$p_{3/2}$ peak which reveals the presence of trivalent Co in the sample. The cycled sample exhibits a shake up satellite at a binding energy difference of 6.2 eV from the Co 2$p_{3/2}$ peak, with a rather low intensity, which is an indication of the presence of slight amount of Co^{2+} [**Dahéron 2008**] also in the sample may be formed as a result of some disproportionation reaction of Co^{3+}.

- Mn 2*p*: (Figure 8.9): Mn 2$p_{3/2}$ is observed at a binding energy of 642.3 eV for Li$M_{0.5}$Mn$_{1.5}$O$_4$-600 (*M* = Fe, Co, Ni) electrode materials before and after cycling. It is difficult to obtain the distribution of trivalent and tetravalent oxidation states from XPS [**Oswald 2009**], but complimentary electrochemical experiments revealed the presence of a mixture of trivalent and tetravalent states of Mn in Co- and Fe-doped materials and only tetravalent oxidation state in the Ni-doped material. The absence of any satellite peaks, characteristic for the divalent Mn rules out the possibility of its existence in the material [**Hernán 2002**].

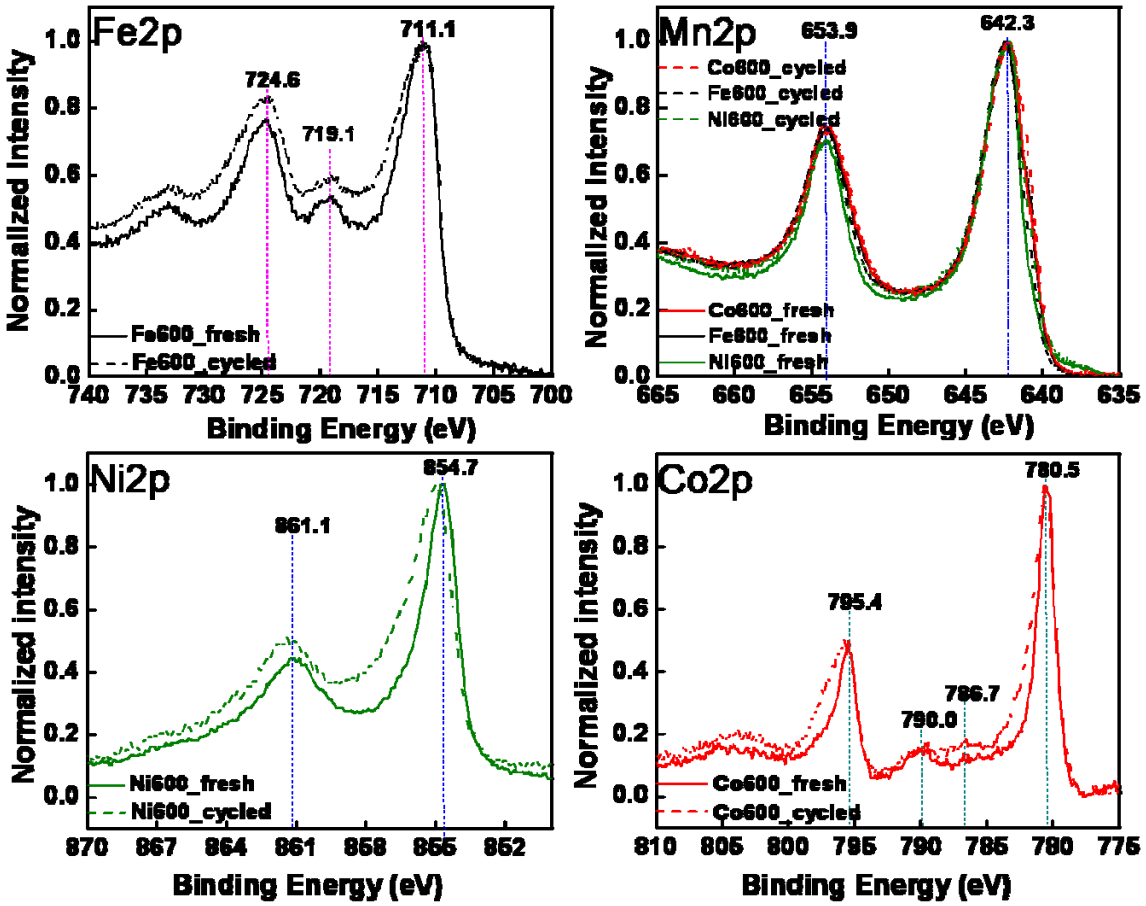

Figure 8.9: *Me 2p (Me = Fe, Co, Ni, Mn) XPS spectra measured for $LiM_{0.5}Mn_{1.5}O_4$-600 (M = Fe, Co, Ni) system: As prepared cathode materials are shown as solid lines and cycled materials are shown as broken lines.*

- Ni 2*p*: (Figure 8.9): The binding energy of Ni $2p_{3/2}$ (854.7 eV) is close to what reported for $LiNi_{0.5}Mn_{1.5}O_4$ spinel (854.0 eV) and slightly lower than that reported for Ni-based spinels ($NiMn_2O_4$, 855.2 eV) indicating the existence of nickel in its divalent oxidation state [**Hernán 2002**]. In addition, this emission peak also has a fine structure associated with shake up processes, which are specific for Ni (II) compounds [**Hernán 2002**]. While the fresh sample exhibits a narrow and symmetric peak, a broadening is visible for the cycled samples, which could be an indication of the different extent of lithium insertion.

- Fe 2*p*: (Figure 8.9): The binding energy of Fe $2p_{3/2}$ (711.1 eV), the separation of Fe $2p_{3/2}$ and Fe $2p_{1/2}$ spin orbit level (13.4 eV) and the difference between the Fe $2p_{3/2}$ and the satellite (8.0 eV) are in good consistency with the values

reported for trivalent Fe in $LiFe_{0.3}Mn_{1.7}O_4$ by Hernán et al. [**Hernán 2002**]. A broadening of the peaks are visible after cycling as in the case of Co and Ni samples, which could be an indication of different extent of lithium insertion.

- O 1*s*: (Figure 8.10): The O 1*s* peak in the case of as prepared cathode has a major contribution from the $LiM_{0.5}Mn_{1.5}O_4$-600 (*M* = Fe, Co, Ni) electrode material at 529.7 eV and a broad weak signal in the range of 532.0 - 533.0 eV, which is more pronounced for the cycled cathodes, probably originated from the presence of Li_2O, Li_2CO_3 or from the SEI formation during cycling.

- C 1*s*: (Figure 8. 10): The peak at 284.4 eV is mainly a contribution from the carbon additive. The cycled cathodes could also have a contribution from the dried electrolyte. The two other features, detected at ~286.0 eV and 290.4 eV are characteristic for the PVDF [**Oswald 2009**].

- F 1*s*: (Figure 8. 10): There are mainly two contributions in the case of cycled cathodes: one at 687.7 eV is from the PVDF binder and the others at about 685.0 and 684.0 eV is from the residual fluorinated compounds like LiF_x or $LiPF_6$ [**Oswald 2009**]. In the case of as-prepared cathodes, the peaks representing the residual fluorinated compound has a smaller ratio in comparison with those for the corresponding cycled cathodes, which could be attributed to the fact that the fresh cathodes lack the presence of any residual $LiPF_6$ which is the major contributor in this binding energy region.

- Li 1*s*: (Figure 8. 10): A broad Li 1*s* peak with two spectral features could be observed near to the Mn 3*p* peak. The first one at ~53.7 eV could be assigned to the lithium in the electrode material and the second contribution at ~55.7 eV is a signature of fluorine containing compounds (LiF_x, $LiPF_6$ etc) [**Oswald 2009**]. In the broad region, there could be also contributions from Li_2O and Li_2CO_3. Again it could be observed that the peak ratios from fresh cathodes are slightly lower than the corresponding cycled ones and the reason could be the lack of $LiPF_6$ in the fresh cathodes.

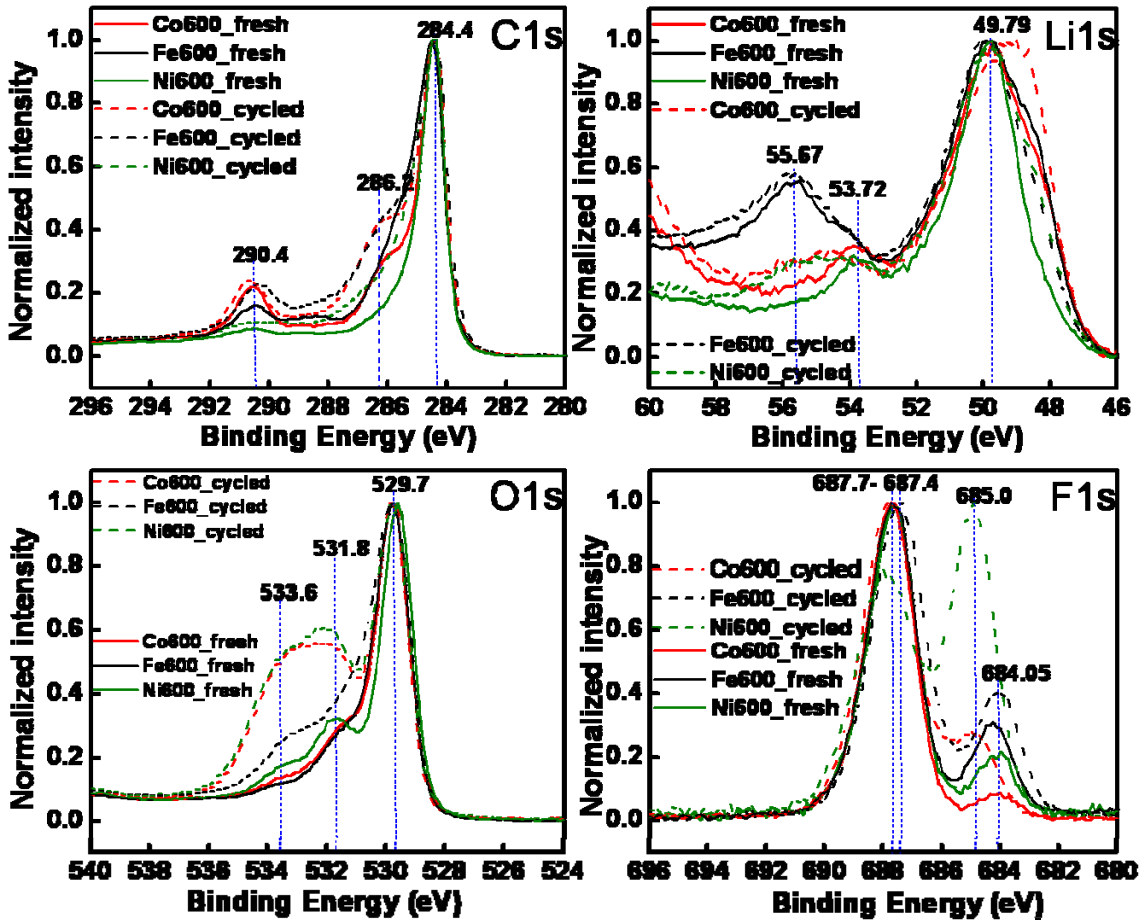

Figure 8.10: *C 1s, O 1s, Li 1s and F 1s XPS spectra measured for* $LiM_{0.5}Mn_{1.5}O_4$*-600 (M = Fe, Co, Ni) system: As prepared cathode materials are shown as solid lines and cycled materials are shown as broken lines.*

8.3 Rate capability studies

For the high power applications, the battery should show good cyclability at diverse C-rates or in other words, it should exhibit higher rate capability. The rate capability studies are normally performed by cycling the battery for a fixed number of cycles under subsequently varied C-rates. In the present work the rate capability studies are often performed using rates such as C/5, C/2, 2C, 10C, 20C and C/5 in the respective order. In detail, the charge/discharge rates were increased after sets of 5 cycles successively from C/5 in the first 5 cycles up to 20C for the 21st - 25th cycles and the lower C/5 rate was used again from 26th - 30th cycles. Figure 8.11 shows the results

obtained for the rate capability experiments for Li$M_{0.5}$Mn$_{1.5}$O$_4$-600 (M = Fe, Co, Ni) and Li$M_{0.5}$Mn$_{1.5}$O$_4$-1000 (M = Fe, Co, Ni).

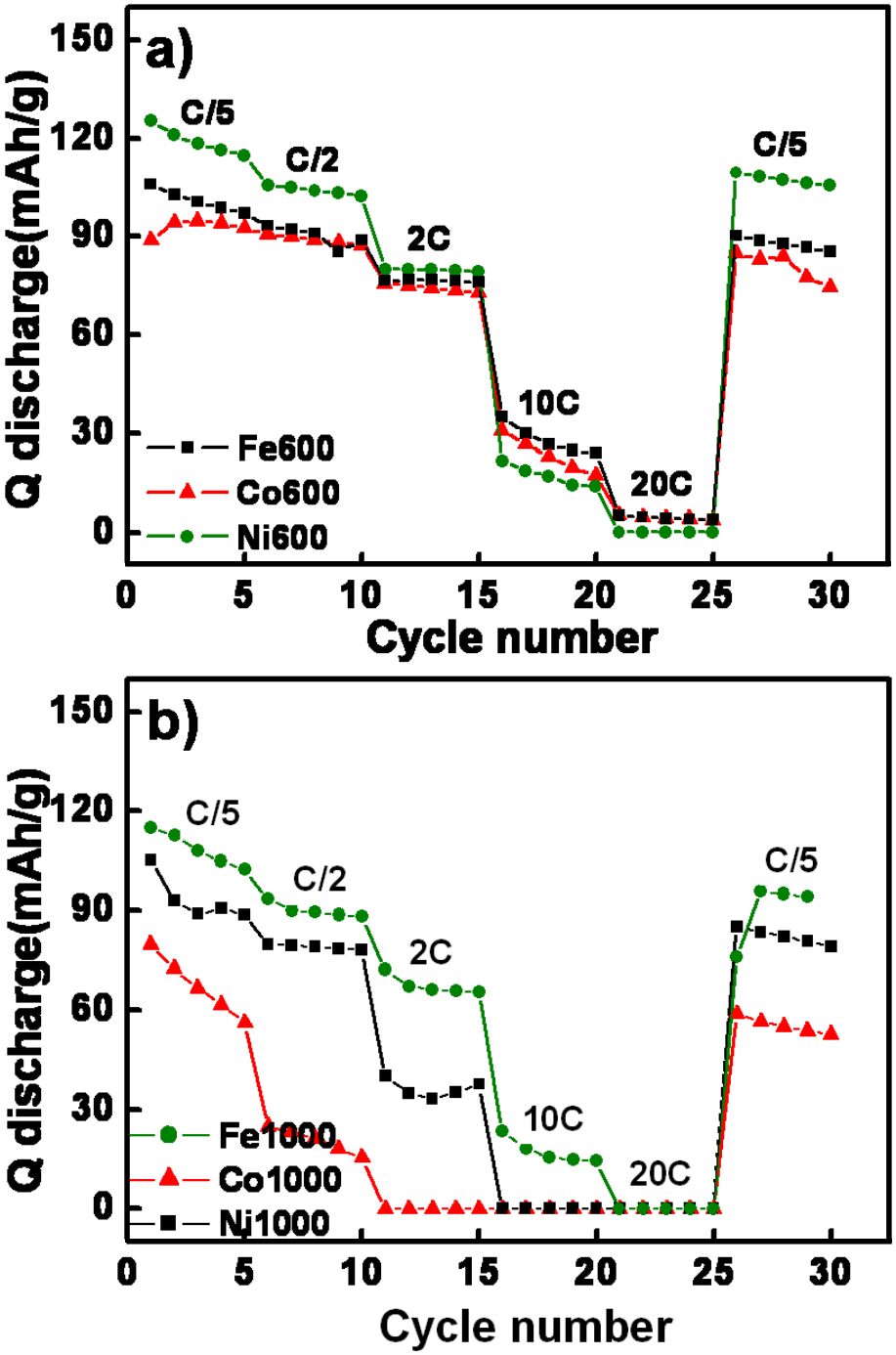

***Figure 8.11**: Variation of discharge capacities with cycle number for (a) Li$M_{0.5}$Mn$_{1.5}$O$_4$-600 (M = Fe, Co, Ni) and (b) Li$M_{0.5}$Mn$_{1.5}$O$_4$-1000 (M = Fe, Co, Ni) at RT at different C-rates where the 600°C annealed samples show a superior performance.*

A comparison between the samples with respect to the doping transition metal reveals that they exhibit similar behavior irrespective of the doped metal ion except for a slightly higher discharge capacity of $LiNi_{0.5}Mn_{1.5}O_4$ at higher C rates. Hence the rate capability is found independent from the nature of dopant cations. The capacities at the end of the cycling (from 26^{th} to 30^{th} cycles) are slightly lower than the initial capacities (from cycles 1 - 5) at the same charge-discharge rate, probably, due to the degradation of the cells during cycling. However, no serious irreversible damage could be concluded at the end of the cycling as these values of the discharge capacity are still close to the initial values at C/5.

8.4 Electrochemical performance of optimized cathodes

The optimization of cathodes with aluminum foils are described in section 6.4, chapter 6. The obtained cathodes from experiment III exhibited stronger adhesion of the material to the aluminum foil than those from experiments I and II. These were then subjected to electrochemical characterization and the results (see Figure 8.12) revealed that the cathodes prepared by experiment III showed a superior cycling behavior, especially at 55°C, to those from experiments I and II, which is very similar to the behavior showed by the aluminum mesh cathode of the same material (see Figure 8.5). At the same time the rate capability of the cathodes from experiment III is also found very superior to that shown by the aluminum mesh cathodes and cathodes from experiments I and II, especially at higher C rate (~50 mAh/g at 20C for the optimized cathode from experiment III and ~0 mAh/g for the aluminum mesh cathode), see Figure 8.11. The performance differences between the foils from the three different experiments can be explained well with the support of the experiment III cathodes' higher adhesion to the aluminum foils. The different rate capabilities of the aluminum mesh and the aluminum foil cathodes can be accounted in terms of the difference in their geometry. The charge-discharge profiles for the first cycle are also displayed for a better comparison and these show similar behavior for all the prepared cathodes, except for a slightly higher initial capacity in the case of cathodes from experiment II.

The results of this optimization study demonstrates that optimization of the cathode preparation can result in significant improvement of the electrochemical performance, especially at high C-rates, for the spinel cathode materials even when the particle size is in micrometer range.

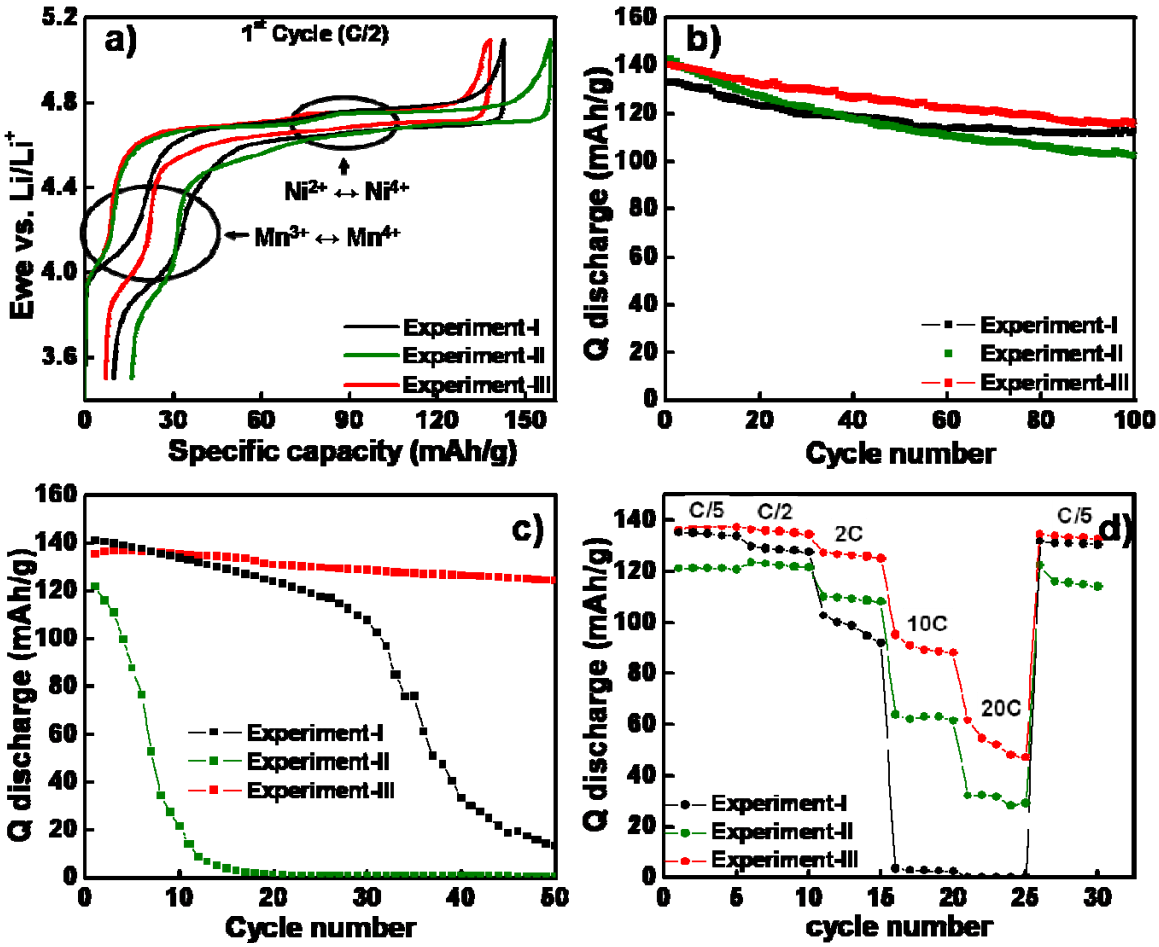

Figure 8.12: *The results of electrochemical characterization obtained for the prepared aluminum foil cathodes, $LiM_{0.5}Mn_{1.5}O_4$-1000 (M = Fe, Co, Ni), where cathodes from experiment III showing superior behavior: (a) charge-discharge profiles, (b) cycling behavior at RT, (c) cycling behavior at 55°C, (d) rate capability studies.*

Chapter 9
in situ investigation of Li-intercalation mechanism in $LiM_{0.5}Mn_{1.5}O_4$ (*M*= Fe, Co)

It is already seen in previous chapters that the cycling stability and cation ordering of substituted spinels varies with the dopant transition metal cation. $LiNi_{0.5}Mn_{1.5}O_4$ was found to show superior cycling behavior in comparison with $LiCo_{0.5}Mn_{1.5}O_4$ and $LiFe_{0.5}Mn_{1.5}O_4$. Also the 600°C annealed $LiNi_{0.5}Mn_{1.5}O_4$ showed a partially cation ordered structure, different from other investigated materials in this work. Hence it is interesting to compare the electrochemical charge-discharge mechanism of these three materials.

The mechanism of lithium extraction-insertion for $LiNi_{0.5}Mn_{1.5}O_4$ has been extensively discussed in the literature **[Kim 2004a, Park 2007, Ariyoshi 2004]**. Co and Fe-doped spinels are less investigated with respect to this aspect. Here, synchrotron diffraction study of delithiation mechanisms for Co- and Fe-doped spinels prepared in the same conditions was performed (1000°C heated up samples) and the behavior is discussed in comparison with the mechanism known for $LiNi_{0.5}Mn_{1.5}O_4$.

9.1 Cycling mechanism for $LiM_{0.5}Mn_{1.5}O_4$ (*M* = Fe, Co)

The voltage profiles in the *in situ* synchrotron diffraction experiments are shown in Figure 9.1a and b. The inset of each figure contains a plot of the number of moles of Li extracted/inserted vs. the potential (vs. Li/Li^+). The charge-discharge potential profiles of both samples show two plateaus in the ranges of ~3.9 - 4.3 V and 4.9 - 5.3 V, which correspond to the electrochemical reactions of Mn^{3+}/Mn^{4+} couple and M^{3+}/M^{4+} (*M* = Fe, Co) respectively, as marked in the figure [**Bhaskar 2010**].

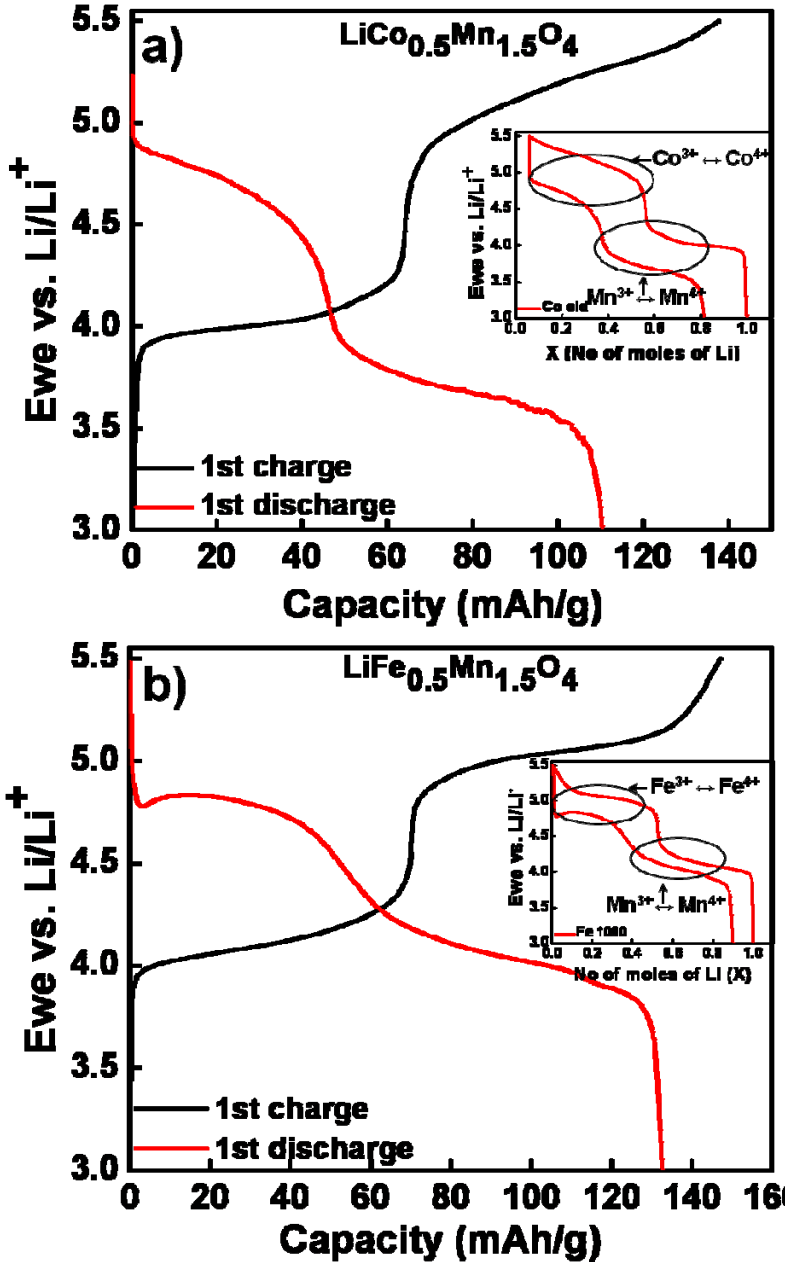

***Figure 9.1**: Charge-discharge potential profiles for (a) $LiCo_{0.5}Mn_{1.5}O_4$-1000 and (b) $LiFe_{0.5}Mn_{1.5}O_4$-1000 at RT at C/8.*

The *in situ* synchrotron diffraction patterns of the freshly prepared cell, after first charging and at the end of the first cycle for both samples are shown in Figure 9.2a and b. Reflections correspond to the spinel phase, assigned to $Fd\bar{3}m$ space group are shown as the top line of reflection marks in each pattern. Additional strong reflections could be assigned to aluminum from the cathode current-collector window. The Rietveld refinements for the Li$M_{0.5}Mn_{1.5}O_4$-1000 (M = Fe, Co) were performed based

on a structural model described in section 7.1, chapter 7. The Rietveld refinement was performed with a profile function 7 (Npr 7) for parameters such as scale factor, unit cell parameters "a", half width parameters (W and X), oxygen coordinates (U parameter) and thermal displacement parameter (B_{iso} with an isotropic approximation).

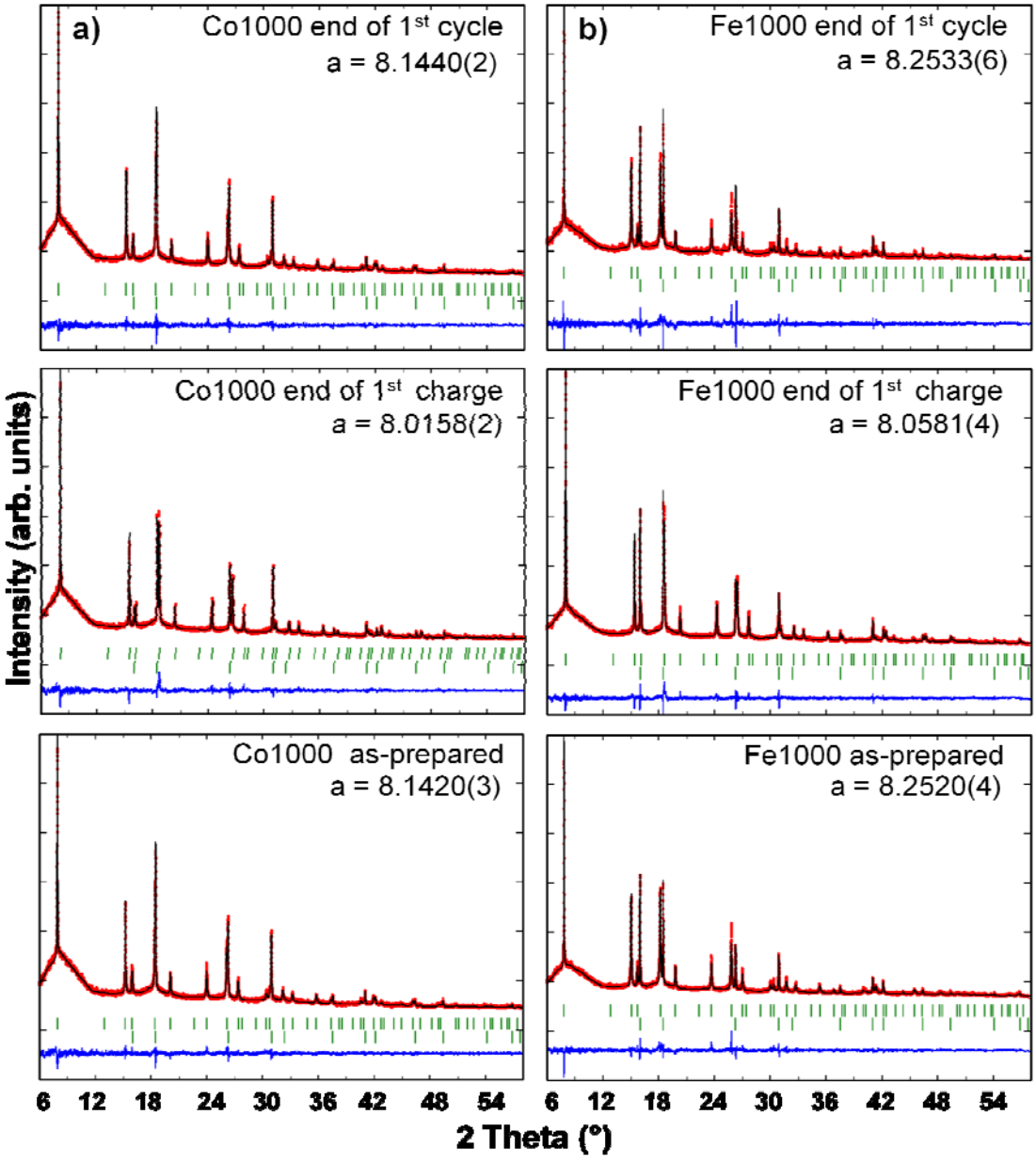

***Figure 9.2**: Rietveld refinement based on in situ synchrotron diffraction results for (a) $LiCo_{0.5}Mn_{1.5}O_4$-1000 (b) $LiFe_{0.5}Mn_{1.5}O_4$-1000 in space group $Fd\bar{3}m$ for as prepared cells, at the end of 1st charge and at the end of 1st cycle.*

A profile matching mode was used for the contributions from the aluminum current collector window, instead of a Rietveld fit as the aluminum reflections show extreme texturing and hence corresponding intensities do not agree with those from aluminum powder as expected for isotropic bulk materials.

Rietveld refinement confirmed that the prepared cell retains its structure (belongs to $Fd\bar{3}m$ space group) at the end of the charge and after cycling. The lattice parameters were found to be decreased at the end of charge in the case of both Co- and Fe-doped spinels. (see Table 9.1). The calculated shrinkage of the unit cell at the end of the first charge is 1.55% and 2.35% for $LiCo_{0.5}Mn_{1.5}O_4$-1000 and $LiFe_{0.5}Mn_{1.5}O_4$-1000, respectively. After the first cycle, the unit cell parameters were observed to be closer to the initial values, even slightly higher and it confirms the successful re-intercalation of Li^+ back to the spinel structure. The slight increase in the lattice parameters could be also an indication of some oxygen loss during full charge.

Table 9.1: *Evolution of cell constants based on in situ synchrotron diffraction, for $LiM_{0.5}Mn_{1.5}O_4$-1000 (M = Fe, Co), space group $Fd\bar{3}m$, at different stages of cycling.*

Sample	Freshly prepared cell a (Å)	End of 1st charge a (Å)	End of 1st cycle a (Å)
$LiFe_{0.5}Mn_{1.5}O_4$-1000	8.2520(4)	8.0581(4)	8.2533(6)
$LiCo_{0.5}Mn_{1.5}O_4$-1000	8.1420(3)	8.0158(2)	8.1440(3)

The structure evolutions during charge and discharge processes for both Co and Fe substituted samples are displayed in Figure 9.3a and b respectively. Selected 2θ regions; 19.8° ≤2θ ≤ 24.8° for $LiCo_{0.5}Mn_{1.5}O_4$-1000 and 19.6° ≤2θ ≤ 24.5° for $LiFe_{0.5}Mn_{1.5}O_4$-1000 of the above measurements are displayed in Figure 9.4a and b.

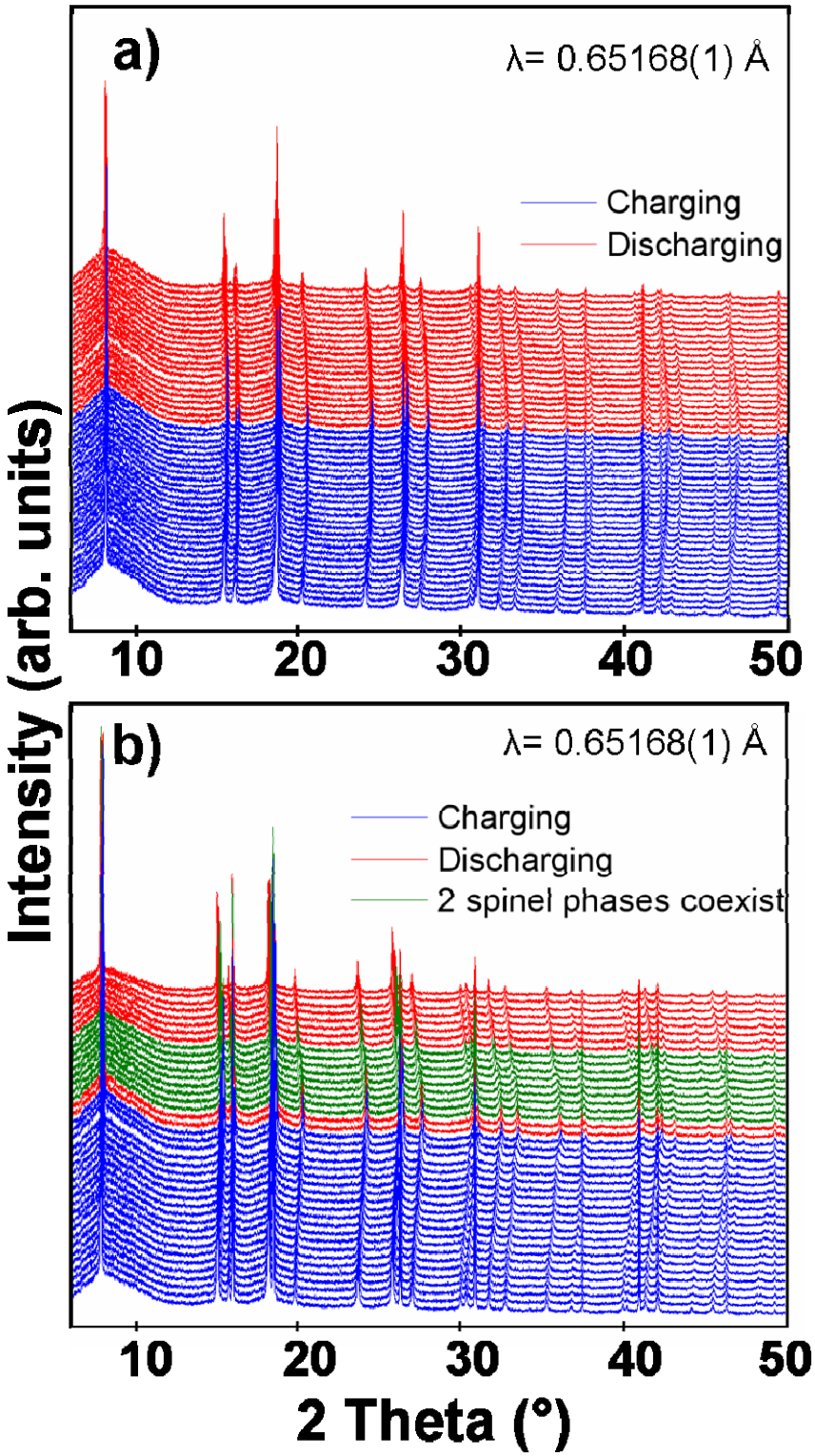

***Figure 9.3**: in situ synchrotron diffraction results showing different regions during the 1st cycle of (a) $LiCo_{0.5}Mn_{1.5}O_4$-1000, (b) $LiFe_{0.5}Mn_{1.5}O_4$-1000, where blue lines and red lines represent charging and discharging respectively. The green lines shown in (b) indicate the regions where the co-existence of two spinel phases was observed.*

The evolution of the synchrotron diffraction patterns of $LiCo_{0.5}Mn_{1.5}O_4$-1000 during cycling is characteristic for solid-solution mechanism of lithiation-delithiation. Each diffraction pattern reflects the presence of one spinel phase at different stages of charge-discharge. The shifting of the reflections to higher and lower 2 theta values indicates the continuous shrinkage and expansion of the unit cell during delithiation and lithium intercalation, respectively.

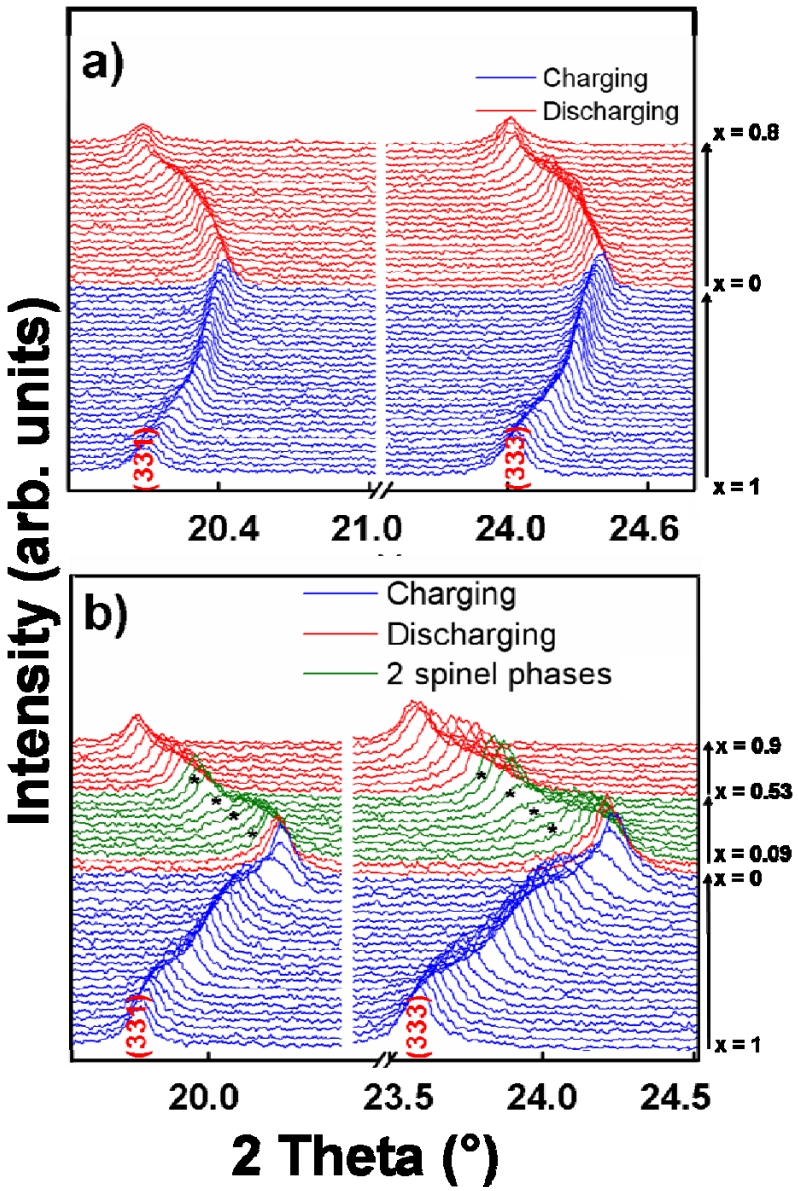

***Figure 9.4**: The selected 2θ regions of the total 47 and 43 in situ synchrotron diffraction patterns of (a) $LiCo_{0.5}Mn_{1.5}O_4$-1000 and (b) $LiFe_{0.5}Mn_{1.5}O_4$-1000 respectively showing the peak shifting during the 1st cycle. The diffraction peaks marked by "*" in (b) are assigned to the second spinel phase.*

In the case of $LiFe_{0.5}Mn_{1.5}O_4$-1000, the extraction of lithium proceeds via solid solution mechanism too. Upon discharge, the pronounced region ($0.09 \leq x \leq 0.53$) was observed, which corresponds to a co-existence of two spinel phases with slightly different lattice parameters. One of the diffraction patterns which shows the co-existence of two phases during discharge is shown in Figure 9.5 and the regions where the two phases co-exist are clearly visible is zoomed in.

The co-existence of the phases observed during discharge for $LiFe_{0.5}Mn_{1.5}O_4$-1000 could be attributed to a slow kinetic re-intercalation process. If the re-intercalation proceeds in an inhomogeneous manner and some particles are intercalated faster than other, the "pseudo two-phase" behavior may be observed. In this case, the diffraction pattern reflects not a co-existence of two phases with fixed cell parameters within one particle (true two-phase behavior), but the presence of particles with different degree of lithium re-insertion.

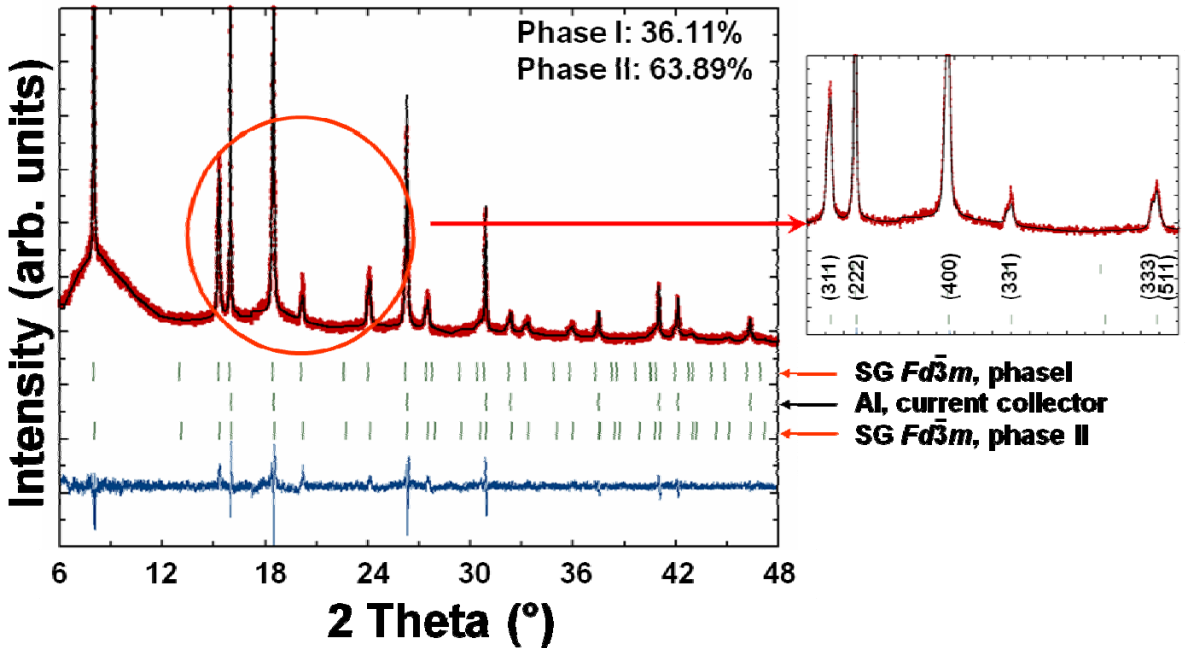

***Figure 9.5**: in situ synchrotron diffraction pattern corresponds to 0.25 moles of Li re-intercalation in $LiFe_{0.5}Mn_{1.5}O_4$-1000 where a pronounced co-existence of the two spinel phases is observed. The lattice parameters and the corresponding phase ratio are found as 8.145(2), 8.101(1) and 37(1) w/w %, 63(1) w/w % for phase I and phase II, respectively.*

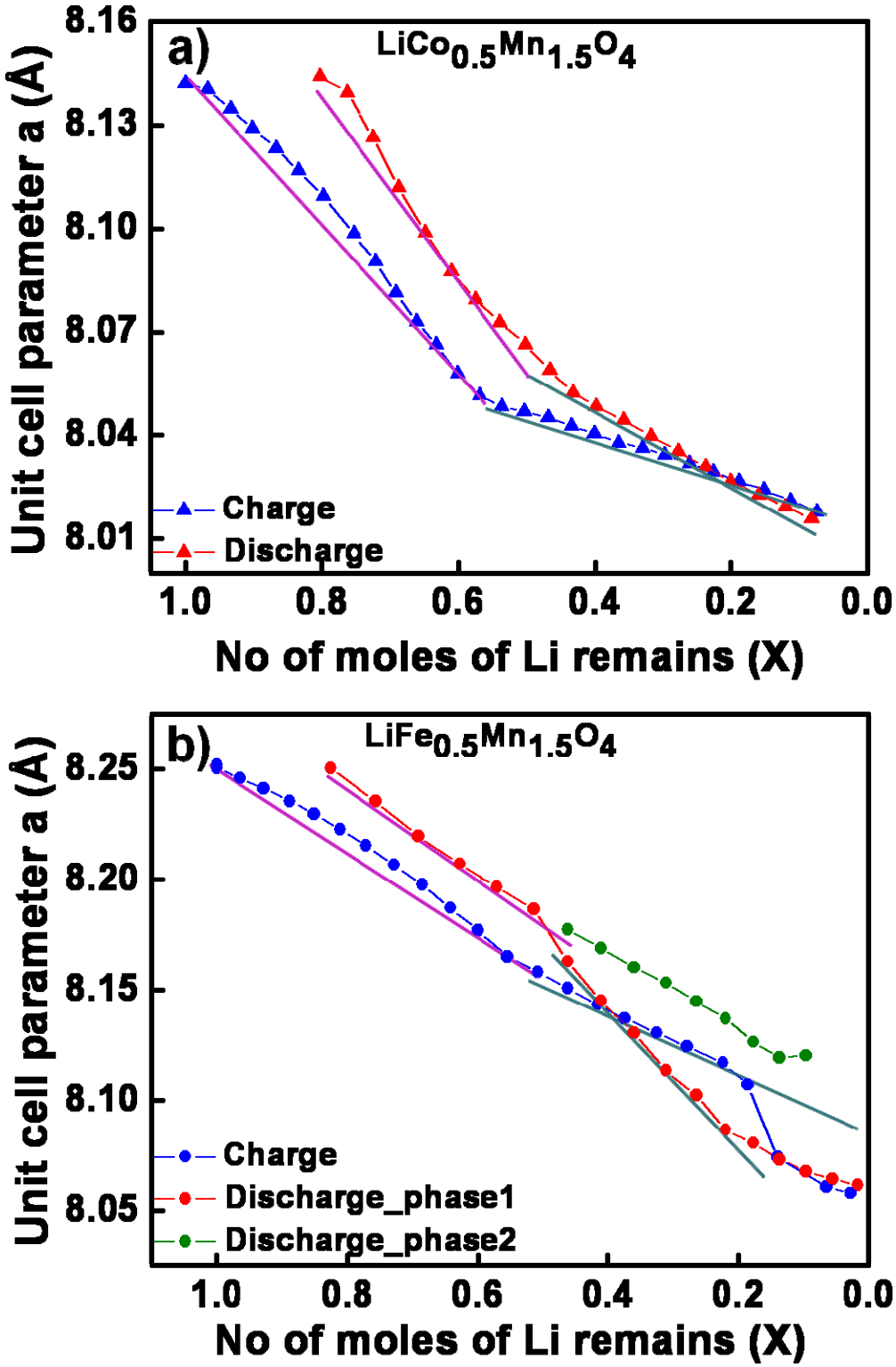

***Figure 9.6**: Lattice parameters vs. remaining number of moles of lithium during first cycle for (a) $LiCo_{0.5}Mn_{1.5}O_4$-1000 and (b) $LiFe_{0.5}Mn_{1.5}O_4$-1000. The green points in (b) represent the lattice parameters of the additional spinel phase. The different slopes are shown by different lines in the figure.*

Apart from this pseudo two-phase behavior exhibited by $LiFe_{0.5}Mn_{1.5}O_4$-1000 in the discharge region due to the kinetic hindrance, both the doped spinels were found to exhibit a solid-solution mechanism of lithium intercalation and extraction. The evolution of the lattice parameter with the extracted lithium content for $LiCo_{0.5}Mn_{1.5}O_4$-1000 and $LiFe_{0.5}Mn_{1.5}O_4$-1000 is shown in Figure 9.6a and b and its almost linear changes again support the existence of a solid-solution mechanism. There are two regions for both the Co- and Fe-doped samples, represented by the two different slopes of the curves, which may indicate a different charge compensation mechanism, not revealed by XRD. The two slopes may correspond to the Li^+ intercalation and extraction corresponds to the Mn^{3+}/Mn^{4+} and M^{3+}/M^{4+} (M = Co, Fe) electrochemical reactions.

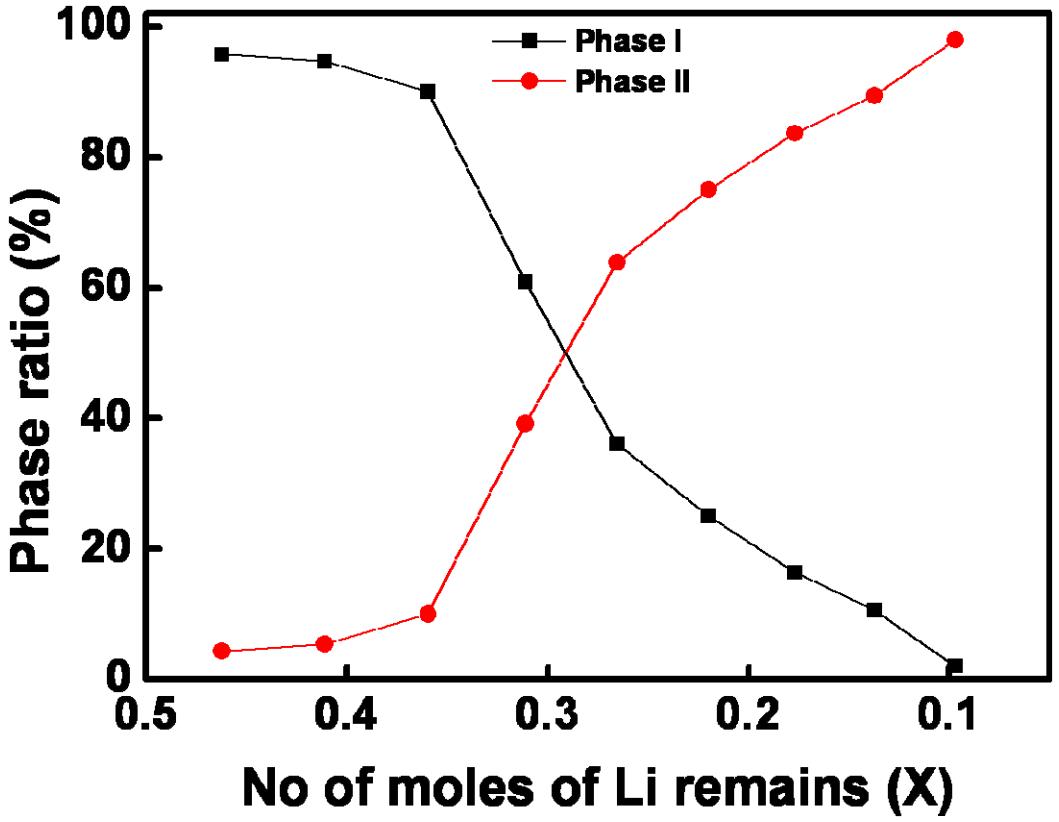

***Figure 9.7**: Phase ratio of the two phases vs. remaining number of moles of lithium during first discharge for $LiFe_{0.5}Mn_{1.5}O_4$-1000 in the region of lithium content (x), $0.09 \leq x \leq 0.53$.*

The evolution of phase ratio with the remaining number of moles of lithium during the discharge for the two-phase region of $LiFe_{0.5}Mn_{1.5}O_4$-1000 is shown in Figure 9.7.

The continuous change of the phase ratio in this region additionally proves that this two-phase co-existence is not an artifact, which may result from the *in situ* measurements such as the presence of a part of the electrode as inactive during the measurement.

Chapter 10
Metal dissolution in the electrolyte for $LiM_{0.5}Mn_{1.5}O_4$ (*M* = Fe, Co, Ni)

One of the major drawbacks associated with the high-voltage cathode materials is found to be electrolyte decomposition, as a result of thermodynamic instability of usual battery electrolytes at the voltages higher than 4 V vs. Li/Li^+. The irreversible reaction of the electrolyte with the positive electrode in the charged state may also occur. This problem is more pronounced with increased cycle number at elevated temperatures (above 50°C) [**Guyomard 1995**]. This can be solved either by developing a new electrolyte which is more stable than the conventional electrolytes or by optimizing the cathode materials, so that their stability with the conventional electrolyte gets enhanced. The optimization of cathode materials may involve several methods like increasing the particle size and hence by reducing the surface reactions, reduction of end-of-charge voltage etc. Out of these, increasing the particle size, with improved electrochemical performance was already achieved for $LiNi_{0.5}Mn_{1.5}O_4$ by increasing the synthesis temperature, close to 1000°C [**Ariyoshi 2003**].

Another major drawback associated with the Mn-based high-voltage cathode materials is found to be Mn and other transition metal dissolution in the electrolyte. This process is attributed to the presence of slightly acidic species in the electrolyte (HF) due to hydrolysis reaction of conducting salt with the traces of H_2O. According to Thackerey et al., the dissolution of manganese-based spinels occurs on extremely lithiated particles $Li_{1+x}Mn_2O_4$ (Mn oxidation state <3.5) [**Thackeray 1997**]. Here, we studied the dissolution of mixed spinels in the lithiated and delithiated state to clarify whether this process can contribute to the capacity fading upon cycling in 5 V region.

10.1 Procedure

To perform a detailed investigation of the metal dissolution, dedicated experiments were carried out. First, four pellet cathodes were prepared, (about 80 mg, 13 mm diameter) each for all the three materials with the method described in section 6.4, chapter 6. The prepared cathodes were then divided into two sets (two cathodes in each set), lithiated and delithiated. The lithiated cathodes were dried at 120°C for 24 h to remove any traces of water and weighed inside the glove-box before use. The delithiated cathodes were prepared by charging them at a rate of C/20 and with a voltage range 3.5 - 5.1 V for $LiNi_{0.5}Mn_{1.5}O_4$-1000 and 3.5 - 5.3 V for $LiFe_{0.5}Mn_{1.5}O_4$-1000 and $LiCo_{0.5}Mn_{1.5}O_4$-1000. After charging, the cells were disassembled in the argon-box and the cathodes were taken out and washed three times with DMC to remove any electrolyte residue. The washed cathodes were dried in the vacuum chamber of the argon box for 2 - 3 days. The lithiated and the delithiated cathode sets were then analyzed with XRD in Debye-Scherrer mode using capillaries and again divided into two sets, each set containing one cathode, to conduct the electrolyte contact experiments at RT and 55°C respectively. Hereafter these sample sets will be referred as "Li$M_{0.5}Mn_{1.5}O_4$-1000 (M = Fe, Co, Ni)–lithiated/delithiated-RT/55". In order to perform the metal dissolution with electrolyte contact, 3 mL of the electrolyte (1M $LiPF_6$ in EC: DMC, 1:2) was taken in aluminum bottles. The cathodes were placed inside the aluminum bottles so that they were completely dipped in the electrolyte solution and the bottles were sealed tightly and kept at RT and 55°C. 55°C experiments were specially carried out, on a hot plate in a sand bath, previously calibrated, which was equipped with a temperature sensor, in order to note any fluctuations and to adjust it. In both experiments, the set up was kept for 30 days, undisturbed, inside the argon-box. At the end of the experiments, the remaining electrolyte solutions were analyzed with ICP-OES for the presence of Mn and other transition metal M (Fe, Co or Ni). In order to perform the elemental analysis, the remaining electrolyte solution after the experiment was filtered to avoid the presence of any original material and dissolved in nitric acid so as to oxidize its organic part. The whole solution was used for the analysis and measured three times. At least three wavelengths were tried per element and an average of the values is reported. The residual pellets were examined with XRD for any structural changes, and compared with the results before experiments. The lithiated cathode pellets after RT and 55°C electrolyte contact experiments were also used to characterize their electrochemical

performance in order to do a comparison with the aged and fresh electrode materials. The results are discussed in the following sections.

10.1.1 Electrochemical delithiation

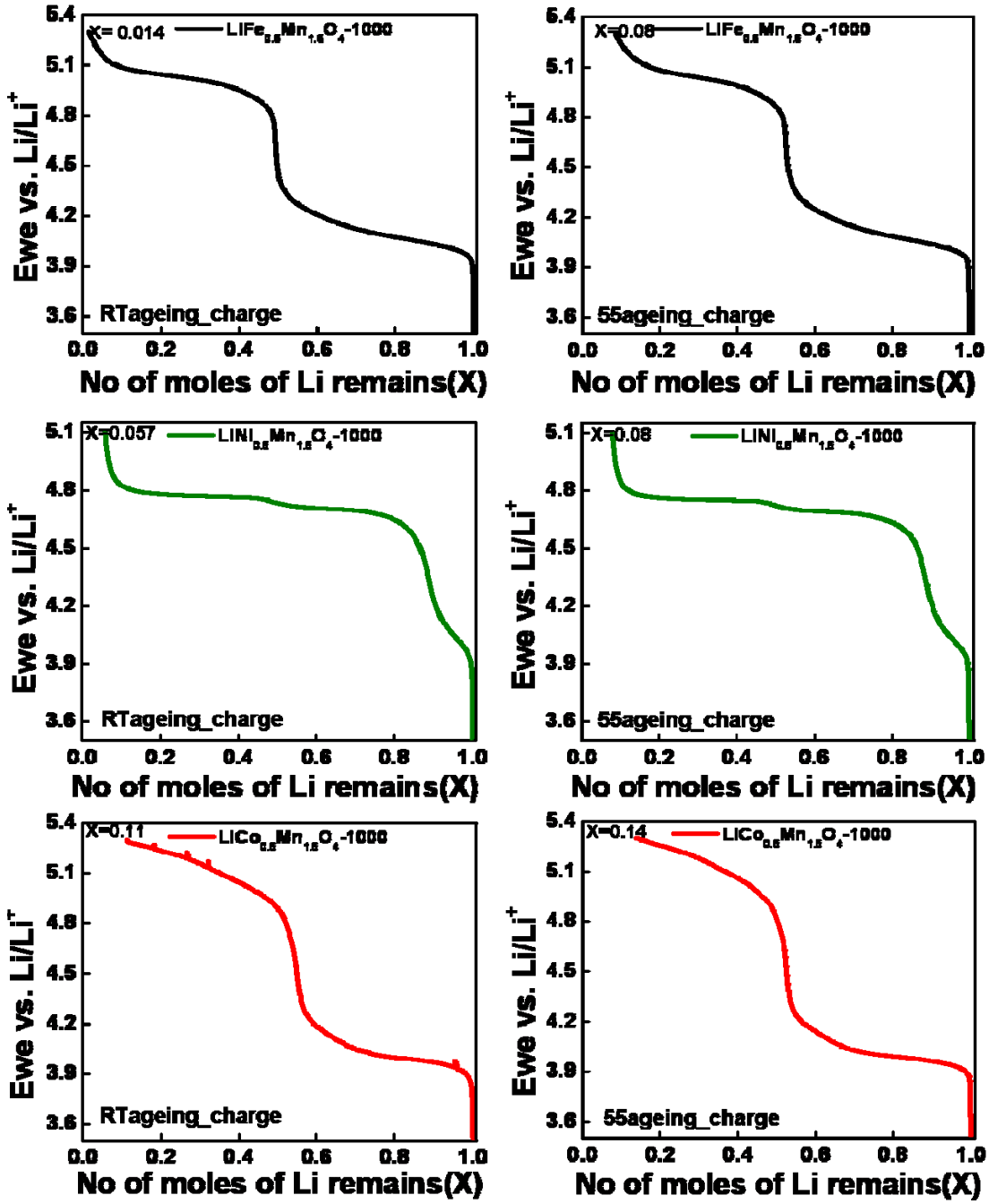

***Figure 10.1**: Voltage vs. number of moles of lithium remains plot, showing the electrochemical delithiation of samples used for RT and 55°C electrolyte contact experiments.*

The electrochemical delithiation of each samples led to a lithium residue of 0.05 ($LiNi_{0.5}Mn_{1.5}O_4$-1000), 0.11 ($LiCo_{0.5}Mn_{1.5}O_4$-1000), and 0.014 ($LiFe_{0.5}Mn_{1.5}O_4$-1000) moles for the samples used for the RT ageing and 0.08 ($LiNi_{0.5}Mn_{1.5}O_4$-1000), 0.14 ($LiCo_{0.5}Mn_{1.5}O_4$-1000) and 0.08 ($LiFe_{0.5}Mn_{1.5}O_4$-1000) moles for the samples used for the 55°C ageing (see Figure 10.1). The amount of lithium extracted was calculated from the amount of electricity passed through the electrochemical cell. The values of the lattice parameters for the as prepared samples and for the samples after the electrochemical delithiation and the shrinkage of unit cell for the preliminary measurement, as calculated by Rietveld refinement, are shown in Table 10.1. The corresponding XRD patterns are displayed in Figure 10.2.

Table 10.1: *The cubic lattice parameters "a" for $LiM_{0.5}Mn_{1.5}O_4$-1000-lithiated and $LiM_{0.5}Mn_{1.5}O_4$-1000-delithiated (M=Fe, Co, Ni) samples and the unit cell shrinkage ($\Delta a/a$) after delithiation. The two spinel phases obtained for $LiNi_{0.5}Mn_{1.5}O_4$-1000-charged samples are given, separated by "/" and the corresponding shrinkage is shown.*

M in $LiM_{0.5}Mn_{1.5}O_4$	a/ Å (as prepared)	a/ Å (charged)	Δa/a (%)
Fe	8.2705(2)	8.0894(6)	2.19
Co	8.1632(3)	8.0283(5)	1.65
Ni	8.1955(4)	8.109(2)/ 8.0105(4)	1.05/2.26

The $LiM_{0.5}Mn_{1.5}O_4$-1000 (M = Fe, Co) samples showed single phase, face centred cubic crystal structure, that belongs to the $Fd\bar{3}m$ space group in the lithiated as well as delithiated states whereas the $LiNi_{0.5}Mn_{1.5}O_4$-1000 samples showed a second phase in the lithiated state which could be assigned to $Li_xNi_{1-x}O$ with an $Fm\bar{3}m$ space group. In the delithiated state the Ni-doped spinel indeed showed three phases; two spinel phases with different lattice parameters, which would illustrate a different extent of lithium extraction and the third phase which is again $Li_xNi_{1-x}O$ with an $Fm\bar{3}m$ space group.

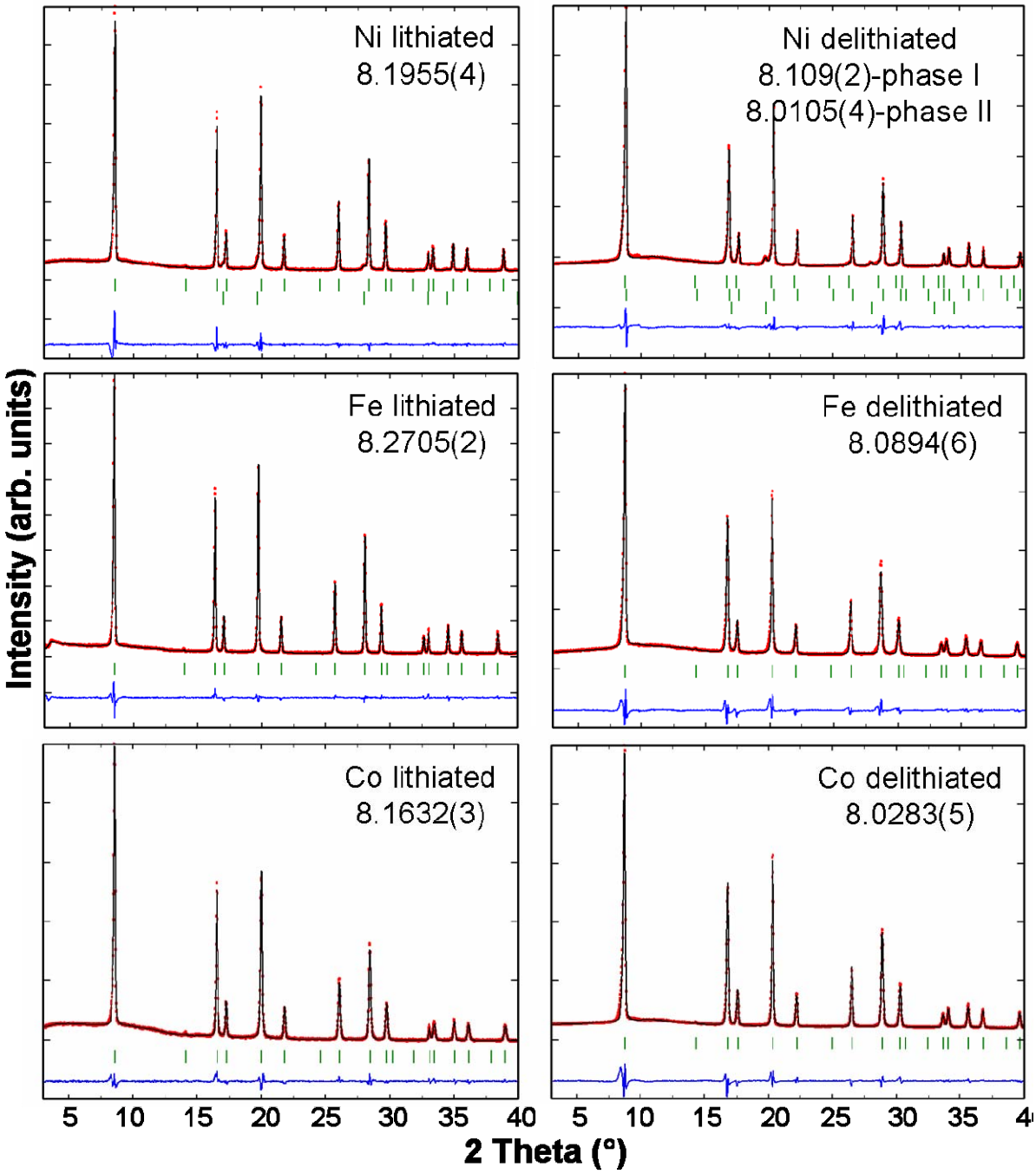

***Figure 10.2**: RT XRD patterns obtained for $LiM_{0.5}Mn_{1.5}O_4$-1000 (M = Fe, Co, Ni) before (left) and after (right) electrochemical delithiation. The corresponding lattice parameters are given in the inset of each figure. The last line of reflection marks in the $LiNi_{0.5}Mn_{1.5}O_4$-1000 samples corresponds to the $Li_xNi_{1-x}O$ phase ($Fm\bar{3}m$ space group).*

10.2 Metal dissolution studies

10.2.1 Chemical analysis after metal dissolution studies

Table 10.2: *The results of ICP-OES analysis of the electrolyte solution for presence of elements Mn, Fe, Co and Ni after the metal dissolution experiments. The values are shown in µg /3mL.*

Li$M_{0.5}Mn_{1.5}O_4$-1000 (M = Fe, Co, Ni)–lithiated-RT				
M in Li$M_{0.5}Mn_{1.5}O_4$	Mn (µg)	Fe (µg)	Co (µg)	Ni (µg)
Fe	16.23	< 0.1		
Co	20.19		< 0.5	
Ni	9.27			< 0.1

Li$M_{0.5}Mn_{1.5}O_4$-1000 (M = Fe, Co, Ni)–delithiated-RT				
M in Li$M_{0.5}Mn_{1.5}O_4$	Mn (µg)	Fe (µg)	Co (µg)	Ni (µg)
Fe	43.07	1.57		
Co	297.8		86.6	
Ni	123.03			37.31

Li$M_{0.5}Mn_{1.5}O_4$-1000 (M = Fe, Co, Ni)–lithiated-55				
M in Li$M_{0.5}Mn_{1.5}O_4$	Mn (µg)	Fe (µg)	Co (µg)	Ni (µg)
Fe	44.00	1.14		
Co	92.40		1.34	
Ni	75.90			1.13

Li$M_{0.5}Mn_{1.5}O_4$-1000 (M = Fe, Co, Ni)–delithiated-55				
M in Li$M_{0.5}Mn_{1.5}O_4$	Mn (µg)	Fe (µg)	Co (µg)	Ni (µg)
Fe	1177.53	60.45		
Co	992.9		245.1	
Ni	1533.60			446.35

The obtained ICP-OES results for the electrolyte solution after the experiments are shown in Table 10.2. The elemental analysis was only carried out for Mn and *M* (Co, Fe, Ni) and not for lithium. The reason for omitting the analysis of lithium was that the electrolyte itself contains a lithium rich salt ($LiPF_6$) which makes the exact evaluation of this element difficult. However, lithium dissolution can be possible as the electrolyte solution is not completely saturated.

Table 10.3 displays the metal ion dissolution in percentage (%) from the structural framework of $LiM_{0.5}Mn_{1.5}O_4$-1000 (*M* = Fe, Co, Ni), so as to provide a better comparison. It is observed that the cathodes in the lithiated state in contact with the electrolyte, exhibit mainly dissolution of manganese. The second transition metal ion is found only in traces in these samples after both RT and 55°C electrolyte contact experiments. In the case of delithiated cathodes, where all the transition elements are apparently present in the tetravalent state, manganese and *M* (*M* = Fe, Co, Ni) dissolution are more pronounced than in the lithiated state. It can be attributed to the lower stability of the tetravalent oxidation state for the *M* ions in the presence of electrolyte.

Another important observation is that the metal ion dissolution is more enhanced at 55°C than at RT. When the metal dissolution of lithiated samples are compared among themselves, Co-doped spinel shows a higher percentage of dissolution both at RT and 55°C. Such a comparison is not exact for the delithiated samples as the state of charge which clearly has an influence on the metal dissolution is not exactly the same for the three materials.

Table 10.3: *Comparison of transition metal ion dissolution (%)[3] from $LiM_{0.5}Mn_{1.5}O_4$-1000 (M = Fe, Co, Ni) in different electrochemical states.*

Li$M_{0.5}Mn_{1.5}O_4$-1000 (M = Fe, Co, Ni)–lithiated-RT				
M in Li$M_{0.5}Mn_{1.5}O_4$	Metal ion dissolution (%)			
	Mn	Fe	Co	Ni
Fe	0.056	0.001		
Co	0.071		0.005	
Ni	0.031			0.001

Li$M_{0.5}Mn_{1.5}O_4$-1000 (M = Fe, Co, Ni)–delithiated-RT				
M in Li$M_{0.5}Mn_{1.5}O_4$	Metal ion dissolution (%)			
	Mn	Fe	Co	Ni
Fe	0.175	0.019		
Co	1.188		0.966	
Ni	0.459			0.391

Li$M_{0.5}Mn_{1.5}O_4$-1000 (M = Fe, Co, Ni)–lithiated-55				
M in Li$M_{0.5}Mn_{1.5}O_4$	Metal ion dissolution (%)			
	Mn	Fe	Co	Ni
Fe	0.150	0.011		
Co	0.320		0.013	
Ni	0.270			0.011

Li$M_{0.5}Mn_{1.5}O_4$-1000 (M = Fe, Co, Ni)–delithiated-55				
M in Li$M_{0.5}Mn_{1.5}O_4$	Metal ion dissolution (%)			
	Mn	Fe	Co	Ni
Fe	4.958	0.751		
Co	3.576		2.469	
Ni	5.814			4.752

[3] % dissolution based on weight of the corresponding metal ion.

10.2.2 Structural analysis after metal dissolution studies

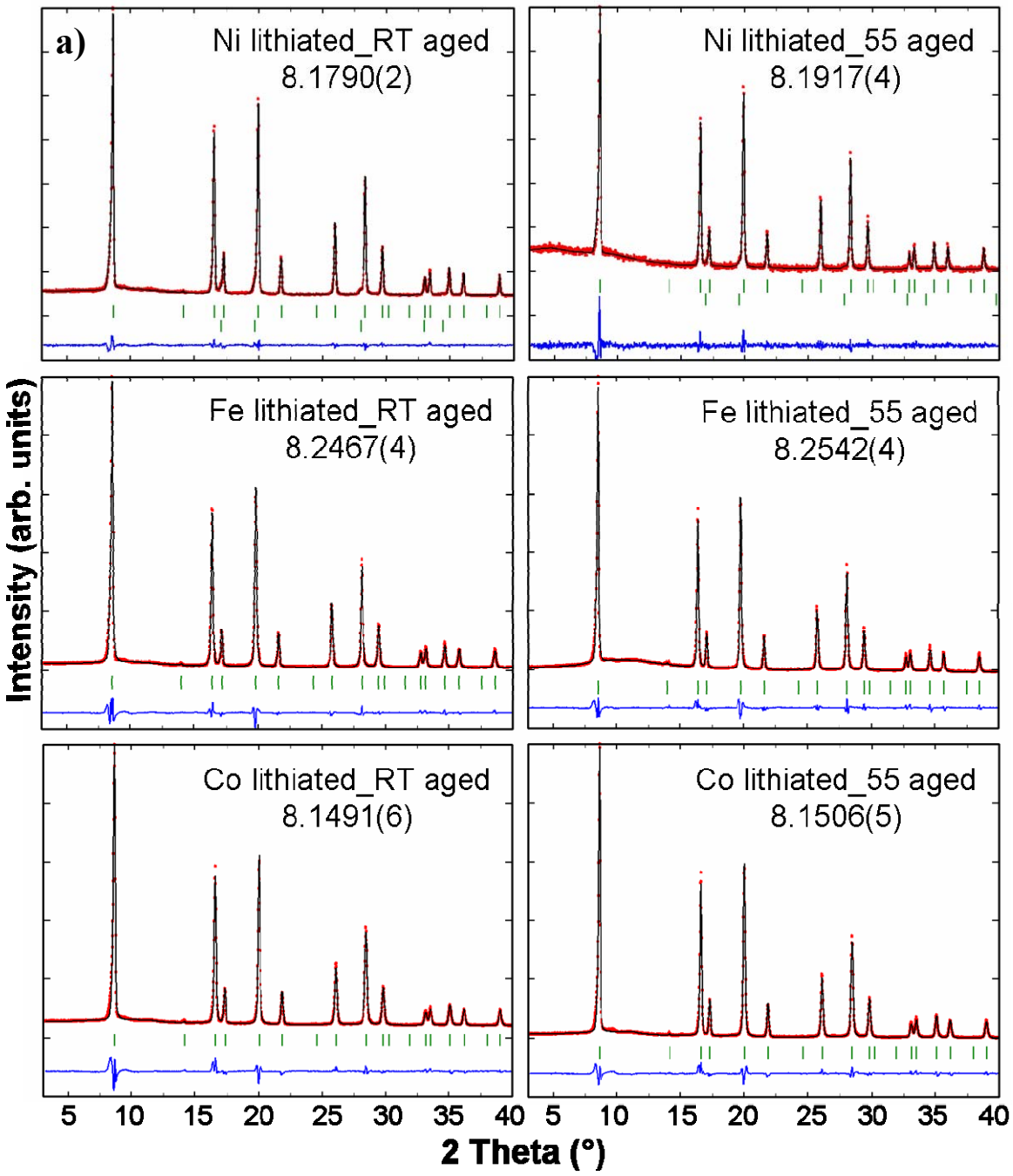

***Figure 10.3a**: RT XRD patterns obtained for lithiated $LiM_{0.5}Mn_{1.5}O_4$-1000 (M = Fe, Co, Ni) samples after electrolyte contact experiments at RT and 55°C. The corresponding lattice parameters are given in the inset of each figure. The last line of reflection marks in the $LiNi_{0.5}Mn_{1.5}O_4$-1000 samples corresponds to the $Li_xNi_{1-x}O$ phase ($Fm\bar{3}m$ space group).*

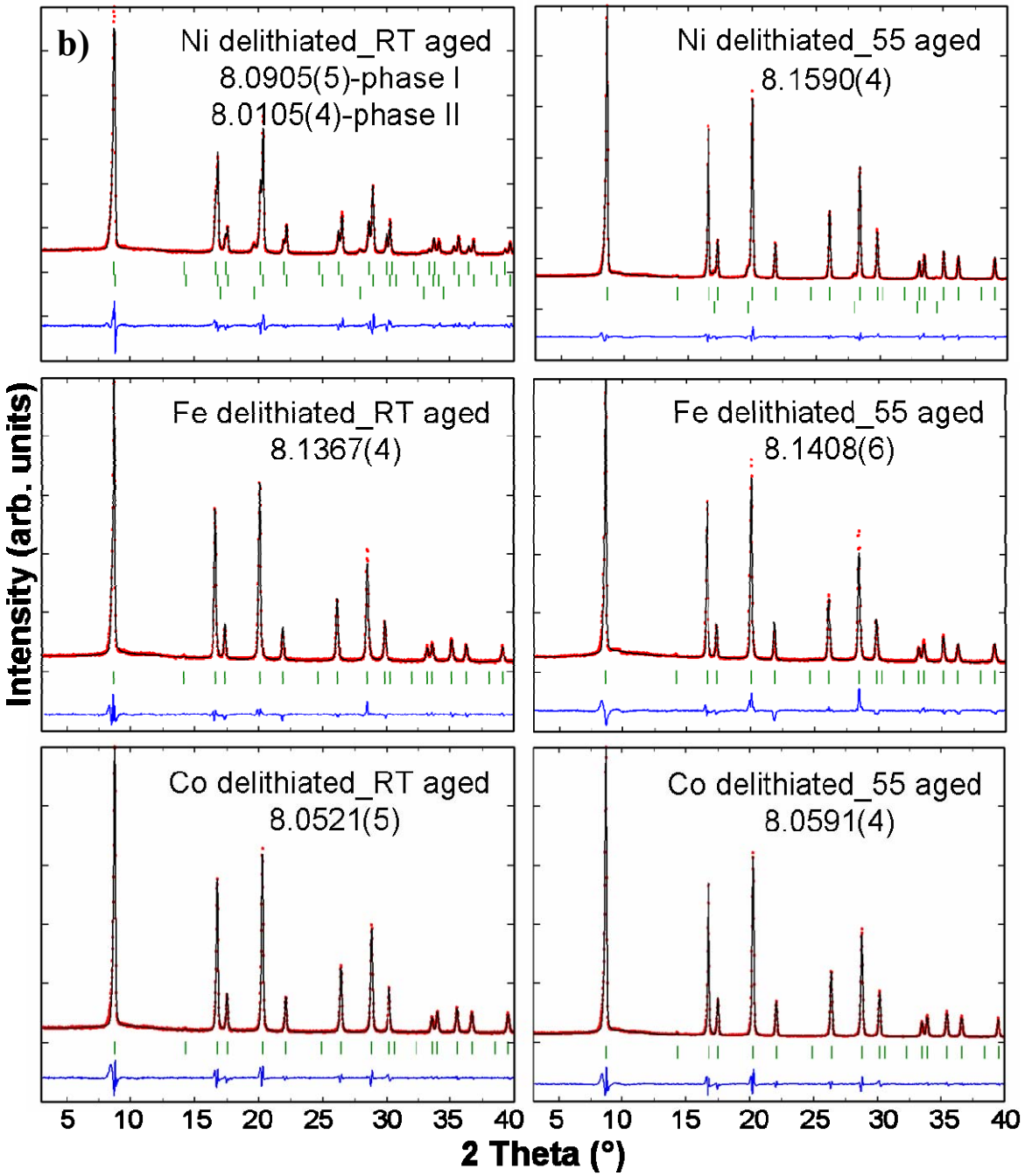

***Figure 10.3 b**: RT XRD patterns obtained for delithiated $LiM_{0.5}Mn_{1.5}O_4$-1000 (M = Fe, Co, Ni) after electrolyte contact experiments at RT and 55°C. The corresponding lattice parameters are given in the inset of each figure. The last line of reflection marks in the $LiNi_{0.5}Mn_{1.5}O_4$-1000 samples corresponds to the $Li_xNi_{1-x}O$ phase ($Fm\bar{3}m$ space group).*

The obtained pellets after the experiments were washed several times with DMC, to remove any soluble decomposition products from the electrolyte, ground and

subjected to X-ray diffraction in Debye-Scherrer mode using capillaries. Figure 10.3 shows a comparison of the XRD patterns after the ageing experiments in the case of Fe-, Co- and Ni-doped samples. The unit cell parameters obtained for each batch of materials are given in the inset of each diffraction pattern. It was observed that after the ageing experiment, the structure of the Li$M_{0.5}Mn_{1.5}O_4$-1000 (M = Fe, Co, Ni) samples remains the same as fresh cathodes for the delithiated and lithiated samples. No additional phases in comparison with those observed before the ageing experiments were visible in the case of all samples (see Figure 10.3a and b).

10.2.3 Electrochemical characterization of the aged cathodes

As seen from the ICP-OES and the XRD analysis, the prolonged storage of the positive cathodes in electrolyte contact results in metal dissolution from the structure framework. It was important to test the impact of this phenomenon on the electrochemical behavior of the material. In order to study this, the RT and 55°C aged electrodes in the lithiated state were subjected to galvanostatic cycling with a rate of C/2. For this, the aged pellets were washed, dried in the vacuum chamber of the argon-box, ground again and a part was pressed at 8 tons in an aluminum mesh and dried at 110°C for 1 h in vacuum to remove the traces of DMC. The prepared cathodes were then used to assemble electrochemical cells in the argon-box with the usual procedure discussed before. The results are displayed in Figure 10.4.

For the RT aged samples, the initial capacities are close to the values obtained for the fresh materials as discussed in chapter 8, section 2 except for the slightly higher capacity of $LiFe_{0.5}Mn_{1.5}O_4$-1000 in the first cycle. However, the capacity fading is more pronounced in comparison with the fresh samples. The 55°C aged Fe and Ni substituted samples exhibited lower initial capacity than the fresh and RT aged cathodes whereas the Co sample showed initial capacity close to that of the fresh sample. In addition, higher capacity retention was found in the case of Fe and Ni substituted samples than the RT treated samples although the Co-doped sample exhibited an increased capacity fading. This difference in the electrochemical behavior could be attributed to the difference in the surface layer. The formation of a protective layer on the surface for the $LiFe_{0.5}Mn_{1.5}O_4$-1000 and $LiNi_{0.5}Mn_{1.5}O_4$-1000 samples, especially at 55°C, could be a reason for this special behavior which may not form for the $LiCo_{0.5}Mn_{1.5}O_4$-1000 sample.

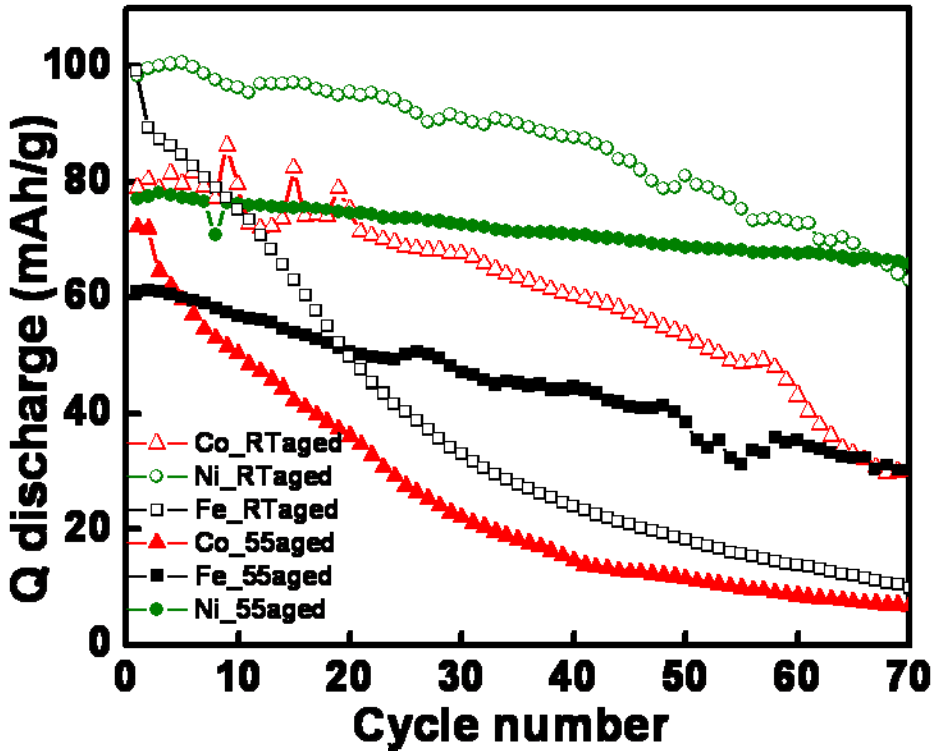

Figure 10.4: *Cycle number vs. capacity plots for $LiM_{0.5}Mn_{1.5}O_4$-1000 (M=Fe, Co, Ni) samples after RT and 55°C electrolyte contact experiments.*

Table 10.4: *Comparison of the initial capacity and capacity retention after 70 cycles for aged and fresh $LiM_{0.5}Mn_{1.5}O_4$-1000 (M=Fe, Co, Ni) samples. Capacity is denoted by 'Q'.*

$LiM_{0.5}Mn_{1.5}O_4$-1000 (M = Fe, Co, Ni)						
M in $LiM_{0.5}Mn_{1.5}O_4$	Fresh		RT aged		55°C aged	
	Initial Q ($mAhg^{-1}$)	% Q retention	Initial Q ($mAhg^{-1}$)	% Q retention	Initial Q ($mAhg^{-1}$)	% Q retention
Fe	89.5	59	100	10	61	49
Co	77	55	79	38	72	11
Ni	107	95	98	64	77	85

The initial capacity and capacity retention values for the fresh, RT aged and 55°C aged samples are displayed in Table 10.5.

The conclusion is that the metal ion dissolution brings out deterioration in the performance of composite cathodes with spinel active material. Hence it is necessary to think of a technique which can reduce or prevent the metal dissolution from the structure framework of these materials and here comes the application of other optimization techniques like coating the materials with inorganic oxides such as ZnO [**Sun 2002a, Sun 2002b, Sun 2003**], Al_2O_3 [**Liu 2002**], MgO [**Kweon 2000**], SiO_2 [**Zheng 2002**] etc, coating with conductive materials such as acetylene black, silver and gold [**Dominko 2001, Lim 2001, Son 2004a, Son 2004b**], surface treatments of cathodes [**Mladenov 2001**] etc. All these optimization techniques, in the case of $LiPF_6$-based electrolytes, help to reduce the metal dissolution, avoid unwanted parasitic reactions such as electrolyte decomposition of the electrode by HF, either by reducing the available surface area or by providing a protective layer on the surface. As a further step to optimization, the $LiM_{0.5}Mn_{1.5}O_4$ (M = Fe, Co, Cr) was coated with ZnO from a Zn-acetate solution and the details of the experiment and the obtained results are discussed below.

10.3 Coating with ZnO

10.3.1 Coating procedure

The coating was carried out by using a method reported by Sun et al. [**Sun 2002b**]. The coating solution was prepared by dissolving $Zn(CH_3COO)_2.H_2O$ in distilled water. Already synthesised $LiM_{0.5}Mn_{1.5}O_4$-1000 (M = Fe, Co, Ni) powders were added into the solution and thoroughly stirred for 4 h at room temperature. The amount of Zn in the solution corresponded to 1.5 wt% of the respective $LiM_{0.5}Mn_{1.5}O_4$ (M = Fe, Co, Cr) powder. Then the mixture was let to dry and after that the dried powders were preheated at 120°C in the oven and later calcined at 400°C for 1 h in air.

10.3.2 Coating characterization

All the coated products were characterized using XRD (see Figure 10.5). Rietveld refinement on the powder diffraction pattern reveals that all the samples belong to disordered spinel structure with space group $Fd\bar{3}m$. No additional reflections were visible in the case of $LiM_{0.5}Mn_{1.5}O_4$-1000 (M = Fe, Co) which illustrate the absence of any crystalline impurity after coating, while $Li_xNi_{1-x}O$ phase was found additional in

the case of coated $LiNi_{0.5}Mn_{1.5}O_4$-1000 as reported before in chapter 7 for the non-coated samples. The absence of (220) reflection in the product after coating reveals that no Zn has been inserted into the spinel crystal lattice [**Alcántara 2004**].

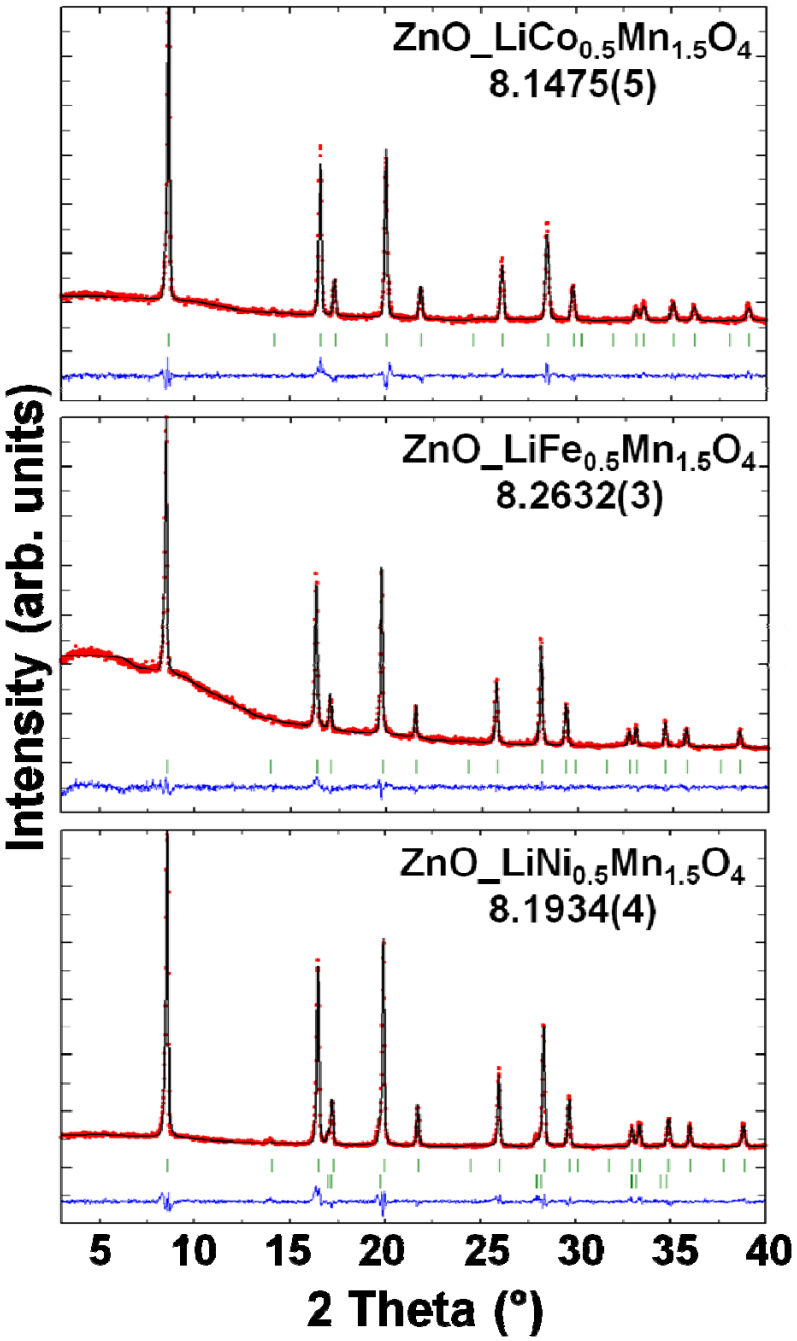

***Figure 10.5**: RT XRD patterns obtained for ZnO coated $LiM_{0.5}Mn_{1.5}O_4$-1000 (M = Fe, Co, Ni). The corresponding lattice parameters are given in the inset of each figure. The last line of reflection marks in the $LiNi_{0.5}Mn_{1.5}O_4$-1000 samples corresponds to the $Li_xNi_{1-x}O$ phase ($Fm\bar{3}m$ space group).*

The bright field TEM images were taken in the case of ZnO coated Li$M_{0.5}$Mn$_{1.5}$O$_4$-1000 (M = Fe, Co, Ni) to get a confirmation for the presence of coating. Figure 10.6 shows the TEM images for coated samples with a crystalline spinel phase covered by about 5 nm thick amorphous layer. Some parts were also observed without any coating, reveals that the coating is either not completely homogeneous or destroyed during TEM sample preparation.

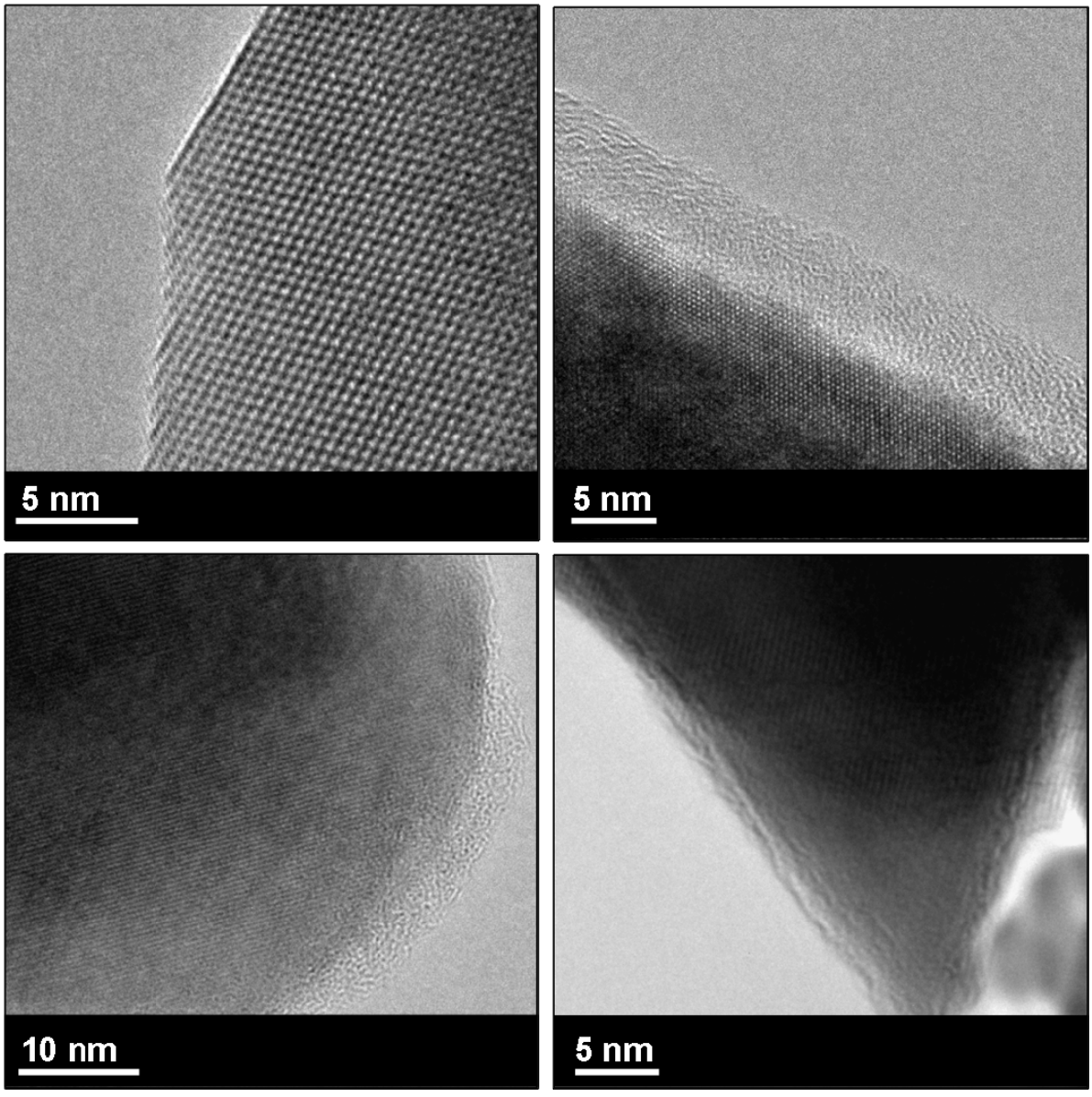

***Figure 10.6**: TEM images of the (a) uncoated part observed for $LiNi_{0.5}Mn_{1.5}O_4$-1000 particle, (b) ZnO-coated $LiNi_{0.5}Mn_{1.5}O_4$-1000 particle, (c) ZnO-coated $LiCo_{0.5}Mn_{1.5}O_4$-1000 particle and (d) ZnO-coated $LiFe_{0.5}Mn_{1.5}O_4$-1000 particle.*

To confirm that this surface amorphous layer is ZnO, XPS analyses of the coated $LiM_{0.5}Mn_{1.5}O_4$-1000 (M = Fe, Co, Ni) were performed. For this, the samples were pressed on indium foils about ~10 mm diameter with a pressure of 5 tons. The instrument was a PHI-5700-Physical Electronics with an Al Kα monochromator. C 1*s* with energy of 284.5 eV was used as a reference. The Zn 2*p* XPS spectrum obtained for the coated samples are shown in Figure 10.7. The observed binding energies of the Zn $2p_{3/2}$ was found to be 1021.2 eV which was very close to the standard value of ZnO found in literature (1021.7 eV) [**Liu 2007**]. This confirms that the coated form of Zn is ZnO and this remained on the surface of the spinel and there was no interaction with the core material. Moreover, the symmetric shape of the Zn 2*p* peak further indicates that ZnO is probably the only chemical state of Zn in these coated samples [**Liu 2007**].

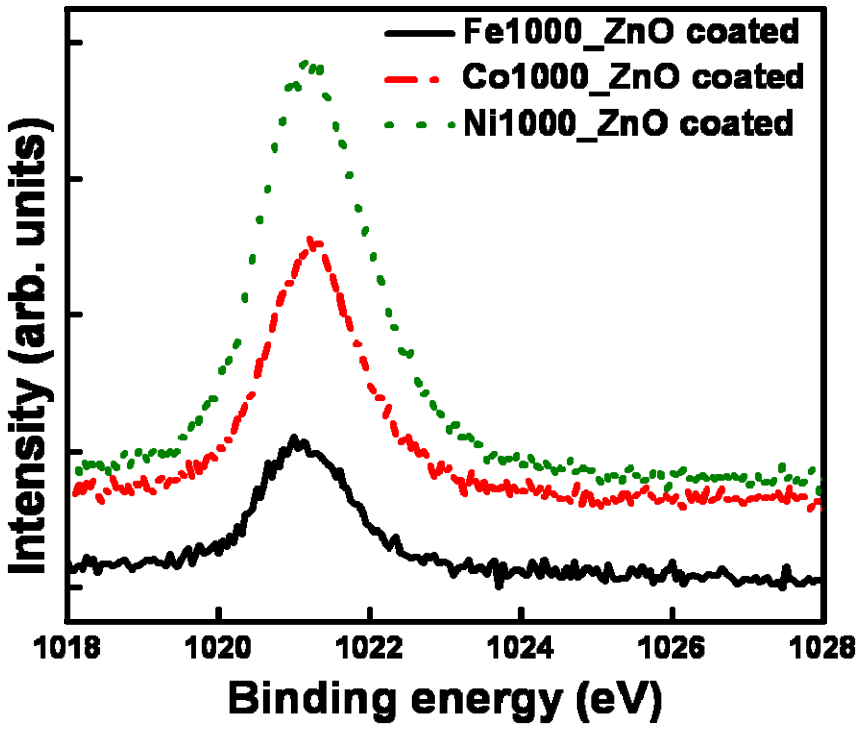

***Figure 10.7**: XPS spectrum of Zn 2p taken from the surface of ZnO-coated $LiM_{0.5}Mn_{1.5}O_4$-1000 (M = Fe, Co, Ni).*

10.3.3 Electrochemical performance

The electrochemical studies were performed with a cathode mixture of composition 80, 15, 5 wt/wt % of active material, super P carbon and PVDF 6020 respectively. The

preparation method of the cathode mixture and the cells was the same as described in chapter 6, section 6.4.

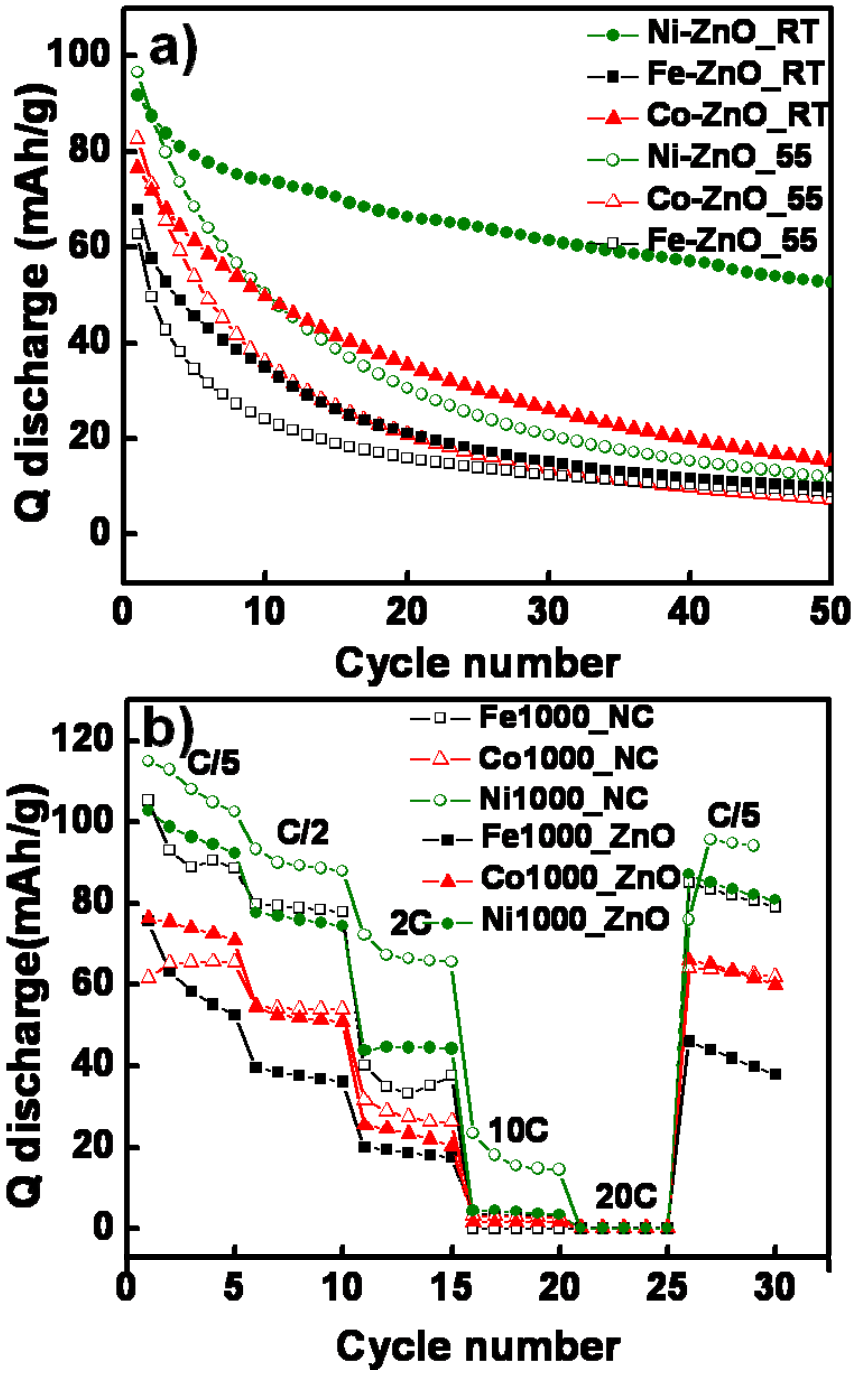

***Figure 10.8**: Cycle number vs. discharge capacity plots for ZnO-coated. $LiM_{0.5}Mn_{1.5}O_4$-1000 (M = Ni, Co, Fe), where (a) shows the cyclability and (b) shows the rate capability of these materials.*

The results of the electrochemical studies are given in Figure 10.8 and a comparison of the initial absolute capacity and capacity retention at RT and 55°C and rate capability studies is given in Table 10.6. It can be seen that there is no pronounced improvement observed in the case of any of the samples, instead the electrochemical properties are found to be deteriorated. Also no improvement was observed in the rate capability after coating (Figure 10.8b). As it was the beginning of the study, this phenomenon cannot be well explained with any solid proofs, but as a first assumption, the reason can be the catalytic effect of the ZnO on the electrolyte oxidation, when cycled at higher voltages (>5 V). An absolute explanation requires detailed surface studies of the cathodes after cycling which is outside the scope of this work.

Table 10.5: *Comparison of the initial capacity and capacity retention for ZnO-coated and non-coated $LiM_{0.5}Mn_{1.5}O_4$-1000 (M=Fe, Co, Ni) samples. Capacity is denoted by 'Q'.*

$LiM_{0.5}Mn_{1.5}O_4$-1000 (M = Fe, Co, Ni) RT cycling				
M in $LiM_{0.5}Mn_{1.5}O_4$	Non-coated		ZnO-coated	
	Initial Q ($mAhg^{-1}$)	% Q retention after 70 cycles	Initial Q ($mAhg^{-1}$)	% Q retention after 70 cycles
Fe	89.5	59	68	15
Co	77	55	76	19
Ni	107	95	91	57

$LiM_{0.5}Mn_{1.5}O_4$-1000 (M = Fe, Co, Ni) 55°C cycling				
M in $LiM_{0.5}Mn_{1.5}O_4$	Non-coated		ZnO-coated	
	Initial Q ($mAhg^{-1}$)	% Q retention after 50 cycles	Initial Q ($mAhg^{-1}$)	% Q retention after 50 cycles
Fe	83	14	63	14
Co	95	25	83	8
Ni	108	96	97	11

Chapter 11
Thermal behavior of the Li$M_{0.5}Mn_{1.5}O_4$ (M = Fe, Co, Ni) cathodes in different states of lithiation

When battery safety is taken into account, thermal stability is a major parameter of consideration. As the temperature inside an electrochemical cell increases, several exothermic reactions such as cathode decomposition and electrolyte oxidation can occur **[Wang2007]**, eventually resulting in a thermal runaway. In this chapter thermal stability of the synthesized electrode materials are investigated by combined TG-DSC and XRD analysis. The structural changes of the as-prepared (lithiated), partially charged and completely charged Li$M_{0.5}Mn_{1.5}O_4$-1000 (M = Fe, Co, Ni) cathode materials with thermal treatment under argon flow and the onset temperatures of degradation were investigated and will be discussed.

11.1 Sample preparation and characterization

11.1.1 Sample preparation

The as prepared samples were prepared by mixing 80% binder, 10% PVDF and 10% super P carbon in NMP and pressing into pellets of 13 mm diameter at 8 tons and drying at 120°C for 24 h under vacuum. Preparation of delithiated samples were accomplished by two methods; 1) chemical method using NO_2PF_6 as the oxidizing agent, 2) electrochemical delithiation. The ICP-OES analysis of the sample after chemical treatment with NO_2PF_6 showed no Li extraction for $LiNi_{0.5}Mn_{1.5}O_4$, whereas a partial delithiation took place in the case of $LiCo_{0.5}Mn_{1.5}O_4$ and $LiFe_{0.5}Mn_{1.5}O_4$. It may be attributed to the fact that the amount of Li extracted using NO_2PF_6

corresponds to the amount of Mn^{3+} present in the sample, as it may not be sufficient for the oxidation of the Co^{3+} and Fe^{3+}. Hence later the delithiated samples for thermal stability measurements were prepared electrochemically. The composite cathodes prepared for this purpose consisted of 80% binder, 10% PVDF and 10% super P carbon. The method of preparation of cathodes and electrochemical cells were the same as discussed in chapter 6, section 6.4.

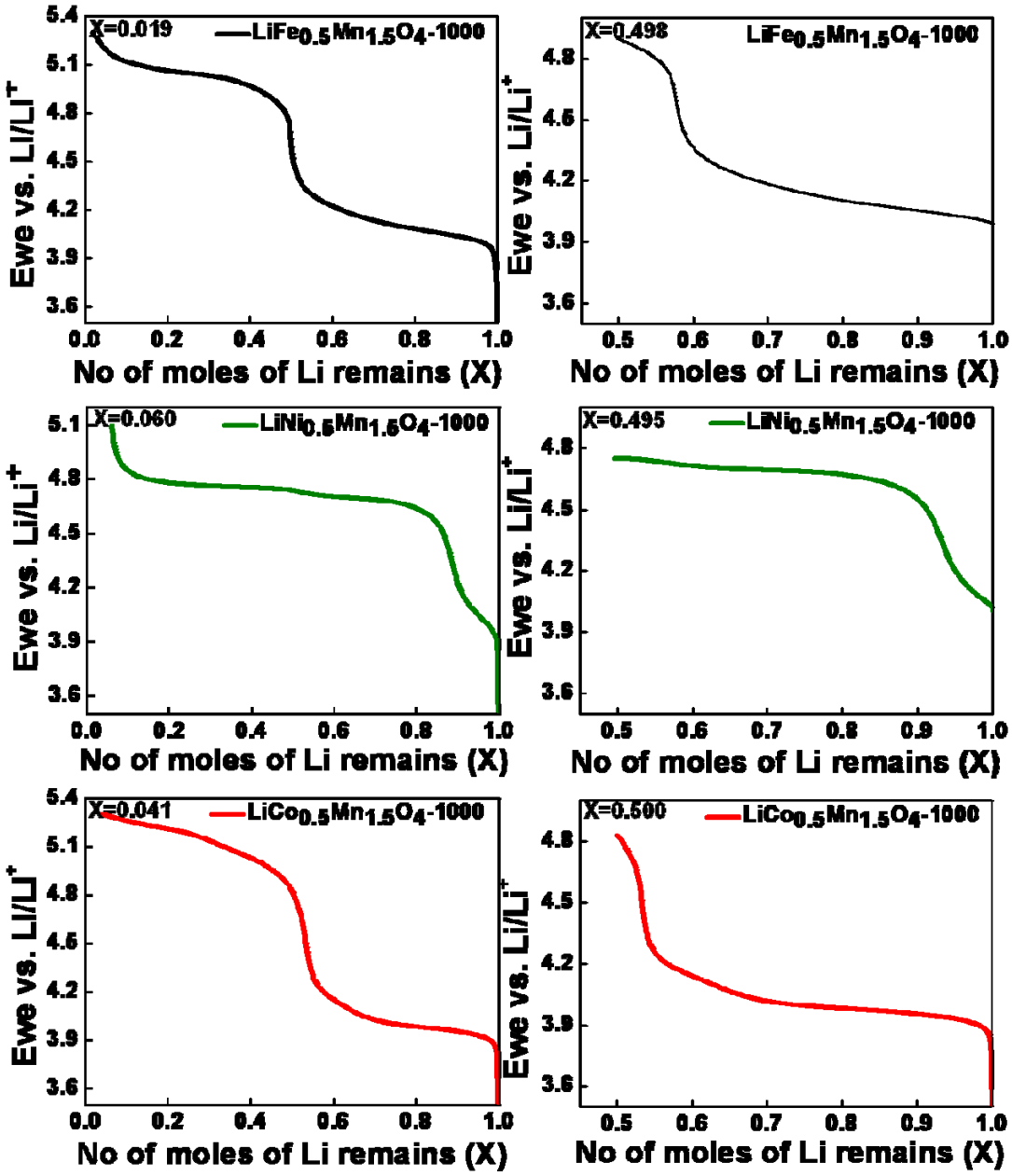

***Figure 11.1**: Voltage vs. number of moles of lithium remains plots, showing complete delithiation (left) and partial delithiation (right) of the samples used for thermal stability studies.*

A charge-discharge rate of C/20 was used and the plots obtained for partial and complete delithiation are shown in Figure 11.1. After electrochemical delithiation, the cells were disassembled in an argon-filled box, and the cathodes were washed with DMC, to remove the electrolyte residue. The washed cathodes were dried under vacuum in the chamber of the argon-box and ground before any other experiments. Thermal stability studies were carried out on the electrochemically delithiated material using a simultaneous TG-DSC analysis, at a heating rate of 10°C/minute under Argon in a Pt-Rh crucible. To elucidate more information on the active material, separate reference test was conducted only with a mixture of PVDF binder and super P carbon. X-ray powder diffraction was used to analyze the lattice contraction after charging and any structural changes after the thermal treatments. XRD data from the as prepared samples, chapter 10, section 10.1, were used as a reference as the same batch of materials were used for the experiments.

11.1.2 Structural characterization of the delithiated samples

All delithiated samples were found to belong to the $Fd\bar{3}m$ space group. The XRD patterns after Rietveld refinement are shown in Figure 11.2 and a comparison of the lattice parameters of lithiated and delithiated samples are given in Table 11.1.

Table 11.1: *The cubic lattice parameters (a) for $Li_{1-x}M_{0.5}Mn_{1.5}O_4$-1000 (M=Fe, Co, Ni) samples in the as prepared, partially charged and charged states. The two spinel phases obtained for $Li_{1-x}Ni_{0.5}Mn_{1.5}O_4$-1000-charged samples are given separated by "/" and the corresponding shrinkage is shown.*

M in $LiM_{0.5}Mn_{1.5}O_4$	As prepared a/ Å	Partially charged a/ Å	Completely charged a/ Å
Fe	8.2705(2)	8.1652(5)	8.0894(6)
Co	8.1632(3)	8.0572(6)	8.0283(5)
Ni	8.1955(4)	8.1035(4)	8.109(2)/ 8.0105(4)

This comparison shows that the unit cells shrink about 1.27%, 1.30% and 1.12% in the case of partially delithiated Fe-, Co- and Ni-doped samples respectively and 2.19

%, 1.65 % and 2.26 % (for the $Li_{1-x}Ni_{0.5}Mn_{1.5}O_4$ phase with a phase ratio 82 % wt/wt) in the case of completely delithiated Fe-, Co- and Ni-doped samples respectively, as a result of the Li extraction.

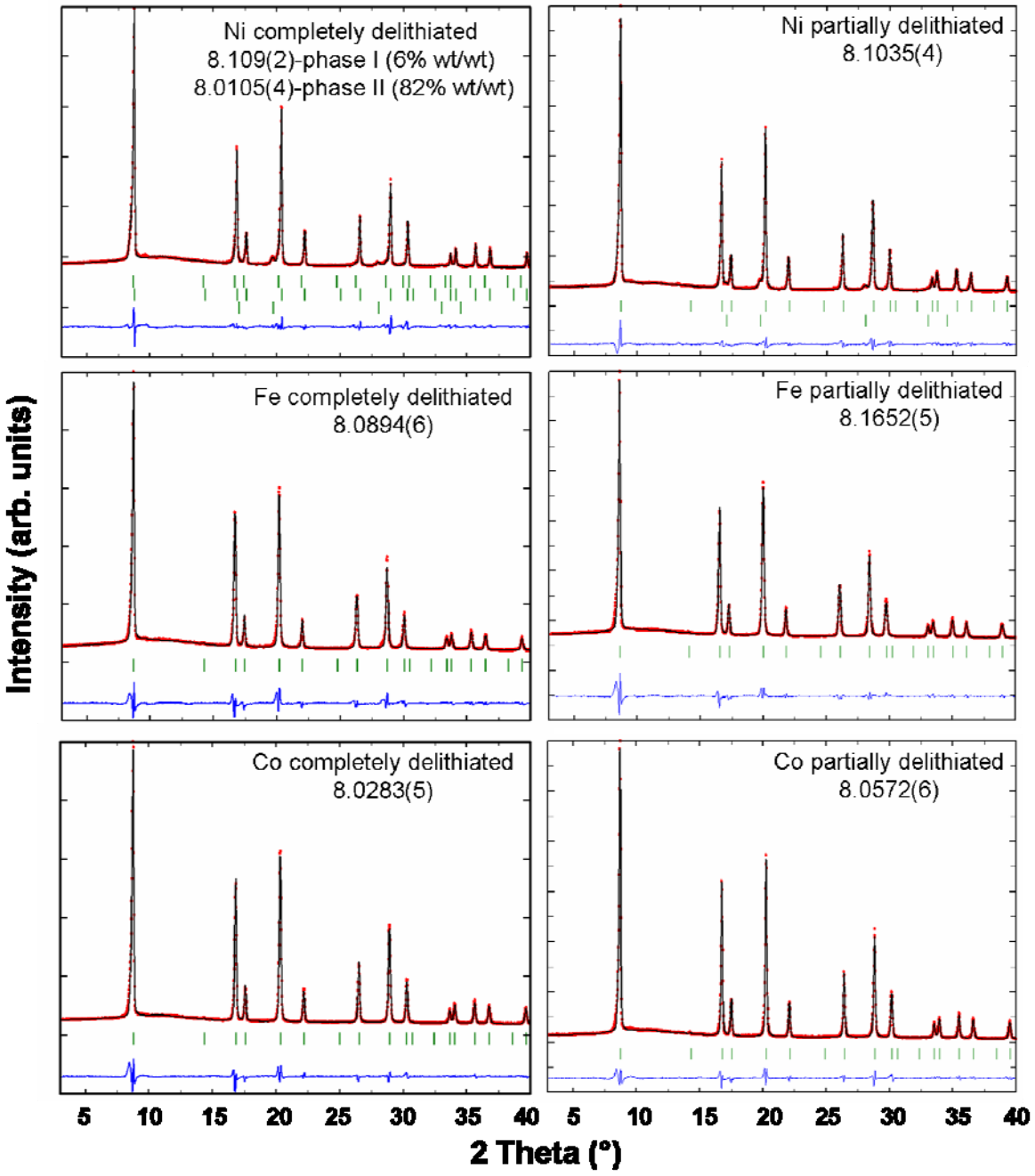

***Figure 11.2**: RT XRD patterns obtained for $LiM_{0.5}Mn_{1.5}O_4$-1000 (M = Fe, Co, Ni) after complete (left) and partial (right) electrochemical delithiation. The corresponding lattice parameters are given in the inset of each figure. The last line of reflection marks in the $LiNi_{0.5}Mn_{1.5}O_4$-1000 samples corresponds to the $Li_xNi_{1-x}O$ phase ($Fm\bar{3}m$ space group).*

11.2 Thermal stability studies

11.2.1 TG-DSC analyses

The results of the thermogravimetric analyses are shown in Figure 11.3. The thermal analysis measurement conducted for the mixture of PVDF binder with super P carbon, is shown in Figure 11.3a.

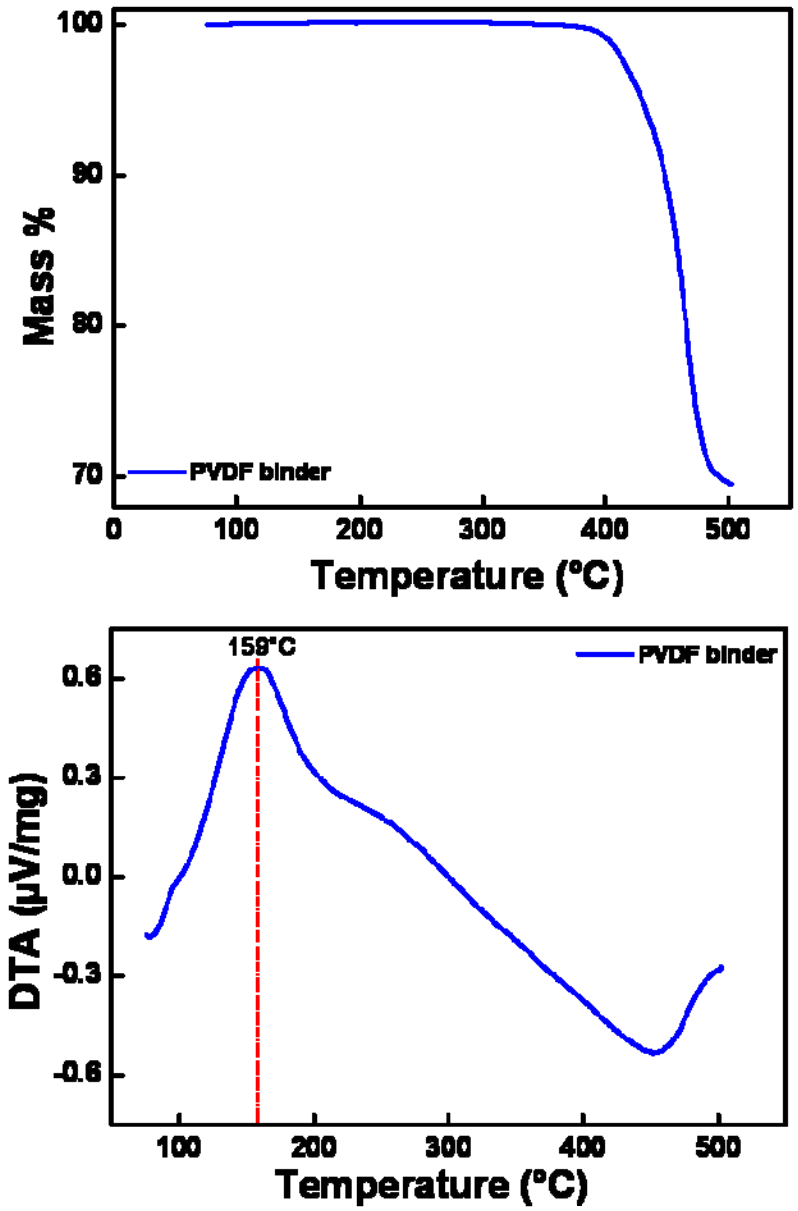

***Figure 11.3a**: TG and DTA profiles in argon at a rate of 10°C/ minute, for the mixture of PVDF binder with super P carbon.*

The maximum temperature of the thermal analysis was chosen as 500°C. It can be seen that there is an endothermic peak for the mixture of PVDF binder with super P carbon sample at ~159°C, which could be related to its melting as there was no weight change observed in the TG analysis. This value is lower than the known melting point of commercial PVDF 6020 (170°C). This endothermic peak was observed for all the samples analysed later as the samples contain 10% wt/wt of PVDF. Also it was found that the PVDF sample undergoes decomposition after 370°C, as revealed by the weight loss after this temperature in the TG analysis. Hence for the further studies, the maximum temperature was set as 350°C so to avoid any effect of the binder decomposition on the structural stability of the cathode materials. Also due to the lower sensitivity of DTA, DSC measurements were conducted simultaneously to extract more information. In the beginning of each experiment, up to 120°C, the "pseudo peaks" observed in the DSC are due to the system stabilization and can be avoided while explaining the processes.

Only <0.5% weight loss was observed until 350°C for the as-prepared Li$M_{0.5}Mn_{1.5}O_4$-1000 (M = Fe, Co, Ni) samples, which is seen as constantly increasing lines in the DSC measurements, whereas there are more pronounced weight losses for the partially and completely charged materials below 350°C.

Considering the set of partially charged samples, weight losses of 0.2%, 0.4% and 0.4% were observed below 200°C for Fe-, Co- and Ni-doped samples respectively which may be attributed to the loss of $LiPF_6$ or other contaminants which can not be removed by washing **[Wang 2007]**. Starting from ~200°C there is a weight loss, which continues up to 300°C, of 0.7%, 1.6% and 2.4% for partially charged Fe-, Co- and Ni-doped samples respectively. The weight losses are appearing as broad exothermic DSC signals for Co (starting from 200°C, continuing up to 350°C, proceeding via two close steps) and Ni (between 200°C and 270°C) whereas no signals are observed for the Fe-doped sample. This difference may be due to the difference in the degradation mechanism among the three samples. Until 350°C, weight losses of 1.3%, 5.2% and 3.7% were observed which appears as a continuation of the exothermic signals from 200°C in DSC for Fe- and Ni- doped samples and a new signal starting from close to 350°C for the Co-doped sample.

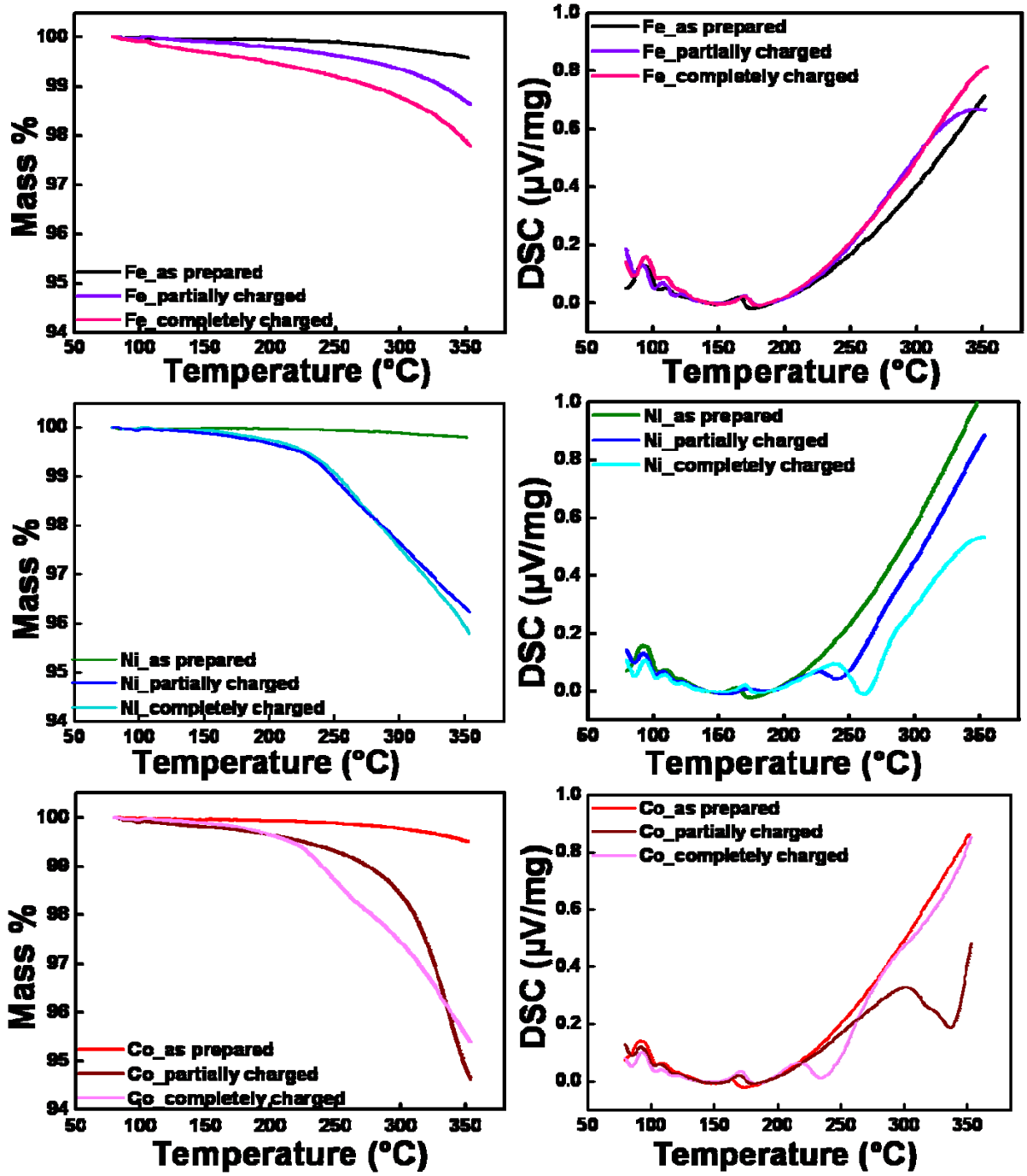

***Figure 11.3b**: TG (left) and DSC (right) profiles in argon at a rate of 10°C/ minute, for $LiM_{0.5}Mn_{1.5}O_4$-1000 (M = Fe, Co, Ni) samples after complete and partial electrochemical delithiation.*

In the case of completely charged samples, $LiFe_{0.5}Mn_{1.5}O_4$-1000 showed the starting of a mass loss slowly from 200°C as in the previous cases. Only a mass loss of 0.5% was observed below 200°C which could be due to the degradation of any electrolyte

residue. 1.2% of the mass is lost between 200°C and 300°C and a mass loss of 2.1% occurs between 300°C and 350°C, without any corresponding DSC signals. For $LiCo_{0.5}Mn_{1.5}O_4$-1000, instead of a continuous gradual mass change observed for partially charged samples, a pronounced faster mass loss is visible from >200°C which goes up to 350°C in two steps (2.6% between 200-300°C and 4.4% until 350°C) and an exothermic signal corresponding to the first step was observed in DSC between 200°C and 250°C which could be attributed to a phase change. For the $LiNi_{0.5}Mn_{1.5}O_4$-1000 samples, the TG curves displaying the mass loss are similar to that of partially charged sample and the pronounced mass loss starts at ~220°C. The mass losses are 0.4% before 200°C, 2.5% until 300°C and 4% until 350°C. The DSC signal appears between 200-260°C and is broader than that of the partially charged samples and the maxima is shifted to higher temperature (shift of ~20°C), indicating more stability than the partially charged material and its exothermic nature could be attributed to a phase change.

From the above observations it can be concluded that the thermal stability of the Li$M_{0.5}Mn_{1.5}O_4$-1000 (M = Fe, Co, Ni) is directly related to the state of charge. The as-prepared samples which are in fully lithiated state are found to be more stable than that of the partially and completely charged samples. This difference in the thermal stability could be attributed to the presence of the higher oxidation states of transition metals which tend to change to stable lower oxidation states by releasing oxygen from the structure. As a result, the structure of the materials could degrade and could even lead to phase changes. The oxygen release can lead to the oxidation of conductive additive to form CO_2 gas or can lead to the formation of metal oxides. Additional information on the structural changes was obtained from XRD.

Among the three Li$M_{0.5}Mn_{1.5}O_4$-1000 (M = Fe, Co, Ni) samples, $LiFe_{0.5}Mn_{1.5}O_4$-1000 was found to exhibit the best thermal stability in the charged as well as discharged states and the poorest by $LiNi_{0.5}Mn_{1.5}O_4$-1000. This difference could be explained based on the distribution of oxidation states in these materials. The Ni-doped material contains Ni in its divalent state and Mn in its tetravalent state, in its completely stoichiometric form. As the materials have slight oxygen deficiency, the material also contains some Mn in its trivalent form. More information on the relative Mn^{3+} ratio for these systems was obtained from the 4 V capacities shown by them. As calculated, $LiNi_{0.5}Mn_{1.5}O_4$-1000 contains ~0.08 moles and Li$M_{0.5}Mn_{1.5}O_4$-1000 (M = Fe, Co)

contains ~0.35 moles of trivalent Mn per one mole of the material. When completely charged, the Mn and *M* (Fe, Co, Ni) in Li$M_{0.5}Mn_{1.5}O_4$-1000 (*M* = Fe, Co, Ni) reaches a tetravalent oxidation state. During the partial charging, the distribution of cation valence states is even different. All the samples would have all Mn in its tetravalent oxidation state whereas the oxidation states of *M* (Fe, Co, Ni) are different. While more of the Fe and Co still remains in its trivalent state, Ni already is oxidized to Ni^{3+} or Ni^{4+} or a mixture of both states (see oxidation plateaus in Figure 11.1). The different stabilities of these oxidation states especially the Ni and *M* (Co, Fe) could be a reason for the degradation of $LiNi_{0.5}Mn_{1.5}O_4$-1000 at lower temperature than the Li$M_{0.5}Mn_{1.5}O_4$-1000 (*M* = Fe, Co) especially in the partially and completely charged states.

A comparison of the TGA results of the Li$M_{0.5}Mn_{1.5}O_4$-1000 (*M* = Fe, Co, Ni) samples with $LiMn_2O_4$ from literature shows that they exhibit similar behavior with the literature. Accordingly, with increasing delithiation, i.e. small values of x (number of moles of lithium remains); the onset temperature for its decomposition decreases **[Wang 2007].**

11.2.2 Characterization of the samples after TG-DSC analyses

The XRD analyses for the samples after TG-DSC studies of as-prepared samples until 350°C are shown in Figure 11.4a. It is interesting to note that the samples after cooling back to RT from the 350°C heat treatment shows a decrease in the lattice parameters in comparison with those calculated from the initial measurements. As these results are different from the *in situ* observations, presented later in the text, the possible explanations could be a reaction which leads to a unit cell shrinkage after the cooling of the materials. Such a reaction is very difficult to propose, but may be something like the formation of Li_2O, $Li_{1-x}C_x$ etc which leads to the unit cell shrinkage which are small amounts to be detected by XRD. Formation of any crystalline transition metal oxides could be excluded as no reflections correspond to their formation, were visible from XRD.

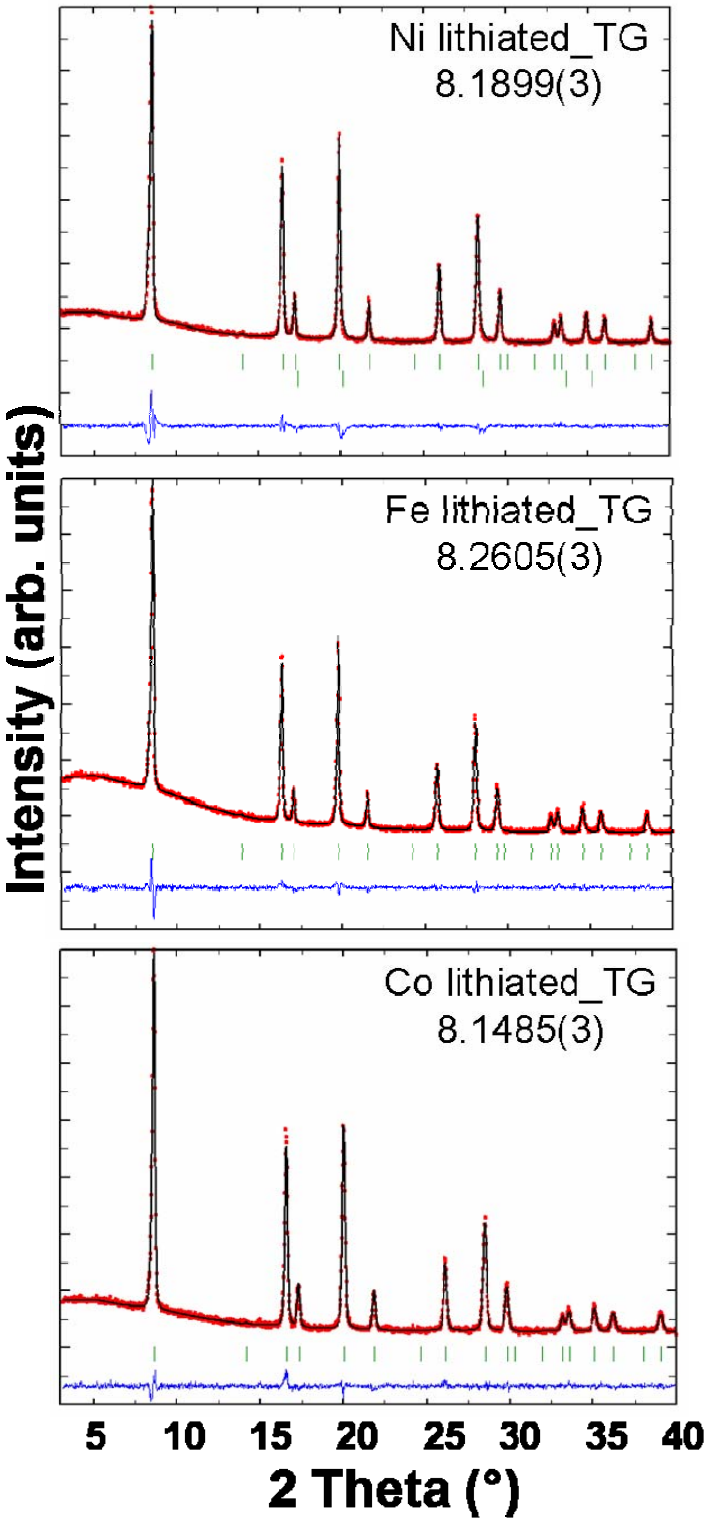

***Figure 11.4a**: RT XRD patterns obtained for as-prepared $LiM_{0.5}Mn_{1.5}O_4$-1000 (M = Fe, Co, Ni) after heating under argon at a rate of 10°C/min up to 350°C. The corresponding lattice parameters are given in the inset of each figure. The last line of reflection marks in the $LiNi_{0.5}Mn_{1.5}O_4$-1000 samples corresponds to the $Li_xNi_{1-x}O$ phase ($Fm\bar{3}m$ space group).*

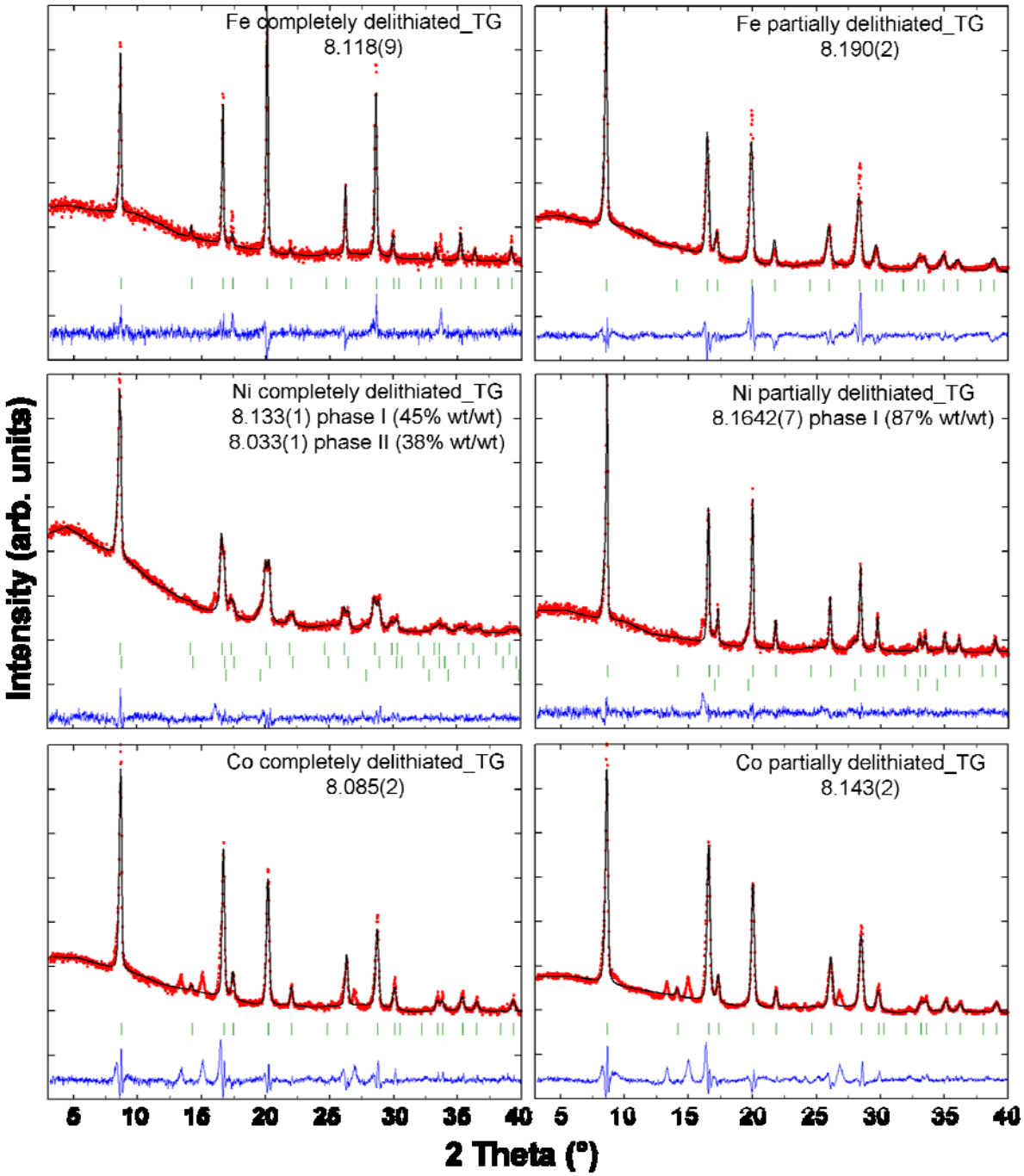

***Figure 11.4b**: RT XRD patterns obtained for, left: completely charged $LiM_{0.5}Mn_{1.5}O_4$-1000 (M = Fe, Co, Ni), right: partially charged $LiM_{0.5}Mn_{1.5}O_4$-1000 (M = Fe, Co, Ni), after heating under argon at a rate of 10°C/min up to 350°C. The corresponding lattice parameters are given in the inset of each figure. The last line of reflection marks in the $LiNi_{0.5}Mn_{1.5}O_4$-1000 samples corresponds to the $Li_xNi_{1-x}O$ phase ($Fm\bar{3}m$ space group).*

The charged samples, after heat treatment under argon until 350°C, show significant increase in the lattice parameters as revealed by the XRD analysis. This increase in the unit cell parameters confirms that oxygen loss from the lattice is the major cause of structural degradation of these materials. Another important observation is the evolution of additional reflections in the patterns after the thermal treatment, which is more pronounced for the completely charged samples. From the above observations, the drawn conclusion is that the thermal stability of Li$M_{0.5}Mn_{1.5}O_4$-1000 (M = Fe, Co, Ni) spinel cathode materials has a direct relation to the onset of oxygen expulsion from the lattice.

11.3 *in situ* structural analyses of selected samples

To extract more information on the degradation mechanism, *in situ* diffraction studies were carried out for one sample during heating. $LiNi_{0.5}Mn_{1.5}O_4$-1000 was selected for this purpose as it was showing the best electrochemical behavior but the least thermal stability. The details of the measurements and results are provided below.

11.3.1 Experimental

The structural changes were investigated from 22-300°C with *in situ* synchrotron diffraction. This was performed with the help of synchrotron facility at HASYLAB/DESY at beamline B2 **[Knapp 2004a]**, in Debye-Scherrer mode using the OBI **[Knapp 2004b]**, a STOE furnace equipped with a EUROTHERM temperature controller and a capillary spinner. Glass capillaries of diameter 0.3 mm were filled with the material inside the argon-filled glove-box, sealed and mounted inside the STOE furnace. The datasets were collected from 2θ = 5 - 60° in steps of 0.004° and in temperature steps of 20°C. The wavelength of 0.73048(1) Å was used for the measurements, as determined from the positions of 8 reflections from a LaB_6 reference material.

The obtained diffraction patterns were analyzed by using WinPLOTR software package **[Roisnel 2001]**. For determining the crystallite size precisely, the instrumental resolution function determined for LaB_6 powder reference material, was explicitly supplied to the FullProf program for an improved sensitivity against broadening of selected reflections due to an unresolved splitting of reflections. For a better structure determination, a Rietveld refinement was performed including for the

oxygen positions and with an isotropic approximation for the thermal displacement parameters.

11.3.2 Analysis of $LiNi_{0.5}Mn_{1.5}O_4$

The crystal structure of $LiNi_{0.5}Mn_{1.5}O_4$ can be refined at room temperature in the space group $Fd\bar{3}m$ with a lattice parameter of 8.1893(2) Å. At elevated temperatures, a second spinel phase with the same cubic symmetry but a larger lattice parameter was observed to appear, see Figure 11.5. These two phases could exhibit different cation stoichiometry, but most probably a partial reduction of $LiNi_{0.5}Mn_{1.5}O_4$ takes place in the argon atmosphere in presence of amorphous carbon as indicated by the increase in the lattice parameters. Diffraction patterns starting from 240°C can be explained based on the model with two spinel phases with slightly different lattice parameters, but more probably crystallites with an inhomogeneous distribution of oxygen should exist.

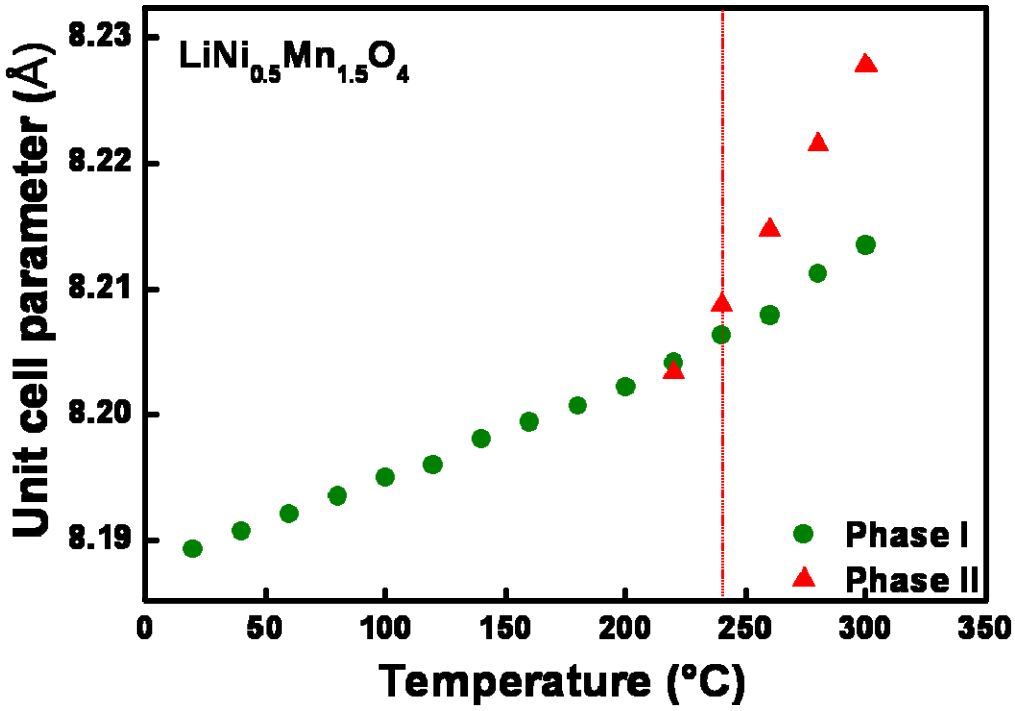

***Figure 11.5a**: Temperature dependence of lattice parameter a, for $LiNi_{0.5}Mn_{1.5}O_4$. Close to 240°C, a partial reduction of the phase takes place, which is reflected in the different slope of the dependence a = a(T).*

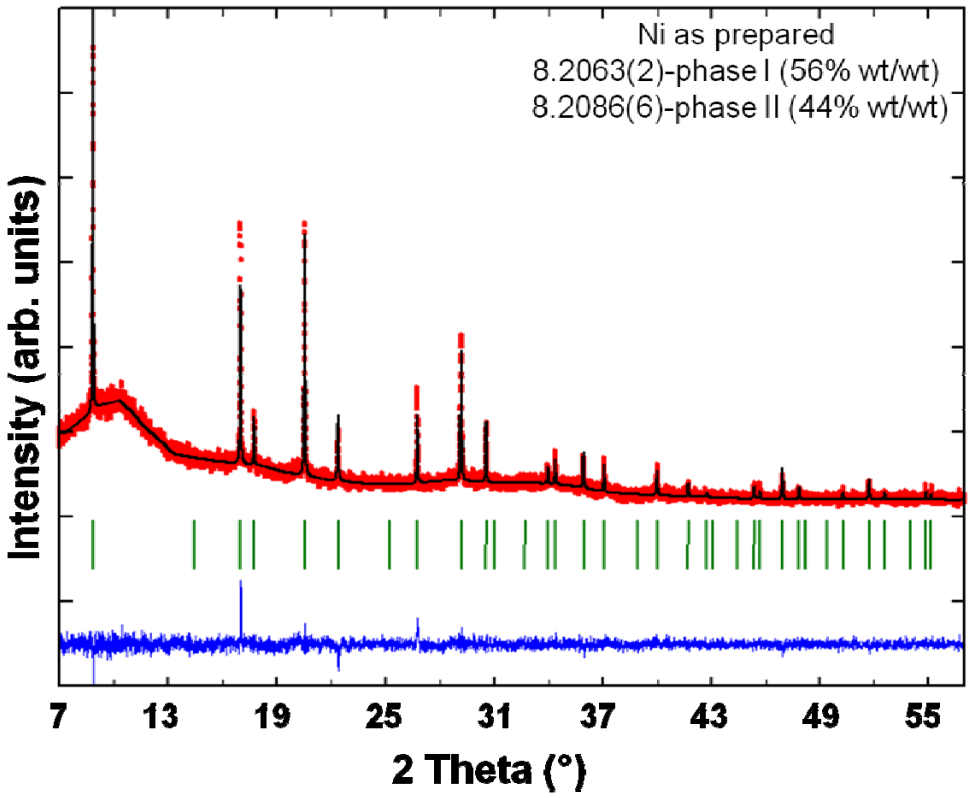

***Figure 11.5b**: Diffraction pattern corresponds to the temperature (240°C) where the second spinel phase starts to appear. The phase ratio and the corresponding lattice parameters are given in the inset.*

11.3.3 Analysis of $Li_xNi_{0.5}Mn_{1.5}O_4$ ($x \approx 0$)

The diffraction pattern of "$Li_{x\approx0}Ni_{0.5}Mn_{1.5}O_4$" sample can be described at room temperature based on two spinel phases (space group $Fd\bar{3}m$) with slightly different lattice parameters a = 8.0065(1) Å and a = 8.0169(3) Å, and a small amount of cubic $Li_xNi_{1-x}O$ (less than 4%w/w). These two phases should demonstrate a small difference in the lithium content, as a result of differential charging and the phase with more lithium should have a larger unit cell.

Close to 220°C, the appearance of a third spinel phase together with significant increasing of the lattice parameters of the spinel phase with higher lithium content was observed (At the same time the $Li_xNi_{1-x}O$ content in the sample increased from 3.5% (w/w) up to 32% (w/w), see Figure 11.6. The lattice parameter a = 8.4295(7) Å of the

new spinel phase at 300°C corresponds to the one of Mn_3O_4 with spinel structure (a = 8.42 Å **[Faulring 1960]**), so that a decomposition of $Li_{x\approx0}Ni_{0.5}Mn_{1.5}O_4$ with the formation of Mn_3O_4-like phase with a small lithium-content and elimination of $Li_xNi_{1-x}O$ under reduced conditions can be proposed. Note that the phase with less lithium content seems to be more stable against thermal decomposition and reduction which is in good agreement with the DSC results for this material where the partially delithiated material (which can be compared with the lithium rich phase here) had a lower onset temperature of degradation than the completely charged material.

Hence it can be concluded that the degradation of the materials proceeds via an oxygen release from the lattice. The onset temperature of degradation is also found to be lower for a delithiated state in comparison with the fully lithiated state. However, these experiments were performed in the absence of any electrolytes. In the presence of electrolyte the onset temperature of degradation could be more reduced **[Wang 2007, Xiang 2009]**.

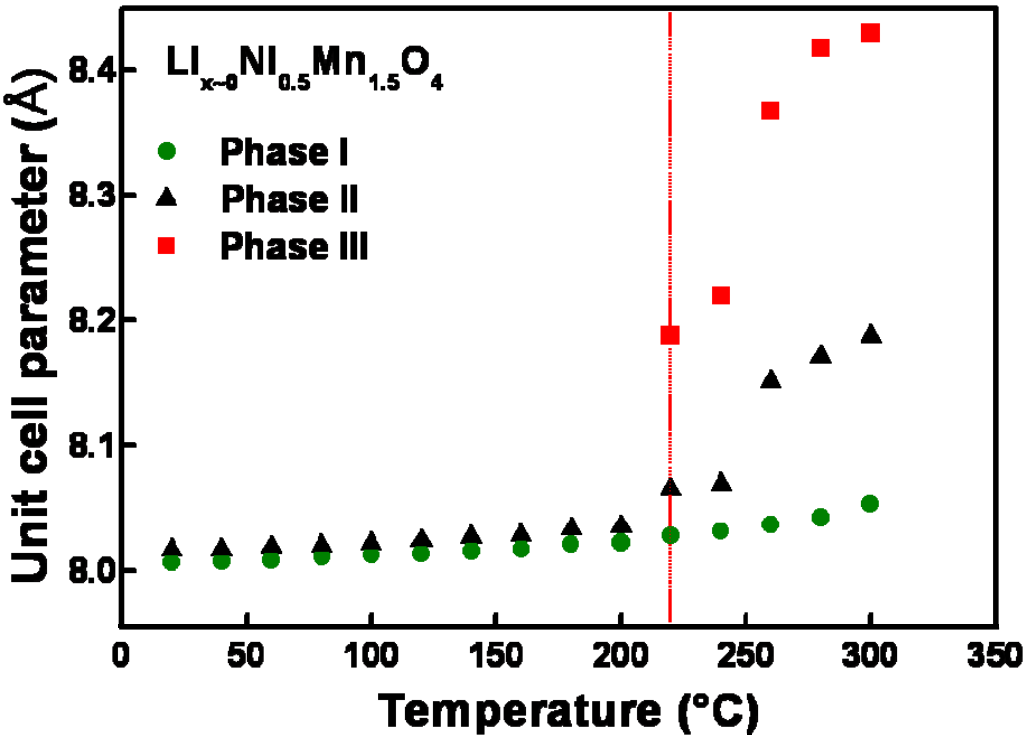

***Figure 11.6a**: Temperature dependence of lattice parameter a, for spinel phases of "$Li_{x\approx0}Ni_{0.5}Mn_{1.5}O_4$"-sample. Close to 220°C, the appearance of the third spinel phase together with the significant increasing of the lattice parameters of another spinel phase was observed.*

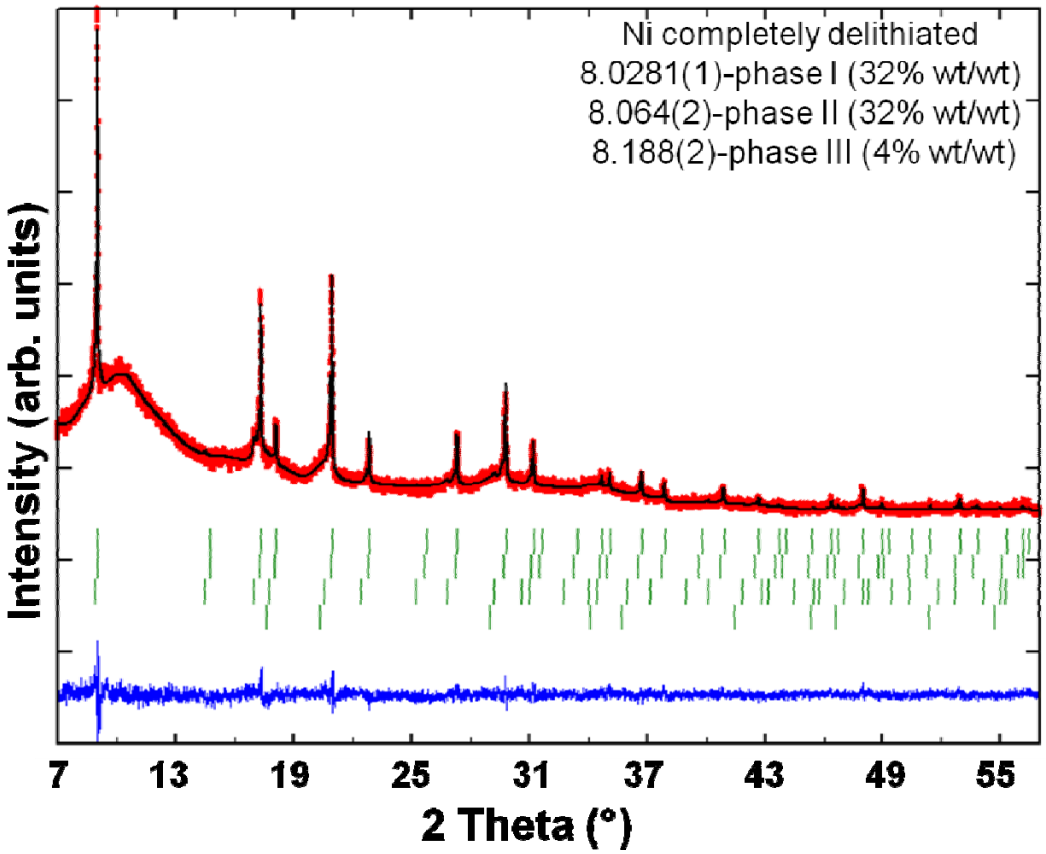

***Figure 11.6b**: Diffraction pattern corresponds to the temperature (220°C) where the third spinel phase starts to appear. The phase ratio and the corresponding lattice parameters are given in the inset. The last line of reflection marks corresponds to the $Li_xNi_{1-x}O$ phase ($Fm\bar{3}m$ space group).*

Chapter 12
Summary and Conclusions

The goal of this work was the synthesis, characterization and study of the operation mechanisms of high-voltage spinels $LiM_{0.5}Mn_{1.5}O_4$ (M = Fe, Co, Ni as positive electrode materials for lithium-ion batteries. The syntheses of these materials were successfully performed by a citric acid assisted Pechini process. It was found that $LiM_{0.5}Mn_{1.5}O_4$ (M = Fe, Co, Ni) spinels were formed at 600°C, with a prolonged annealing time of 24 h with intermittent grinding. The X-ray and neutron diffraction analysis confirmed the crystallization of the samples in $Fd\bar{3}m$ space group for M = Fe and Co, but $P4_332$ with a high degree of 3d-cation disorder for M = Ni. These samples also showed a change in the lattice parameter, better crystallinity and an increased particle size when excursed to 1000°C. The high-temperature treatment resulted in the loss of Ni/Mn ordering in $LiNi_{0.5}Mn_{1.5}O_4$ and transformation of primitive simple cubic structure ($P4_332$) to face-centered spinel ($Fd\bar{3}m$) Chemical analysis showed a slight Mn excess for the Fe doped sample which was further supported by the calculated stoichiometry from the neutron diffraction studies. Thermogravimetric analysis in air showed that all the materials remained stable till ~650°C and exhibited a weight loss after this temperature, which is an indication of oxygen loss, further supported by the increase in the unit cell parameters of the materials after 1000°C excursion. The materials synthesized by fast excursion to 1000°C exhibited an uptake of weight close to 650°C, which is additional confirmation of the oxygen deficiency in this material. However this oxygen deficiency is not very high, as understood from the small amount of weight gain.

Electrochemical characterization revealed a 4 V and 5 V activity for $LiM_{0.5}Mn_{1.5}O_4$ (M = Fe, Co), in the voltage range 3.5 - 5.3 V, and only 5 V activity for $LiNi_{0.5}Mn_{1.5}O_4$, in the voltage range 3.5 - 5.1 V. An exceptional behavior was exhibited by $LiFe_{0.5}Mn_{1.5}O_4$ in the 5 V region and a detailed investigation by varying

the cycling rate and introduction of OCV periods between the charge and discharge demonstrated the dependence of the character and the position of the PITT peak on the kinetic parameters. When comparing the cyclabilities of the synthesized samples, the Li$M_{0.5}Mn_{1.5}O_4$-1000 (M = Fe, Co, Ni) spinel showed better cycling stability in comparison with Li$M_{0.5}Mn_{1.5}O_4$-600 (M = Fe, Co; Ni) which can be attributed to the better crystallinity and reduced active surface. $LiCo_{0.5}Mn_{1.5}O_4$-1000 and $LiFe_{0.5}Mn_{1.5}O_4$-1000 showed poorer cyclability at 55°C in comparison with $LiNi_{0.5}Mn_{1.5}O_4$-1000 which can be a result of the slightly enhanced end-of-charge voltage and also may be associated with side reactions at the high operation voltage or a difference in the solid electrolyte interface formation. The rate capability was found to be almost not affected by the specific dopant 3d element.

The *in situ* synchrotron diffraction measurements elucidate a solid-solution mechanism of lithium extraction for $LiFe_{0.5}Mn_{1.5}O_4$ -1000 and $LiCo_{0.5}Mn_{1.5}O_4$ -1000. Upon lithium re-insertion, a two-phase mechanism was revealed for Fe-doped spinel in the range ($0.09 \leq x \leq 0.53$) in $Li_xFe_{0.5}Mn_{1.5}O_4$. Based on the results of PITT analysis, the appearance of two-phase region can result from poor kinetics of lithium re-insertion into $Li_xFe_{0.5}Mn_{1.5}O_4$.

The metal dissolution studies of the Li$M_{0.5}Mn_{1.5}O_4$-1000 (M = Fe, Co; Ni) cathodes in electrolyte solution showed that the delithiated state is more prone to a metal dissolution than the lithiated state. The percentage of metal dissolution was found more at 55°C than at RT. Mn dissolution percentage was higher than the other substituted transition metal in all the Li$M_{0.5}Mn_{1.5}O_4$-1000 (M = Fe, Co; Ni) materials. The cathodes after the metal dissolution experiment (aged cathodes), showed inferior cyclability in comparison with the fresh cathodes. Hence it could be concluded that metal dissolution from the spinel structural framework leads to deterioration of the electrochemical performance. In order to prevent the dissolution, the materials were coated with ZnO with a sol-gel process and the presence, uniformity and thickness of coating was analyzed by TEM and XPS analyses. In contrast to the expectation, the materials showed deteriorated electrochemical behavior after coating, which could be due to the added up electrolyte decomposition by catalysing property of ZnO.

Thermal stability studies of the Li$M_{0.5}Mn_{1.5}O_4$-1000 (M = Fe, Co) cathodes were conducted using combined TG-DSC analysis. The onset temperature is found to be

lowest for the completely charged samples and slightly higher for the partially charged samples except in the case of $LiNi_{0.5}Mn_{1.5}O_4$-1000 (most probably due to the presence of Ni in its unstable trivalent oxidation state during partial charging which tend to reduce to its stable divalent oxidation state by releasing oxygen). The reason of the less stability of the completely charged $LiM_{0.5}Mn_{1.5}O_4$-1000 (M = Fe, Co) could be the existence of most of the transition metal ions in its tetravalent form in the charged samples. These ions tend to get reduced to their stable valencies mainly by releasing oxygen from the structural framework. The released oxygen in turn reacts with the carbon present in the cathode and degrades the composite by expelling carbon dioxide. Hence it can be concluded that the thermal stability is directly related to the extent of lithium content in the samples for $LiM_{0.5}Mn_{1.5}O_4$-1000 (M = Fe, Co). Charged Ni doped spinel exhibited a lower thermal stability than the Co and Fe doped spinel, which could be due to the lower stability of Ni^{4+} in comparison with the Co^{4+} and Fe^{4+} that in the former case the oxygen release takes place at even lower temperature than the latter. *in situ* XRD studies performed for uncharged Ni-doped spinel showed that the material start to degrade above ~240°C and forms an extra cubic spinel phase in addition with the $Li_xNi_{1-x}O$ phase existed before. The investigations for the charged Ni doped spinel revealed an onset temperature of ~220°C which lead to the formation of a Mn_3O_4 phase and a significant increase in the phase ratio of $Li_xNi_{1-x}O$ phase. Also it was observed that the smaller lithium content in the charged material got a higher onset temperature of structural degradation.

List of figures

List of tables

Bibliography

Aitchison 1999 P. Aitchison, B. Ammundsen, D. J. Jones, G. Burns and J. Roziére, *"Cobalt substitution in lithium manganate spinels: examination of local structure and lithium extraction by XAFS"*, J. Mater. Chem. **9** (1999) 3125-3130

Aklalouch 2008 M. Aklalouch, J. M. Amarilla, R. M. Rojas, I. Saadoune and J. M. Rojo, *"Chromium doping as a new approach to improve the cycling performance at high temperature of 5 V $LiNi_{0.5}Mn_{1.5}O_4$-based positive electrode"*, J. Power Sources **185** (2008) 501-511

Alcántara 2004 R. Alcántara, M. Jaraba, P. Lavela and J. L. Tirado, *"X-ray diffraction and electrochemical impedance spectroscopy study of zinc coated $LiNi_{0.5}Mn_{1.5}O_4$ electrodes"*, J. Electroanal. Chem. **566** (2004) 187–192

Amine 1996 K. Amine, H. Tukamoto, H. Yasuda and Y. Fujita, *"A New Three-Volt spinel $Li_{1+x}Mn_{1.5}Ni_{0.5}O_4$ for secondary lithium batteries"*, J. Electrochem. Soc. **143** (1996) 1607

Amine 1997 K. Amine, H. Tukamoto, H. Yasuda and Y. Fujita, *"Preparation and electrochemical investigation of $LiMn_{2-x}Me_xO_4$ (Me: Ni, Fe, and x = 0.5, 1) cathode materials for secondary lithium batteries"*, J. Power Sources **68** (1997) 604-608

Ariyoshi 2003 K. Ariyoshi, S. Yamamoto and T. Ohzuku, *"Three-volt lithium-ion battery with $LiNi_{0.5}Mn_{1.5}O_4$ and the zero-strain insertion material of $LiLi_{0.33}Ti_{1.67}O_4$"*, J. Power Sources **119-121** (2003) 959

Ariyoshi 2004 K. Ariyoshi, Y. Iwakoshi, N. Nakayama and T. Ohzuku, *"Topotactic two-phase reactions of $LiNi_{0.5}Mn_{1.5}O_4$ ($P4_332$) in nonaqueous lithium cells"*, J. Electrochem. Soc. **151** (2004) 296-303

Arrebola 2006a J. C. Arrebola, A. Caballero, M. Cruz, L. Hernán, J. Morales and E. R. Castellón, *"Crystallinity control of a nanostructured $LiNi_{0.5}Mn_{1.5}O_4$ spinel via polymer-assisted synthesis: a method for improving its rate capability and performance in 5 V lithium batteries"*, Adv. Funct. Mater. **16** (2006) 1904–1912

Arrebola 2006b J. C. Arrebola, A. Caballero, L. Hernán, M. Melero, J. Morales and E. R. Castellón, *"Electrochemical properties of $LiNi_{0.5}Mn_{1.5}O_4$ films prepared by spin-coating deposition"*, J. Power Sources **162** (2006) 606-613

Aurbach 1999 D. Aurbach, B. Markovsky, I. Weissman, E. Levi and Y. Ein-Eli, *"On the correlation between surface chemistry and performance of graphite negative electrodes for Li ion batteries"*, Electrochim. Acta **45** (1999) 67

Aurbach 2006 D. Aurbach, B. Markovsky, Y. Talyossef, G. Salitra, H.-J. Kim and S. Choi, *"Studies of cycling behavior, ageing, and interfacial reactions of $LiNi_{0.5}Mn_{1.5}O_4$ and carbon electrodes for lithium-ion 5-V cells"*, J. Power Sources **162** (2006) 780–789

Balbuena 2004 P. B. Balbuena and Y. Wang, *"Lithium-ion batteries: Solid-electrolyte interface"*, Imperial College Press (2004)

Berar 1991 J. F. Berar, P. Lelann, *"ESDs and estimated probable-error obtained in rietveld refinements with local correlations"*, J. Appl. Crystallogr. **24** (1991) 1-5

Besenhard 1987 J. O. Besenhard, J. Gürtler, P. Komenda, and A. Paxinos, *"Corrosion protection of secondary lithium electrodes in organic electrolytes*", J. Power Sources **20** (1987) 253

Besenhard 1995 J. O. Besenhard, M. Winter, J. Yang and W. Biberacher, *"Filming mechanism of lithium-carbon anodes in organic and inorganic electrolytes"*, J. Power Sources **54** (1995) 228

Besenhard 1997 J. O. Besenhard, J. Yang and M. Winter, *"Will advanced lithium-alloy anodes have a chance in lithium-ion batteries?"*, J. Power Sources **68** (1997) 87

Besenhard 1999 G. Hambitzer, K Pinkwart, C. Ripp, C. Schiller, *"Handbook of battery materials"*, (ed., J. O. Besenhard), WILEY-VCH Verlag GmbH, D-69469, Weinheim, Germany (1999)

Bhaskar 2010 A. Bhaskar, N. N. Bramnik, A. Senyshyn, H. Fuess and H. Ehrenberg, *"Synthesis, characterization, and comparison of electrochemical properties of* $LiM_{0.5}Mn_{1.5}O_4$ *(M = Fe, Co, Ni) at different temperatures"*, J. Electrochem. Soc. **157** (2010) 689-695

Bockris 1981 J. O'M. Bockris, B. E. Conway, E. Yeager and R. E. White, *"Comprehensive treatise of electrochemistry"*, Plenum Publishing Corp. **3** (1981) 341-470

Bonhote 1996 P. Bonhote, A. P. Dias, N. Papageorgiou, K. Kalyanasundaram and M. Gratzel, *"Hydrophobic, highly conductive ambient-temperature molten salts"*, Inorg. Chem. **35** (1996) 1168

Bramnik 2008 N. N. Bramnik, K. Nikolowski, D. M. Trots, and H. Ehrenberg, *"Thermal stability of* $LiCoPO_4$ *cathodes"*, Electrochem. Solid-State Lett. **11** (2008) A89-A93

Buqa 2005 H. Buqa, A. Würsig, D. Goers, L. J. Hardwick, M. Holzapfel, P. Novàk, F. Krumeich, M. E. Spahr, *"Behavior of highly*

crystalline graphites in lithium-ion cells with propylene carbonate containing electrolytes", J. Power Sources **146** (2005) 134

Caballero 2005 A. Caballero, L. Hernán, M. Melero, J. Morales and M. Angulo, *"Oxygen lattice instability as a capacity fading mechanism for 5 V cathode materials"*, J. Electrochem. Soc. **152** (2005) 6-12

Chan 2008 C. K. Chan, H. Peng, G. Liu, K. McIlwrath, X. F. Zhang, R. A. Huggins and Y. Cui, *"High-performance lithium battery anodes using silicon nanowires"*, Nature Nanotechnology **3**, (2008) 31-35

Courtney 1997 I. A. Courtney and J. R. Dahn, *"Electrochemical and in situ X-ray diffraction studies of the reaction of lithium with tin oxide composites"*, J. Electrochem. Soc. **144** (1997) 2045

Dahéron 2008 L. Dahéron, R. Dedryvère, H. Martinez, M. Ménétrier, C. Denage, C. Delmas and. Gonbeau, *"Electron transfer mechanisms upon lithium deintercalation from $LiCoO_2$ to CoO_2 investigated by XPS"*, Chem. Mater. **20** (2008) 583–590

Djian 2007 D. Djian, F. Alloin, S. Martinet, H. Lignier and J. Y. Sanchez, *"Lithium-ion batteries with high charge rate capacity: Influence of the porous separator"*, J. Power Sources **172** (2007) 416-421

Dokko 2004 K. Dokko,, N. Anzue, M. Mohamedi, T. Itoh, I. Uchida, *"Raman spectro-electrochemistry of $LiCo_xMn_{2-x}O_4$ thin film electrodes for 5 V lithium batteries"*, Electrochem. Commun. **6** (2004) 384–388

Dominey 1994 L. A. Dominey, *"Lithium batteries: new materials, developments and perspectives"*, Elsevier, Amsterdam (1994) 137

Dominko 2001 R. Dominko, M. Gaberscek, J. Drofenik, M. Bele and S. Pejovnik, *"A novel coating technology for preparation of cathodes in Li-ion batteries"*, Electrochem. Solid-State Lett. **4** (2001) 187

EC-Lab EC-Lab software user's manual, Version 9.9, BioLogic science instruments.

Eftekhari 2003 A. Eftekhari, *"Electrochemical performance and cyclability of $LiFe_{0.5}Mn_{1.5}O_4$ as a 5 V cathode material for lithium batteries"*, J. Power Sources **124** (2003) 182–190

Eftekhari 2004 A. Eftekhari, *"Fabrication of 5 V lithium rechargeable micro-battery"*, J. Power Sources **132** (2004) 240–243

Endres 2004 F. Endres, *"Ionic liquids: promising solvents for electrochemistry"*, Zeitschrift für Physikalische Chemie **218** (2004) 255

Fan 2007 Y. Fan, J. Wang, Z. Tang, W. He and J. Zhang, *"Effects of the nanostructured SiO_2 coating on the performance of $LiNi_{0.5}Mn_{1.5}O_4$ cathode materials for high-voltage Li-ion batteries"*, Electrochim. Acta **52** (2007) 3870–3875

Fang 2007 H. Fang, Z. Wang, B. Zhang, X. Li and G. Li, *"High performance $LiNi_{0.5}Mn_{1.5}O_4$ cathode materials synthesized by a combinational annealing method"*, Electrochem. Commun. **9** (2007) 1077-1082

Faulring 1960 G. M. Faulring, W. K. Zwicker, W. D. Forgeng, *"Thermal transformations and properties of cryptomelane"*, Am. Mineral. **45** (1960) 947

Fong 2009 R. Fong, U. Vonsacken and J. R. Dahn, *"Studies of lithium intercalation into carbons using nonaqueous electrochemical-cells"*, J. Electrochem. Soc. **137** (1990) 2009

Forsyth 2003 S. A. Forsyth and D. R. MacFarlane, *"1-alkyl-3-methylbenzotriazolium salts: ionic solvents and electrolytes"*, J. Mater. Chem. **13** (2003) 2451

Fuller 1997 J. Fuller, R. T. Carlin and R. A, Osteryoung, *"The room temperature ionic liquid 1-ethyl-3- methylimidazolium tetrafluoroborate: electrochemical couples and physical properties"*, J. Electrochem. Soc. **144** (1997) 3881

Gabano 1983 J. P. Gabano, *"Lithium batteries"*, Academic Press, London

Gao 1996 Y. Gao. K. Myrtle, M. Zhang, J. N. Reimers and J. R. Dahn, *"Valence band of $LiNi_xMn_{2-x}O_4$ and its effects on the voltage profiles of $LiNi_xMn_{2-x}O_4$/Li electrochemical cells"*, Phys. Rev. **54** (1996) 16670-16675

Golding 2002 J. Golding, S. Forsyth, D. R. MacFarlane, M. Forsyth and G. B. Deacon, *"Methanesulfonate and p-toluenesulfonate salts of the N-methyl-N-alkylpyrrolidinium and quaternary ammonium cations: novel low cost ionic liquids"*, Green Chem. **4** (2002) 223

Goodenough J. Goodenough, *"Electrochemical cell with new fast ion conductors"*, U. S. Patent 4302518

Gritzner 1993 G. Gritzner and G. Kreysa, *"Nomenclature, symbols and definitions in electrochemical engineering"*, Pure & Appl. Chem. **65** (1993) 1010

Gummow 1994 R. J. Gummow, A. de Kock and M. M. Thackeray, *"Improved capacity retention in rechargeable 4 V lithium/lithium manganese oxide (spinel) cells"*, Solid State Ionics **69** (1994) 59-67

Guohua 1996 L. Guohua, H. Ikuta, T. Uchida and W. Wakihara, *"The spinel phases $LiM_yMn_{2-y}O_4$ (M = Co, Cr, Ni) as the cathode for*

rechargeable lithium batteries", J. Electrochem. Soc. **143** (1996) 178

Guyomard 1995 D. Guyomard and J. M. Tarascon, *"High voltage stable liquid electrolytes for $Li_{1+x}Mn_2O_4$/carbon rocking-chair lithium batteries"*, J. Power Sources **54** (1995) 92

Hagiwara 2000 R. Hagiwara and Y. Ito, *"Room temperature ionic liquids of alkylimidazolium cations and fluoroanions"*, J. Fluorine Chem. **105** (2000) 221

Hardwick 2007 L. J. Hardwick, *"in situ Raman microscopy of insertion electrodes for lithium-ion batteries and supercapacitors"*, Dissertation, Swiss federal institute of technology, Zurich (2007)

Hernán 2002 L. Hernán, J. Morales, L. Sánchez, E. Rodríguez Castellón and M. A. G. Aranda, *"Synthesis, characterization and comparative study of the electrochemical properties of doped lithium manganese spinels as cathodes for high voltage lithium batteries"*, J. Mater. Chem. **12** (2002) 734–741

Holzapfel 2004 M. Holzapfel, C. Jost and P. Novàk, *"Stable cycling of graphite in an ionic liquid based electrolyte"*, Chem. Commun. **18** (2004) 2098

Jow 1982 T. R. Jow and C. C. Liang, *"Lithium-aluminum electrodes at ambient temperatures"*, J. Electrochem. Soc. **129** (1982) 1429

Kawai 1998a H. Kawai, M. Nagata, H. Tukamoto and A. R. West, *"A novel cathode $Li_2CoMn_3O_8$ for lithium ion batteries operating over 5 volts"*, J. Mater. Chem. **8** (1998) 837-839

Kawai 1998b H. Kawai, M. Nagata, M. Tabuchi, H. Tukamoto, A. R. West, *"Novel 5 V spinel cathode $Li_2FeMn_3O_8$ for lithium ion batteries"*, Chem. Mater. **10** (1998) 3266-3268

Kawai 1999 H. Kawai, M. Nagata, H. Tukamoto and A. R. West, *"High voltage lithium cathode materials"*, J. Power Sources **81-82** (1999) 67-72

Kim 2003 B. Kim, Y. Choi and Y. Cho, *"Synthesis of $LiFe_xMn_{2-x}O_4$ cathode materials by emulsion method and their electrochemical properties"*, Solid State Ionics **158** (2003) 281–285

Kim 2004a J. -H. Kim, S. -T. Myung, C. S. Yoon, S. G. Kang and Y. -K. Sun, *"Comparative study of $LiNi_{0.5}Mn_{1.5}O_{4-\delta}$ and $LiNi_{0.5}Mn_{1.5}O_4$ cathodes having two crystallographic structures: $Fd\bar{3}m$ and $P4_332$"*, Chem. Mater. **16** (2004) 906-914

Kim 2004b J. -H. Kim, C. S. Yoon, S. -T. Myung, J. Prakash and Y. -K. Sun, *"Phase Transitions in $LiNi_{0.5}Mn_{1.5}O_4$ during Cycling at 5 V"*, Electrochemical and Solid-State Letters **7** (2004) 216-220

Knapp 2004a M. Knapp, C. Baehtz, H. Ehrenberg, H. Fuess, *"The synchrotron powder diffractometer at beamline B2 at HASYLAB/DESY: status and capabilities"*, J. Synchrotron Rad. **11** (2004) 328-334

Knapp 2004b M. Knapp, V. Joco, C. Baehtz, H. H. Brecht, A. Berghaeuser, H. Ehrenberg, H. von Seggern and H. Fuess, *"Position-sensitive detector system OBI for high resolution X-ray powder diffraction using on-site readable image plates"*, Nucl. Instrum. Methods **521** (2004) 565

Kunduraci 2008 M. Kunduraci and G.G. Amatucci, *"The effect of particle size and morphology on the rate capability of 4.7V $LiMn_{1.5+\delta}Ni_{0.5-\delta}O_4$ spinel lithium-ion battery cathodes"*, Electrochim. Acta **53** (2008) 4193–4199

Kweon 2000 H. J. Kweon, S. J. Kim, D. G. Park, *"Modification of $Li_xNi_{1-y}Co_yO_2$ by applying a surface coating of MgO"*, J. Power Sources **88** (2000) 255

Lamm 2010 A. Lamm, P. Friebe, T. Soczka-Guth and R. Justen, *"Safety aspects on Li-ion-batteries for future mobility concepts"*, *12th Ulm electrochemical talks (2010)*

Larcher 2000 D. Larcher, L. Y. Beaulieu, D. D. MacNeil and J. R. Dahn, *"in situ X-ray study of the electrochemical reaction of Li with eta '-Cu_6Sn_5"*, J. Electrochem. Soc. **147** (2000) 1658

Levi 1999 M. D. Levi, G. Salitra, B. Markovsky, H. Teller, D. Aurbach, U. Heider, and L. Heider, *"Solid-State electrochemical kinetics of Li-ion intercalation into $Li_{1-x}CoO_2$: simultaneous application of electroanalytical techniques SSCV, PITT, and EIS"*, J. Electrochem. Soc. **146** (1999) 1279-1289

Lim 2001 M. R. Lim, W. I. Cho, K. B. Kim, *"Preparation and characterization of gold-codeposited $LiMn_2O_4$ electrodes"*, J. Power Sources **92** (2001) 168

Linden 2002 D. Linden and T. B. Reddy, *"Handbook of batteries"*, 3rd Edition, McGraw-Hill, New York (2002)

Liu 1996 W. Liu and G. C. Farrington, F. Chaput and B. Dunn, *"Synthesis and electrochemical studies of spinel phase $LiMn_2O_4$ cathode materials prepared by the pechini process"*, J. Electrochem. Soc. **143** (1996) 879-884

Liu 2002 L. Liu, Z. Wang, H. Li, L. Chen and X. Huang, *"Al_2O_3-coated $LiCoO_2$ as cathode material for lithium ion batteries"*, Solid State Ionics **152–153** (2002) 341

Liu 2007 D. Liu, X. Liu and Z. He, *"Surface modification by ZnO coating for improving the elevated temperature performance of $LiMn_2O_4$"*, J. Alloys and compounds **436** (2007) 387-391

Locati 2007 C. Locati, U. Lafont , L. Simonin , F. Ooms and E. M. Kelder, *"Mg-doped $LiNi_{0.5}Mn_{1.5}O_4$ spinel for cathode materials"*, J. Power Sources **174** (2007) 847–851

MacFarlane 1999 D. R. MacFarlane, P. Meakin, J. Sun, N. Amini and M. Forsyth, *"Pyrrolidinium imides: a new family of molten salts and conductive plastic crystal phases"*, J. Phys. Chem. **103** (1999) 4164

Mantia 2008 F. L. Mantia, F. Rosciano, N. Tran and P. Novák, *"Direct evidence of oxygen evolution from $Li_{1+x}(Ni_{1/3}Mn_{1/3}Co_{1/3})_{1-x}O_2$ at high potentials"*, J. Appl. Electrochem. 38(2008) 893-896

Markovsky 2004 B. Markovsky, Y. Talyossef, G. Salitra, D. Aurbach, H. –J. Kim and S. Choi**,** *"Cycling and storage performance at elevated temperatures of $LiNi_{0.5}Mn_{1.5}O_4$ positive electrodes for advanced 5 V Li-ion batteries"*, Electrochem. Commun. **6** (2004) 821-826

McEwen 1999 A. B. McEwen, H. L. Ngo, K. LeCompte and J. L. Goldman, *"Electrochemical properties of imidazolium salt electrolytes for electrochemical capacitor applications"*, J. Electrochem. Soc. **146** (1999) 1687-1695

Mengeritsky 1996 E. Mengeritsky, P. Dan, J. Weisman, A. Zaban, and D. Aurbach, *"Safety and performance of tadiran TLR-7103 rechargeable batteries"*, J. Electrochem. Soc. **143** (1996) 2110-2116

Mladenov 2001 M. Mladenov, R. Stoyanova, E. Zhecheva and S. Vassilev, *"Effect of Mg doping and MgO-surface modification on the cycling stability of $LiCoO_2$ electrode"*, Electrochem. Commun. **3** (2001) 410

Mukerjee 2004 S. Mukerjee, X. Q. Yang, X. Sunb, S. J. Lee, J. McBreen and Y. Ein-Eli, *"in situ synchrotron X-ray studies on copper–nickel 5 V Mn oxide spinel cathodes for Li-ion batteries"*, Electrochim. Acta **49** (2004) 3373–3382

Muraliganth 2010 T. Muraliganth, K. R. Stroukoff, and A. Manthiram, *"Microwave-solvothermal synthesis of nanostructured Li_2MSiO_4/C (M = Mn and Fe) cathodes for lithium-ion batteries"*, Chem. Mater. **22** (2010) 5754–5761

Narukawa 2002 S. Narukawa, I. Nakane, N. Imachi, S. Fukuoka and M. Yamasaki, *"Recent advances in li-ion polymer battery technology"*, 11th IMLB, Monterey (2002)

Nikolowski 2005 K. Nikolowski, C. Baehtz, N. N. Bramnik and H. Ehrenberg, *"A Swagelok-type in situ cell for battery investigations using synchrotron radiation"*, J. Appl. Crystallogr. **38** (2005) 851-853

Nishida 2003 T. Nishida, Y. Tashiro and M. Yamamoto, *"Physical and electrochemical properties of 1- alkyl-3-methylimidazolium tetrafluoroborate for electrolyte"*, J. Fluorine Chem. 135(2003)

Numata 2000 T. Numata, C. Amemiya, J. Iriyama, T. Miura and M. Shirakata, *"Special issue on lithium-ion rechargeable batteries - advantages of blended electrode for lithium-ion rechargeable batteries"*, NEC R&D **41** (2000) 8

Ohno 2002 H. Ohno and M. Yoshizawa, *"Ion conductive characteristics of ionic liquids prepared by neutralization of alkylimidazoles"*, Solid State Ionics **154** (2002) 303

Ohzuku 1994 T. Ohzuku and A. Ueda, *"Solid-state redox reactions of $LiCoO_2$ ($R\bar{3}m$) for 4 volt secondary lithium cells"*, J. Electrochem. Soc. **141** (1994) 2972-2977

Ohzuku 1999 T. Ohzuku, S. Takeda and M. Iwanaga, *"Solid-state redox potentials for $Li[Me_{0.5}Mn_{1.5}]O_4$ (Me: 3d-transition metal) having spinel-framework structures: a series of 5 volt materials for advanced lithium-ion batteries"*, J. Power Sources **81–82** (1999) 90–94

Ohzuku 2001 T. Ohzuku, K. Ariyoshi, S. Takeda and Y. Sakai, *"Synthesis and characterization of 5 V insertion material of $Li[Fe_yMn_{2-y}]O_4$ for lithium-ion batteries"*, Electrochim. Acta 46 (2001) 2327–2336

Okada 2000 M. Okada, Y-S. Lee and M. Yoshio, *"Cycle characterizations of $LiM_xMn_{2-x}O_4$ (M = Co, Ni) materials for lithium secondary battery at wide voltage region"*, J. Power Sources **90** (2000) 196–200

Oswald 2009 S. Oswald, K. Nikolowski and H. Ehrenberg, *"Quasi in situ XPS investigations on intercalation mechanisms in Li-ion battery materials"*, Anal. Bioanal. Chem. **393** (2009) 1871–1877

Ozawa 2009 K. Ozawa, *"Lithium ion rechargeable batteries: materials, technology and new applications"*, Wiley-VCH 2009

Park 2007 S. H. Park , S.-W. Oh , S. H. Kang, I. Belharouak, K. Amine and Y.-K. Sun, *"Comparative study of different crystallographic structure of $LiNi_{0.5}Mn_{1.5}O_{4-\delta}$ cathodes with wide operation voltage (2.0–5.0 V)"*, Electrochim. Acta **52** (2007) 7226–7230

Pasero 2008 D. Pasero, N. Reeves V. Pralong and A. R. West, *"Oxygen non-stoichiometry and phase transitions in $LiMn_{1.5}Ni_{0.5}O_4$"*, J. Electrochem. Soc. **155** (2008) 282-291

Peled 1979 E. Peled, *"The electrochemical-behavior of alkali and alkaline-earth metals in non-aqueous battery systems - the solid electrolyte interphase model"*, J. Electrochem. Soc. **126** (1979) 2047

Pierre 2003 P. Strobel, A. Ibarra-Palos, M. Anne, C. Poinsignon, A. Crisci, *"Cation ordering in $Li_2Mn_3MO_8$ spinels: structural and vibration spectroscopy studies"*, Solid State Sciences **5** (2003) 1009–1018

Piotto 2004 A. P. Piotto, *"New electroactive materials for lithium-ion rechargeable batteries"*, Dissertation, ETH, Zurich (2004)

Pletcher 1991 D. Pletcher, *"A first course in electrode processes"*, The Electrochemistry Consultancy, Alresford, Hants, (1991)

Reddy 1995 T.B. Reddy and S. Hossain, *"Handbook of batteries"*, (ed., D. Linden), McGraw-Hill, 36.1, New York (1995)

Robertson 1996 A. D. Robertson, W. F. Howard, S. H. Lu and W. F. Averill, *Ext. Abstr.,* 190th Meeting of the Electrochemical Society, San Antonio (1996) 1010

Roisnel 2001 T. Roisnel, J. Rodriguez-Carvajal, *"WinPLOTR: a windows tool for powder diffraction pattern analysis"*, Mater. Sci. Forum **378** (2001) 118

Rogers 2003 R. D. Rogers and K. R. Seddon, *"Ionic liquids - solvents of the future?"*, Science **302** (2003) 792

Rosciano 2008 F. Rosciano, *"in situ synchrotron and neutron diffraction based methods for the characterization of cathodic materials for lithium-ion batteries"*, Dissertation, ETH, Zurich (2008)

Sato 2004 T. Sato, G. Masuda and K. Takagi, *"Electrochemical properties of novel ionic liquids for electric double layer capacitor applications"*, Electrochim. Acta **49** (2004) 3603

Sears 1984 V. F. Sears, AECL Report **8490** (1984)

Shaju 2008 K. M. Shaju, P. G. Bruce, *"Nano-$LiNi_{0.5}Mn_{1.5}O_4$ spinel: a high power electrode for Li-ion batteries"*, Dalton Trans. (2008) 5471-5475

Sigala 1995 C. Sigala, D. Guyomard, A. Verbaere, Y. Piffard and M. Toumoux, *"Positive electrode materials with high operating voltage for lithium batteries: $LiCr_yMn_{2-y}O_4$ ($0 \leq y \leq 1$)"*, Solid State Ionics **81** (1995) 167

Son 2004a J. T. Son, K. S. Park, H. G. Kim, *"Surface-modification of $LiMn_2O_4$ with a silver-metal coating"*, J. Power Sources **126** (2004) 182

Son 2004b J. T. Son, H. G. Kim, Y. J. Park, *"New preparation method and electrochemical property of $LiMn_2O_4$ electrode"*, Electrochim. Acta **50** (2004) 453

Song 1998 M. Y. Song, D. S. Ahn, S. G. Kang, S. H. Chang, *"Influence of the substitution of Fe for Mn on the electrochemical properties of $LiMn_2O_4$"*, Solid State Ionics **111** (1998) 237-242

Spahr 2006 M. E. Spahr, H. Buqa, A. Würsig, D. Goers, L. Hardwick, P. Novak, F. Krumeich, J. Dentzer and C. Vix-Guterl, *"Surface reactivity of graphite materials and their surface passivation during the first electrochemical lithium insertion"*, J. Power Sources **153** (2006) 300

Strobel 1996 P. Strobel, F. Le Cras, M. Anne, *"Composition-valence diagrams: A new representation of topotactic reactions in ternary transition metal oxide systems. Application to lithium intercalation"*, J. Solid State Chem.**124** (1996) 83

Strobel 2003 P. Strobel, A. Ibarra-Palos, M. Anne, C. Poinsignon, *"Cation ordering in $Li_2Mn_3MO_8$ spinels: structural and vibration spectroscopy studies"*, Solid State Sci. **5** (2003) 1009–1018

Suarez 1997 P. A. Z. Suarez, V. M. Selbach, J. E. L. Dullius, S. Einloft, C. M. S. Piatnicki, D. S. Azambuja, R. F. deSouza and J. Dupont, *"Enlarged electrochemical window in dialkylimidazolium cation based room-temperature air and water-stable molten salts"*, Electrochim. Acta **42** (1997) 2533

Sudant 2005 G. Sudant, E. Baudrin, D. Larcher and J. M. Tarascon, *"Electrochemical lithium reactivity with nanotextured anatase-type $Ti0_2$"*, J. Mater. Chem. **15** (2005) 1263

Sun 1998 J. Sun, M. Forsyth and D. R. MacFarlane, *"Room-temperature molten salts based on the quaternary ammonium ion"*, J. Phys. Chem. **102** (1998) 8858

Sun 2002a Y. K. Sun, Y. -S. Lee, M. Yoshio and K. Amine, *"Synthesis and Electrochemical Properties of ZnO-Coated $LiNi_{0.5}Mn_{1.5}O_4$ Spinel as 5 V Cathode Material for Lithium Secondary Batteries"*, Electrochem. Solid State Lett. **5** (2002) 99

Sun 2002b Y. K. Sun, K. -J. Hong, J. Prakash and K. Amine, *"Electrochemical performance of nano-sized ZnO-coated $LiNi_{0.5}Mn_{1.5}O_4$ spinel as 5 V materials at elevated temperatures"*, Electrochem. Commun. **4** (2002) 344

Sun 2003 Y. K. Sun, C. S. Yoon, I. H. Oh, *"Surface structural change of ZnO-coated $LiNi_{0.5}Mn_{1.5}O_4$ spinel as 5 V cathode materials at elevated temperatures"*, Electrochim. Acta **48** (2003) 503

Tarascon 1993 J. M. Tarascon, D. Guyomard, and G. L. Baker, *"An update of the Li metal-free rechargeable battery based on $Li_{1+\chi}Mn_2O_4$ cathodes and carbon anodes"*, J. Power Sources **44** (1993) 689-700

Tarascon 2001 J. M. Tarascon and M. Armand, *"Issues and challenges facing rechargeable lithium Batteries"*, Nature **414** (2001) 359

Thackeray M. M. Thackeray and R. J. Gummow, *"Electrochemical cell"*, U. S. Patent 5316877

Thackeray 1983 M. M. Thackeray, W. David, P. Bruce and J. Goodenough, *"Lithium insertion into manganese spinels"*, Mater. Res. Bull. **18** (1983) 461-472

Thackeray 1997 M. M. Thackeray, *"Manganese oxides for Lithium batteries"*, Prog. Solid State Chem. **25** (1997) l-71

Thackeray 2007 M. M. Thackeray, S-H Kang, C. S. Johnson, J. T. Vaughey, R. Benedek and S A. Hackney, *"Li_2MnO_3-stabilized $LiMO_2$ (M = Mn, Ni, Co) electrodes for lithium-ion Batteries"*, J. Mater. Chem. **17** (2007) 3112-3125

Takahashi 2004 K. Takahashi, M. Saitoh, M. Sano, M. Fujita and K. Kifune, *"Electrochemical and structural properties of a 4.7 V-class $LiNi_{0.5}Mn_{1.5}O_4$ positive electrode material prepared with a self-reaction method"*, J. Electrochem. Soc. **151** (2004) A173-A177

Tsunoda 2000 M. Tsunoda, Y. Oshima, M. Yoshinaga and T. Shirasu, *"Issue on lithium-ion rechargeable batteries - prismatic lithium-ion rechargeable battery with manganese spinel and nickel-cobalt oxide cathode"*, NEC R&D **41** (2000) 13

Wakihara 1998 M. Wakihara and O. Yamamoto, *"Lithium ion batteries: fundamentals and performance"*, Wiley-VCH 1998

Wang 2003 Z. Wang, H. Ikuta, Y. Uchimoto, and Masataka Wakihara, *"Preparation and electrochemical properties of stoichiometric and non-stoichiometric $LiCo_xMn_{2-x}O_4$"*, J. Electrochem. Soc. **150** (2003) 1250-1254

Wang 2007 Q. Wang, J. Sun and C. Chen, *"Thermal stability of delithiated $LiMn_2O_4$ with electrolyte for lithium-ion batteries"*, J. Electrochem. Soc. **154** (2007) 263-267

Wang 2009 L. Wang, J. Li, X. He, W. Pu, C. Wan and C. Jiang, *"Recent advances in layered $LiNi_xCo_yMn_{1-x-y}O_2$ cathode materials for lithium ion batteries"*, J Solid State Electrochem. **13** (2009) 1157–1164

Wasserscheid 2003 P. Wasserscheid and T. Welton, *"Ionic Liquids in Synthesis"*, Wiley-VCH, Weinheim, (2003)

Webber 2002 A. Webber and G. E. Blomgren, *"Advances in lithium-ion batteries"*, (S. B. van Schalkwijk ed.), Kluwer Academic/Plenum Publishers, New York (2002) 185

Welton 1999 T. Welton, *"Room-temperature ionic liquids. solvents for synthesis and catalysis"*, Chem. Rev. **99** (1999) 2071

Whittingham 2004 M. S. Whittingham, *"Lithium batteries and cathode materials"*, Chem. Rev. **104** (2004) 4271

Wilson 1995 A. M. Wilson and J. R. Dahn, *"Lithium insertion in carbons containing nanodispersed silicon"*, J. Electrochem. Soc. **142** (1995) 326

Winter 1998 M. Winter, J. O. Besenhard, M. E. Spahr, and P. Novák, *"Insertion electrode materials for rechargeable lithium batteries"*, Adv. Mater. **10** (1998) 725-763

Winter 2004 M. Winter and Ralph J. Brodd, *"What are batteries, fuel cells, and supercapacitors?"*, Chem. Rev. **104** 10 (2004) 4245–4270

Wohlfahrt-Mehrens 1997 M. Wohlfahrt-Mehrens, A. Butz, R. Oesten, G. Arnold, R. P. Hemmer, R. A. Huggins, *"The influence of doping on the operation of lithium manganese oxide spinel"*, J. Power Sources **68** (1997) 582-585

Xiang 2009 H. F. Xiang, H. Wang, C. H. Chen, X. W. Ge, S. Guo, J. H. Sun, W. Q. Hu, *"Thermal stability of $LiPF_6$-based electrolyte and*

effect of contact with various delithiated cathodes of Li-ion batteries", J. Power Sources **191** (2009) 575–581

Xu 2004 K. Xu, *"Nonaqueous liquid electrolytes for lithium-based rechargeable batteries"*, Chem. Rev. **104** (2004) 4303

Yoon 2007 Y.K. Yoon, C.W. Park, H.Y. Ahn, D.H. Kim, Y.S. Lee and J. Kim, *"Synthesis and characterization of spinel type high-power cathode materials $LiM_xMn_{2-x}O_4$ (M = Ni, Co, Cr)"*, J. Phys. Chem. Solids **68** (2007) 780–784

Zhao 2009 S. L. Zhao, H. Y. Chen, J. B. Wen and D. X. Li, *"Electrochemical properties of spinel $LiCo_xMn_{2-x}O_{4-\delta}$ prepared by sol–gel process"*, J. Alloys Compd. **474** (2009) 473–476

Zheng 2002 Z. Zheng, Z. Tang, Z. Zhang, W. Sheng and Y. Lin, *"Surface modification of $Li_{1.03}Mn_{1.97}O_4$ spinels for improved capacity retention"*, Solid State Ionics **148** (2002) 317

Zhong 1997 Q. Zhong, A. Bonakdarpour, M. Zhang, Y. Gao and J.R. Dahn, *"Synthesis and Electrochemistry of $LiNi_xMn_{2-x}O_4$"*, J. Electrochem. Soc. **144** (1997) 205-213

Publications

Synthesis, characterization, and comparison of electrochemical properties of $LiM_{0.5}Mn_{1.5}O_4$ (M = Fe, Co, Ni) at different temperatures
A. Bhaskar, N. N. Bramnik, A. Senyshyn, H. Fuess and H. Ehrenberg
J. Electrochem. Soc.**, 157** 6 (2010) A689-A695

High-voltage cathodes for Li-ion batteries: Metallophosphoolivines and manganese-based spinels
N. N. Bramnik, K. Nikolowski, A. Bhaskar, C. Baehtz, D. Trots, A. Senyshin, H. Fuess and H. Ehrenberg
Acta Crystallogr., A64 (2008) C59

Conference Contributions

Synthesis and characterization of $LiNi_{0.5}Mn_{1.5}O_4$ cathode materials: impact on electrochemical properties and morphology
A. Bhaskar, N. N. Bramnik, H. Ehrenberg and H. Fuess
ICAM 2007 at Mahatma Gandhi University, India

About the cyclability of high-voltage spinels $LiM_{0.5}Mn_{1.5}O_4$ (M = Fe, Co, Ni)
A. Bhaskar, N. N. Bramnik, H. Ehrenberg, A. Senyshyn and H. Fuess
LiBD-4 2009 – Electrode materials at Arcachon, France

$LiNi_{0.5}Mn_{1.5}O_4$: The effect of different coatings on the electrochemical performance
A. Bhaskar, N. N. Bramnik, H. Ehrenberg, R. Schierholz, F. Scheiba and H. Fuess
IMLB 2008, 14th international meeting on lithium batteries at Tianjin, China

Acknowledgement

This work is carried out at the institute for materials science, Technische Universität Darmstadt. The financial support by the “Deutsche Forschungsgemeinschaft” (DFG, EH183/8) is gratefully acknowledged.

I would like to thank my supervisor and referee Prof. Dr. rer. nat. Helmut Ehrenberg and my co-supervisor Prof. Dr. Ing. Hartmut Fuess for their valuable guidance and thoughtful comments. I would also like to express my sincere gratitude to my second co-supervisor Dr. Natalia N. Bramnik for her enthusiastic guidance. She taught me several new things and was always ready to answer my countless questions. Several ideas in this thesis were emerged through our energetic discussions.

I am grateful to Prof. Dr. rer. nat. Wolfram Jaegermann for being my referee and also to Prof. Dr. rer. nat. Wolfgang Ensinger and Prof. Dr. rer. nat. Jörg J. Schneider for being my internal and external examinors.

I would like to thank Dr. Anatoliy Senyshyn for the neutron diffraction measurements and Dr. Dymitro Trots for providing support with the *in situ* synchrotron measurements. I wish to thank Dr. Wolfgang Gruner, Dr. Steffen Oswald, Dr. Daria Mikhailova and Mrs. Andrea Voss at IFW Dresden who measured the TG-DTA, XPS, high temperature XRD and ICP-OES measurements which appear in this thesis. I wish to thank Dr. Gennady Cherkashinin, who measured the XPS data which are provided in chapter 10.

I wish to thank Dr. Ljubomira Ana Schmitt, Mr. Ditty Dixon and Dr. Roland Schierholz for providing me with the TEM images.

Dipl-Ing Claudia Fasel and Mrs. Renate Benz are gratefully acknowledged for initial measurements of TG-DTA (presented in chapter 7) and ICP-OES, which led me to some of the detailed studies reported in this thesis.

Technical assistance from Mr. Heinz Mohren and Mr. Jean-Christoph Jaud are gratefully acknowledged.

I would like to acknowledge the works done by my student helpers Krystina Bachtin, Thomas Leiter and Heiko Hoffmann, during the last year of this thesis.

Mr. Rene Schmitz, Mr. Raphael Schmitz, Dr. Alexandra Lex-Balducci and Prof. Martin Winter from WWU Münster and Ms. Hai-Yen Tran, Ms. Michaela Memm and Dr. Wohlfahrt-Mehrens from ZSW Ulm are gratefully acknowledged for providing me with the opportunity and materials to work in these institutes and helping me with the lab works.

All colleagues in working groups “structural research” and “renewable energy” from TU Darmstadt and “functional composite materials” from IFW Dresden are gratefully acknowledged for their support and help during this work.

I wish to thank my primary and high-school teachers to create an enthusiasm about science in me and lecturers for BSc and MSc. Chemistry courses for providing me with a deeper understanding.

I would like to thank my friends Ditty, Thomy, Lena, JB, Gisa, Joshni, Praseedha, Laetitia, Joachim, Ljuba, Alex, Matze, Sajan, Ani, Lincy, Angelina, Ilona, Magda, Niels, So-Yun, Kumar, Gopi, who have made my time in Germany as well as in India unforgettable. Special thanks to Karen, Gerhard and their family.

I wish to thank Thomy’s family: Uli, Frank, their parents and Jeanette to give me their love and affection which made me feel them as my second family.

Finally I wish to thank my parents, grant parents and my sister, Anju, whom I missed a lot during these years, for their love, support and understanding.

Thanks to God almighty!

Curriculum vitae

Personal

Aiswarya Bhaskar
Kalathara House, East Gate, Vaikom,
Kottayam, Kerala, India, 686141
Born. on 23. 05. 1984 in Cherthala

Education

1989-1993	Govt. Lower Primary School, Ottappunna, Cherthala Kerala, India
1993-1994	Sree Narayana Upper Primary School, Sreekandeswaram, Cherthala, Kerala, India
1994-2001	Jawahar Navodaya Vidyalaya, Alapuzha, Kerala, India
2001-2004	Bachelor of Chemistry (BSc. Chem), Mahatma Gandhi University, Kottayam, India
2004-2006	Master of Chemistry (MSc. Chem), Mahatma Gandhi University , Kottayam, India with one semester Master's thesis from IIT Madras

Work experience

09/2006-02/2007	Lecturer for MSc. Chem at Devamatha College, Kuravilangadu, Kerala, India
03/2007-08/2007	Research Assistant at NIIST (formerly RRL), Trivandrum, India
09/2007-09/2010	Ph.D thesis under the supervision of Prof. Dr. rer. nat. H. Ehrenberg, Prof. Dr. Ing. H. Fuess and Dr. N. N. Bramnik at institute for complex materials-IFW Dresden and institute for materials science-TU Darmstadt

Declaration

I hereby declare that I have made this thesis independently and with the stated and permitted aids.

I have not given any doctoral exam so far.

Darmstadt, 01/19/2011

MSc. Chem. Aiswarya Bhaskar

Investigations on $LiM_{0.5}Mn_{1.5}O_4$ (M = Fe, Co, Ni) Spinels as High-Volt cathode materials for Rechargeable Li-Ion batteries

Aiswarya Bhaskar

Institute for Materials Science

Technische Universität Darmstadt

2011

D 17